

APPLICATION OF FERMI-EYGES SCATTERING THEORY
TO MAGNETICALLY SCANNED THERAPEUTIC ELECTRON BEAMS

A Thesis Report

by

George A. Sandison

Submitted to the Faculty of
Graduate Studies of the
University of Manitoba in
partial fulfillment of the
requirements for the degree
of Doctor of Philosophy

May 1987 ©
Winnipeg, Manitoba

Permission has been granted to the National Library of Canada to microfilm this thesis and to lend or sell copies of the film.

The author (copyright owner) has reserved other publication rights, and neither the thesis nor extensive extracts from it may be printed or otherwise reproduced without his/her written permission.

L'autorisation a été accordée à la Bibliothèque nationale du Canada de microfilmer cette thèse et de prêter ou de vendre des exemplaires du film.

L'auteur (titulaire du droit d'auteur) se réserve les autres droits de publication; ni la thèse ni de longs extraits de celle-ci ne doivent être imprimés ou autrement reproduits sans son autorisation écrite.

ISBN 0-315-37346-6

APPLICATION OF FERMI-EYGES SCATTERING THEORY
TO MAGNETICALLY SCANNED THERAPEUTIC ELECTRON BEAMS

BY

GEORGE A. SANDISON

A thesis submitted to the Faculty of Graduate Studies of
the University of Manitoba in partial fulfillment of the requirements
of the degree of

DOCTOR OF PHILOSOPHY

© 1987

Permission has been granted to the LIBRARY OF THE UNIVERSITY OF MANITOBA to lend or sell copies of this thesis, to the NATIONAL LIBRARY OF CANADA to microfilm this thesis and to lend or sell copies of the film, and UNIVERSITY MICROFILMS to publish an abstract of this thesis.

The author reserves other publication rights, and neither the thesis nor extensive extracts from it may be printed or otherwise reproduced without the author's written permission.

"The essential point in science is not a complicated mathematical formalism or a ritualized experimentation. Rather the heart of science is a kind of shrewd honesty that springs from really wanting to know what the hell is going on!"

Saul-Paul Sirag

Acknowledgements

I would like to take this opportunity to sincerely thank my supervisor, Dr. Walter Huda, for his guidance and helpful advice during my Ph.D. studies. I would also like to express my appreciation to the Department of Medical Physics of the Manitoba Cancer Treatment and Research Foundation (MCTRF) for accepting me as their first Ph.D. student, on the then embryonic Medical Physics Graduate Program, in 1982. My thanks are also due to Dr. Peter Dunscombe for offering me a Physicist position at the MCTRF upon submission of this thesis to the Faculty of Graduate Studies. I could not have hoped to work with a more friendly and able group of people.

It has been an uphill battle, comprised of long working hours, to complete the research work carried out for this thesis, and the work both published and unpublished which never made it into the pages of this manuscript. The understanding and encouragement of my wife, Linda Temple, to whom many of these hours should have been devoted, was an indispensable and constant source of motivation.

Also, my personal deadline of May 1987 could not have been met without the speedy and conscientious typing skills of Thelma Davidson. Thank you Thelma!

Finally, I would like to recognize the funding for components of this research work provided by a grant from the Manitoba Health Research Council. Personal financial support has also been provided by the following agencies during this period of study.

1. Manitoba Health Research Council Studentship (July 1986 - June 1987)
2. National Cancer Institute of Canada "Steve Fonyo" Studentship (July 1985 - June 1986)
3. National Cancer Institute of Canada Studentship (July 1984 - June 1985)
4. Manitoba Cancer Treatment and Research Foundation (September 1982 - June 1984)

Abstract

Fermi-Eyges small angle multiple scattering theory has been applied to therapeutic broad electron beams in the energy range 7 - 32 MeV. These beams are produced in the Sagittaire Therac 40 linear accelerator, by magnetic scanning of the narrow accelerator beam. Broad electron beams are modelled by a collimated isotropic source of electrons, the thick lead collimation is assumed equivalent to an infinitely thin absorbing plate with the source located at the exit window of the accelerator.

The predictive power of this simple model is excellent in the air space above patients. Beam profile shape is accurately predicted for any clinically used beam energy, source surface distance or field size for penumbra formed by a single collimator and no measured input data is required. When penumbra are formed by a double collimator system, the collimator closest to the source restricts the field size causing a variation in fluence and mean square angle of travel of the electrons at the level of the lower collimator. These variations are accounted for by introducing an empirical factor into the formalism. An interesting feature of this empirical factor is that it is field size dependent and its effect on penumbra width may be scaled for both beam energy and SSD to accurately predict beam profile shape.

The collimated isotropic source model may be used to predict within 5% the changes in beam output for a fixed field size with SSD or beam energy and also the increase in FWHM of beam profiles above the

FWHM expected on geometrical grounds at small field sizes and low beam energies. These changes in beam output and beam profile FWHM may be satisfactorily explained by lateral electron disequilibrium effects and the accuracy of the predictions demonstrates that the use of the virtual source concept for magnetically scanned electron beams is redundant.

In tissue-equivalent material, three experimental methods of deriving electron pencil beam spread have been investigated and compared to the theoretical predictions of Fermi-Eyges theory. Results indicate that the use of central axis dose ratios to generate values of $\sigma(z)$ is very limited and that the empirical pinhole technique is beset with experimental difficulties. The use of broad beam penumbra to generate values of pencil beam spread does not suffer from major shortcomings and gives results in agreement with Fermi-Eyges theory up to about 0.7 times the incident electron range in media equivalent to bone, lung and muscle.

Range straggling modifications to Fermi-Eyges theory suggested by Werner et al (1982) and Lax et al (1983) have been shown to have limited predictive power. Neither modification is universally satisfactory for the range of tissue densities and atomic numbers encountered in patients. Alternative theoretical modifications to Fermi-Eyges theory to account for range straggling in homogeneous and inhomogeneous media require development.

TABLE OF CONTENTS

	PAGE
Acknowledgements	1-2
Abstract	3-4
Glossary of Terms	13-18
CHAPTER 1 GENERAL INTRODUCTION	19
1.1 Introduction	20-23
1.2 Outline of Thesis	23-24
CHAPTER 2 BASIC PHYSICS AND CHARACTERISTICS OF THERAPEUTIC ELECTRON BEAMS	25
2.1 Introduction	26
2.2 Basic Physics	26
2.2.1 Energy Loss	26-27
2.2.2 Stopping Power	27-30
2.2.3 Continuous Slowing Down Approximation	30-31
2.2.4 Scattering	31
2.2.5 Single Scattering	31-32
2.2.6 Multiple Scattering	32-35
2.2.7 Mass Angular Scattering Power	35-36
2.3 Characteristics of Therapeutic Beams	36
2.3.1 Dose	36-38
2.3.2 Depth Dose Curves	38-40
2.3.3 Practical Range, R_p	40
2.3.4 Field Size and Isodose Curves	40-41
2.3.5 Inhomogeneities	41-44
CHAPTER 3 REVIEW OF DOSE COMPUTATION ALGORITHMS	45
3.1 Introduction	46-47
3.2 Broad Beam Approaches to Electron Dosimetry	47
3.2.1 Empirical Methods	47-50
3.2.2 Boltzmann Transport Equation	50
3.2.3 Age Diffusion Equation	50-53
3.2.4 Inhomogeneities	54-56
3.3 Pencil Beam Approaches to Electron Dosimetry	57
3.3.1 Empirical Methods	57-59
3.3.2 Analytical Methods	59-63
3.3.3 Inhomogeneities	63-68
3.4 Discussion	68-79
3.5 Conclusions	79-81

	PAGE
CHAPTER 4 FERMI-EYGES THEORY AND APPLICATIONS TO RADIOTHERAPY	82
4.1 Introduction	83
4.2 The Fermi Equation and Solutions	83-93
4.3 Applications in Radiotherapy	93
4.3.1 Parallel Rectangular Broad Beams	93-97
4.3.2 Diverging Rectangular Broad Beams	97-103
4.4 Conclusions	103-104
Appendix 4.1	105-107
Appendix 4.2	108-116
CHAPTER 5 APPLICATION OF FERMI-EYGES SCATTERING THEORY TO MAGNETICALLY SCANNED THERAPEUTIC ELECTRON BEAMS IN AIR	117
5.1 Introduction	118-120
5.2 Fermi-Eyges Theory	120-123
5.3 Relationship Between Broad Beams and Pencil Beams	123-127
5.4 Lateral Scatter Disequilibrium	127-130
5.5 Accelerator Model for Broad Beam Penumbra Formation	131-134
5.6 Materials and Methods	134-136
5.7 Results	136
5.7.1 Static Beam Profile Measurements	136-139
5.7.2 Verification of the Isotropic Point Source Location	139-141
5.7.3 Penumbra Width Below Thick Lead Collimation	141-142
5.7.4 Predictive Power and Limitation of Model for a Single Collimator	142
5.7.4.1 Lateral Position	142-145
5.7.4.2 Beam Energy	145-148
5.7.4.3 Source Surface Distance	148
5.7.4.4 Field Size	148-152
5.7.5 Predictive Power and Limitations of Model for a Double Collimator	152
5.7.5.1 Beam Energy	152-154
5.7.5.2 Source Surface Distance	154-155
5.7.5.3 Field Size	155-157
5.7.6 Predictive Power and Limitations of Model for Beam Output and Profile FWHM	157
5.7.6.1 Output for Fixed Field Size	157-160
5.7.6.2 Output for Variable Field Size	160-164
5.7.6.3 Beam Profile FWHM	164-168
5.8 Discussion	168-177
5.9 Conclusion	177-179
Appendix 5.1	180-182

	PAGE
CHAPTER 6 APPLICATION OF FERMI-EYGES SCATTERING THEORY TO MAGNETICALLY SCANNED THERAPEUTIC ELECTRON BEAMS IN TISSUE	183
6.1 Introduction	184-186
6.2 Methods of deriving pencil beam spread in tissue	186
6.2.1 Theoretical	186-189
6.2.2 Semi-Empirical from Central Axis Dose Ratios	190-191
6.2.3 Semi-Empirical from Penumbra	191-192
6.2.4 Empirical	192-193
6.3 Materials and Methods	193-197
6.4 Results	198
6.4.1 Theoretical Method	198-200
6.4.2 Semi-empirical Central Axis Dose Ratio Method	200-204
6.4.3 Semi-empirical Penumbra Method	204-210
6.4.4 Empirical Method	210-215
6.5 Discussion	215-226
6.6 Conclusions	226-228
CHAPTER 7 CONCLUSIONS	229
7.1 Conclusions	230-234

LIST OF FIGURES

	PAGE
Figure 2.1 Central axis depth dose curves in water for therapeutic beams of energy in the range 0 - 50 MeV	39
Figure 2.2 Typical isodose curves in water for a 22 MeV electron beam	42
Figure 4.1 Trigonometrical relationships between the polar angle θ and its projections θ_x and θ_y on to the (z,x) and (z,y) planes for an electron originally travelling parallel to the z-axis	84
Figure 4.2 Geometry for a pencil beam scanned over a wide angle θ_0 between the limits $-\theta_{0max} < \theta_0 < +\theta_{0max}$	98
Figure 5.1 Spatial fluence, most probable angle of travel and mean square angle of travel of electrons from three point sources incident upon a semi-infinite air medium	122
Figure 5.2 Spatial variance of a Gaussian pencil beam at depth z when defined at a collimator positioned at distance z' beyond an isotropic point source	126
Figure 5.3 Definition of penumbra width for the central plane of a broad beam profile	128
Figure 5.4 Comparison of predicted beam profiles (full lines) for a 20 x 20 cm field to the measured data for 7, 16, 22 and 32 MeV energies. Only half the profile is shown	129
Figure 5.5 Schematic of the treatment head of the Sagittaire Therac 40 accelerator	132
Figure 5.6 Accelerator model used to compute broad beam dose distributions	133
Figure 5.7 Static accelerator beam profiles in the x and y directions at 100 cm SSD for a 22 MeV beam	137

	PAGE
Figure 5.8 Fit of the variance for the Gaussian accelerator static electron beam profile in air with SSD to obtain the variance of the Gaussian initial angular distribution of an equivalent pencil beam.	138
Figure 5.9 Determination of the isotropic source position	140
Figure 5.10 Variation of $\sigma(z)$ derived from penumbra measured below a large straight edged block on the central axis of a 20 x 20 cm ² field with block thickness.	143
Figure 5.11 Variation of $\sigma(z)$ derived from penumbra measured below a 5.1 cm thick block on the central axis of a 20 x 20 cm ² field with block angle for a 7 MeV beam	144
Figure 5.12 Variation of $\sigma(z)$ derived from penumbra measured below a thick block with distance of the block off the central axis for a 20 x 20 cm ² field at 100 cm SSD and 7, 10, 16 and 22 MeV beam energies	146
Figure 5.13 Variation of $\sigma(z)$ derived from penumbra measured below a thick block with distance of the block off the central axis for 15 x 15 cm ² , 10 x 10 cm ² and 5 x 5 cm ² fields at 100 cm SSD and 7 and 22 MeV beam energies	147
Figure 5.14 Variation of $\sigma(z)$ derived from penumbra measured below trimmer collimation at 100 cm SSD with beam energy	149
Figure 5.15 Variation of $\sigma(z)$ derived from penumbra measured below trimmer collimation with SSD for a 22 MeV beam energy	150
Figure 5.16 Variation of $\sigma(z)$ derived from penumbra measured below photon collimation at 100 cm SSD with field size for 7, 16, 22 and 32 MeV beam energies	158
Figure 5.17 Variation of Ionization with source chamber distance (SCD) for a 6 cm x 6 cm field at beam energies of 7, 16, 22 and 32 MeV	161

	PAGE
Figure 5.18 Variation of Ionization with SCD for a 7 MeV beam energy at square field sizes of 5 x 5 cm, 10 x 10 cm and 15 x 15 cm	162
Figure 5.19 Variation of Ionization with SCD for a 10 MeV beam energy at square field sizes of 5 x 5 cm, 10 x 10 cm and 15 x 15 cm	163
Figure 5.20 Variation in output at 100 cm source chamber distance with field size for beam energies of 7, 10, 22 and 32 MeV. Field is defined by the photon collimators	165
Figure 5.21 Variation in output at 100 cm SCD with field size for beam energies of 7 MeV and 32 MeV. Theoretically predicted curves shown dashed.	166
Figure 6.1 Comparison of film and ionization chamber measurements for the central axis percentage depth dose of a 20 cm x 20 cm field using a 22 MeV beam energy and 100 cm SSD	195
Figure 6.2 Theoretical variation of $\sigma(z)$ with depth z in homogeneous scattering media of different atomic number for a point monodirectional pencil beam	199
Figure 6.3 Theoretical variation of $\sigma(z)$ with depth z in water and incident beam energy for a point monodirectional pencil beam	201
Figure 6.4 Depth ionization curves in temex of a 22 MeV beam energy for both a 20 x 20 cm and a 2.2 cm x 2.2 cm field	202
Figure 6.5 Semi-empirical $\sigma(z)$ values generated from central axis data presented in Figure 6.4	203
Figure 6.6 Variation of semi-empirical $\sigma(z)$ values in temex with small field central axis depth dose for a 22 MeV beam energy	205
Figure 6.7 Variation of semi-empirical $\sigma(z)$ values in polystyrene derived from the penumbra of a 10 cm x 10 cm field for 7 and 22 MeV incident beam energies	207

	PAGE
Figure 6.8 Variation of semi-empirical $\bar{\sigma}(z)$ values in lung-equivalent material derived from the penumbra of a 10 cm x 10 cm field for 7 and 22 MeV beam energies	208
Figures 6.9 Variation of semi-empirical $\bar{\sigma}(z)$ values in bone equivalent material derived from the penumbra of a 10 cm x 10 cm field for 7 and 22 MeV beam energies	209
Figure 6.10 Comparison of measured semi-empirical $\bar{\sigma}(z)$ values in polystyrene for a 22 MeV beam energy with predictions of Fermi-Eyges theory and empirical modifications to this theory	211
Figure 6.11 Comparison of measured semi-empirical $\bar{\sigma}(z)$ values in lung-equivalent material for a 16 MeV beam energy with empirical modifications to Fermi-Eyges theory	212
Figure 6.12 Comparison of measured semi-empirical $\bar{\sigma}(z)$ values in bone-equivalent material for a 16 MeV beam energy with empirical modifications to Fermi-Eyges theory	213
Figure 6.13 Profiles of an empirical pencil beam of 22 MeV energy at 1 cm and 8 cm depth in temex	214
Figure 6.14 Central axis percentage depth dose measured along the pencil beam using film	216
Figure 6.15 Variation of empirical $\bar{\sigma}(z)$ values with depth z in temex for a 22 MeV pencil beam	217

LIST OF TABLES

	PAGE
Table 2.1 Physical properties of media encountered in patients	44
Table 4.1 Solutions to the Fermi Equation in the z-x plane	90
Table 5.1 Variation of linear scattering power k in air with electron beam energies of the Sagittaire Therac 40 accelerator	124
Table 5.2 Variation of $\sigma(z)$ derived from penumbra measured below trimmer collimation at 100 cm SSD with field size for a 22 MeV beam	151
Table 5.3 Variation of $\sigma(z)$ derived from penumbra measured below double collimator system at 100 cm SSD with beam energy for a 20 x 20 cm ² field defined at 100 cm SSD	153
Table 5.4 Variation of $\sigma(z)$ derived from penumbra measured below photon collimation with SSD for a 20 x 20 cm ² field defined at 100 cm SSD	156
Table 5.5 Variation of empirical perturbation factors f with field size setting of the double collimator system	159
Table 5.6 Comparison of measured values of FWHM with predicted values for y-direction beam profiles	167
Table 6.1 Physical properties of dosimetric materials	197

Glossary of Terms

The symbols and terms defined in this glossary are presented in the order found in the text of this thesis.

S_{col} = collision stopping power: MeVcm^{-1}

ρ = density: gcm^{-3}

$\frac{S_{col}}{\rho}$ = mass collision stopping power: $\text{MeVg}^{-1}\text{cm}^2$

r_e = the classical electron radius: $2.817938 \times 10^{-13}\text{cm}$

m_{oc}^2 = electron rest mass energy: 0.511 MeV

β = ratio of electron velocity to that of light

Z = atomic number

U = atomic mass unit

A = relative atomic mass

I = mean excitation energy of a medium: MeV

T = kinetic energy of an electron: MeV

J = T/m_{oc}^2

δ = density effect correction

Δ = lower limit of energy transferred to delta-rays: MeV

η = fractional energy cut-off Δ/T

$\frac{S_{rad}}{\rho}$ = mass radiative stopping power: $\text{MeVg}^{-1}\text{cm}^2$

$\frac{S_{tot}}{\rho}$ = total mass stopping power: $\text{MeVg}^{-1}\text{cm}^2$

$(\sigma_{rad,n})$ = dimensionless scaled radiative cross-section for energy loss via electron-nuclear interactions

- $(\phi_{\text{rad},e})$ = dimensionless scaled radiative cross-section for energy loss via electron-electron interactions
- λ = fine structure constant: 1/137.04
- $\frac{d \Sigma_n}{d \mathcal{E}}$ = differential cross-section for the emission of a photon of energy \mathcal{E} due to the interaction of the electron with the screened coulomb field of the atomic nucleus
- $\frac{d \Sigma_e}{d \mathcal{E}}$ = differential cross-section for the emission of a photon of energy \mathcal{E} due to the coulombic interaction of the incident electron with one of the atomic electrons
- r_0 = continuous slowing down approximation range
- θ = polar scattering angle: radians
- γ = cut-off deflection angle for restricted mass scattering power
- $D(\vec{r})$ = absorbed dose at point \vec{r}
- s = pathlength travelled by an electron along the direction of its motion
- $\Omega(\vec{r})$ = unit vector in the direction of the electron motion
- $\Phi_{E,\Omega}$ = electron fluence differential in energy and angle
- $\Phi(z)$ = primary electron fluence integrated over all energies and angles at depth z
- R_p = practical electron range
- ρ_e = electron density: electrons cm^{-3}
- $L(\beta)$ = stopping number per electron
- z = depth in medium

z_m	=	depth of maximum dose
EXP	=	exponential
ERF	=	error function
a	=	half-length of field in x-direction
$d\theta$	=	element of polar scattering angle
$\Sigma(\theta)$	=	differential cross-section for scattering per atom
e	=	charge of electron: $1.602 \times 10^{-19} \text{C}$
$\overline{\theta^2}$	=	mean square polar scattering angle
$P(\theta)d\theta$	=	probability of finding an electron from a point mono-directional source travelling with polar angle θ in a scattering medium
$\overline{\theta^2}_{1/e}$	=	angle at which scattering distribution falls to 0.368 of its value at zero angle
$\overline{\theta^2}_M$	=	mean square angle of the Gaussian term in the Moliere series
k	=	linear angular scattering power: cm^{-1}
$\frac{k}{\rho}$	=	mass angular scattering power: g^{-1}cm^2
θ_m	=	cut-off polar scattering angle due to the finite size of the nucleus
θ_μ	=	screening angle due to the screening of the nucleus by orbital electrons
x	=	lateral coordinate
∇^2	=	Laplacian operator

- K = diffusion coefficient
 θ_x = polar angle projected on to z,x plane
 θ_y = polar angle projected on to z,y plane
 $\overline{\theta_x^2}$ = mean square of polar angles projected on to z,x plane
 $\overline{\theta_y^2}$ = mean square of polar angles projected on to z,y plane
 $P_{\Delta z}(\theta_x)d\theta_x$ = probability of an electron being deflected through a projected polar angle between θ_x and $\theta_x+d\theta_x$ after traversing a thickness Δz of scattering material
 $F(x,y,z,\theta)dxdy d\theta$ = probability of finding an electron at depth z and lateral coordinate x,y travelling with a polar angle between θ and $\theta+d\theta$ to the z axis
 $F(z,x,\theta_x)dxd\theta_x$ = probability of finding an electron at depth z and lateral coordinate x , travelling with a projected polar angle between θ_x and $\theta_x+d\theta_x$ to the z axis
 $F(z,y,\theta_y)dyd\theta_y$ = probability of finding an electron at depth z and lateral coordinate y , travelling with a projected polar angle between θ_y and $\theta_y+d\theta_y$ to the z axis
 A_i = $1/2 \int_0^z k(z-\epsilon)^i d\epsilon$; $i = 0,1,2$
 A'_i = $\overline{\theta_x^2(0)} z^{1+A_i}$; $i = 0,1,2$
 B = $A'_0 A'_2 - A'_1{}^2$
 $\overline{\theta_x}$ = mean of polar angles projected on to z,x plane

- $F(z, x)$ = spatial probability distribution in z, x plane irrespective of the projected angle of travel θ_x of the electrons at depth z
- $\sigma^2(z)$ = variance of Gaussian spatial probability distribution for a pencil beam at depth z
- $F(z, \theta_x)$ = angular probability distribution projected on to the z, x plane irrespective of lateral position x at depth z
- $F(z)$ = total number of electrons at depth z
- $F(z, x, y)$ = three dimensional spatial probability distribution
- $\tilde{F}(z, x, \theta_x)$ = convolution of $F(z, x, \theta_x)$ over broad field dimension in x -direction
- $\tilde{F}_i(z, x)$ = moments of $F(z, x, \theta_x)$ with respect to θ_x : $i=0, 1, 2$
- $\langle \theta_x \rangle (z, x)$ = mean value of θ_x in broad field at position z, x in z, x plane
- $\langle \theta_x^2 \rangle (z, x)$ = mean square value of θ_x in broad field at position z, x in z, x plane
- θ_0 = angle with respect to z axis through which pencil beam scanned
- θ_{0max} = maximum angle with respect to z axis through which pencil beam scanned
- b = half-field width in y -direction
- x', y', z', θ'_x = rotated coordinate system
- $F(z, x, \theta_x, \theta_0)$ = distribution function for a pencil beam entering a medium at projected angle θ_0 in the z, x plane to the z axis

- k_0 = scattering power constant
- E = beam energy
- N_0 = Avogadro's number = 6.022045×10^{23} atoms per gram atom
- f_i = fraction by weight of element Z_i of mass number A_i
- σ_{mcs}^2 = component of the variance of a pencil beam Gaussian spatial probability distribution due to multiple coulomb scattering (mcs)
- d = distance below collimator positioned at depth z
- t = thickness of collimator
- f = empirical perturbation factor for reducing theoretical $\overline{\theta_x^2}$
- $W(z)$ = penumbra width of broad field at depth z
- θ_{xmax} = maximum projected scattering angle beyond which electrons are considered to be absorbed
- $Q(z)$ = $\text{EXP}[-R^{1.2}(1.5-R)]$
- R = $0.95(z/R_p)$
- $S(z)$ = half-length of small field at depth z
- $L(z)$ = half-length of large field at depth z
- N = square root of normalized central axis dose ratio for small and large fields
- $D(x,y,z)$ = spatial dose distribution
- $D_\infty(z)$ = central axis dose distribution for an infinitely large field
- SSD = source-surface distance
- $P(z)$ = central axis dose distribution for a pencil beam
- FWHM = full width at half maximum of a beam profile

Chapter 1

GENERAL INTRODUCTION

1.1 Introduction

Cancer is the second largest single cause of death in the adult population of Canada. One effective method of treatment for cancer is the use of external beams of ionizing radiation. This treatment is known as radiotherapy and its optimal effectiveness depends upon maximizing the radiation damage to tumour tissue and minimizing the damage to any surrounding normal tissue. To achieve this goal, accurate knowledge of the tumour or target volume and surrounding anatomy is required, in addition to an optimized spatial map of the dose distribution within the patient. Anatomical detail may be provided by several imaging modalities, most notable of which is X-ray computed tomography. The spatial distribution of dose is optimized by the appropriate selection of treatment variables which include the position of beam entry to the patient, angle of beam entry, beam energy, field size and shape, source to skin distance and bolus material. The large number of anatomical sites, treatment variables and the patient load for cancer centers, makes empirical measurement of dose distributions for individual patients undesirable. Computerized dose computation algorithms are used instead.

High energy photon and electron beams are the two radiation modalities most commonly available for the treatment of tumours. The therapeutic use of electrons in the energy range between 5 and 35 MeV is advantageous because of the rapidly descending dose

gradient with depth compared to high energy photons. This results in a significant reduction in dose to normal tissues distal to the tumour volume. Electron therapy is therefore potentially useful in treating regions of the head, neck and thorax since large doses to radiosensitive or critical organs such as the eyes, central nervous system and lung can be avoided.

The International Commission on Radiological Units and Measurements, in report 24 (ICRU 1976), suggests that the degree of accuracy required for the delivery of tumour dose in radiotherapy is $\pm 5\%$. This number is based on the steepness of dose-response curves for a limited number of tissues and is intended to reasonably minimize tumour recurrence rate and normal tissue complications. Unfortunately, the error limit poses a major problem for electron radiotherapy. There does not currently exist an algorithm which is capable of computing electron dose to within $\pm 5\%$ for all patient anatomical locations and treatment conditions. The objective of this work has been to investigate and develop pencil beam methods of electron dose computation to achieve an algorithm capable of predicting dose distribution changes with treatment variables, which has the desired degree of accuracy in cancer patients and which requires a minimal amount of experimental input data. This thesis represents a significant advance toward the realization of this objective.

The small-angle multiple scattering theory of Fermi (Rossi

and Greisen 1941), and later developments by Eyges (1948) and Brahme (1975), has been used to describe the penetration of an electron pencil beam through air and tissue. The broad electron beams from a Sagittaire Therac 40 linear accelerator are modelled by a collimated isotropic source of pencil beams. This model is considered applicable to all accelerators which utilize magnetic quadrupole scanning of a narrow accelerator beam to produce broad beams, and is the model which is most similar to the beam geometry used in radiation therapy (ICRU 1984a). Even so, very few calculations have been performed in this geometry. Berger and Seltzer (1978) used an isotropic source approach for calculations of dose from a scatter foil type accelerator. Recent work by Huizenga and Storchi (1986a, 1987) has also been performed to develop an isotropic source model for a magnetically scanned accelerator.

A large part of this thesis is the modelling of the collimated therapeutic electron beams in air. Accurate modelling of the beams in air is an important component of treatment planning and accounts for the effect of changes in the treatment variables of beam energy, field size, and source to skin distance on dose distributions in tissue and beam output. The collimated isotropic source model is shown to break down in homogeneous tissue-equivalent media at a depth of about 0.7 times the range of the electrons. This is due to the growing importance with depth of

secondary interaction effects neglected by Fermi-Eyges theory. A number of methods used in radiotherapy for obtaining values of pencil beam spread in homogeneous media are also examined and compared to the theory. Major limitations associated with several of the methods have been revealed and future work will clearly need to take these limitations into account to achieve the required accuracy in patient dosimetry.

1.2 Outline of the thesis

Chapter 2 briefly introduces the physics of electron interactions in tissue for electrons of therapeutic energy (5 MeV to 50 MeV). It includes concepts used in radiotherapy such as absorbed dose, depth dose curves, isodoses and the effect of inhomogeneities on these parameters.

Chapter 3 reviews the electron dose computation algorithms which have been developed for radiotherapy. Recent developments in pencil beam approaches to electron dose computation are emphasized and their limitations discussed.

Chapter 4 presents a detailed description of Fermi-Eyges theory and some theoretical calculations which provide the basis of the isotropic source model.

Chapter 5 reports on the in-air development and experimental verification of the collimated isotropic source model of the Sagittaire Therac 40 accelerator. The predictive power of this model for beam profile shape and beam output in air is presented

for rectangular fields.

Chapter 6 intercompares three experimental methods of obtaining electron pencil beam spread in tissue with the predictions of Fermi-Eyges theory. The limitations and advantages of each method are discussed. The predictive power of the collimated isotropic source model developed for air is tested in homogeneous phantoms of muscle, bone and lung equivalent media.

Chapter 7 consists of a summary of the conclusions derived from the work presented in this thesis.

Chapter 2

BASIC PHYSICS AND CHARACTERISTICS
OF THERAPEUTIC ELECTRON BEAMS

2.1 Introduction

In this chapter, the basic physics of the interactions of electrons in the therapeutic energy range (5 - 30 MeV) with tissue are summarized. Concepts commonly used in electron radiotherapy such as absorbed dose, range, percentage depth dose and isodose distributions are introduced. In addition, the effect of inhomogeneities on the spatial distribution of electron dose is discussed.

2.2 Basic Physics

2.2.1 Energy Loss

Inelastic electron-electron scattering is the main energy-loss mechanism for electrons of therapeutic energy. This interaction results in the excitation or ionization of atomic electrons. The ionized atomic electron may, by definition, receive up to half the incident electron's energy and is commonly called a delta-ray (ICRU 1970). A second important energy-loss mechanism for electrons of therapeutic energy is inelastic nuclear scattering. This process involves an inelastic free electron-nucleus collision accompanied by the emission of quanta of radiation known as bremsstrahlung (Koch and Motz 1959). An electron of therapeutic energy penetrating tissue undergoes a very large number of statistically random energy loss interactions. The statistical nature of this energy loss leads to a spectrum of energies for electrons which have travelled the same

pathlength. The energy-loss fluctuations about the average value is termed energy straggling (Landau 1944, Blunck and Westphal 1951) or alternatively range straggling when reference is made to the total pathlength or range travelled.

2.2.2 Stopping Power

The total stopping power S_{tot} is the average rate at which electrons lose energy at any point along their paths (ICRU 1984a). It is commonly separated into two components: (a) the collision stopping power S_{col} , which is the average energy loss per unit pathlength due to inelastic electron-electron scattering and (b) the radiative stopping power S_{rad} , which is the average energy loss per unit pathlength due to the emission of bremsstrahlung (ICRU 1980).

Electron stopping powers are rarely measured and are therefore normally obtained from stopping power theory. The collision stopping powers for electrons at energies above 10 keV are evaluated using the theory of Bethe (1933) and the interaction cross section described by Moller (1932). It is often convenient to divide stopping powers by the density ρ of the medium and add the prefix "mass" to the name. The mass collision stopping power, S_{col}/ρ is given by (ICRU 1984b)

$$\frac{S_{\text{col}}}{\rho} = \frac{2\pi r_e^2 m_0 c^2}{U} \cdot \frac{1}{\beta} \cdot \frac{Z}{A} \left[\ln(T/I)^2 + \ln(1+J/2) + F(J) - \delta \right] \quad (2.1)$$

where $F^-(J) = (1-\beta^2) [1 + J^2/8 - (2J+1) \ln 2]$, U is the atomic mass unit, r_e is the classical electron radius, m_0c^2 is the electron rest energy, β is the velocity of the incident electron divided by the velocity of light, Z is the atomic number of the target material, A is the relative atomic mass, I is the mean excitation energy of the medium, T is the kinetic energy of the incident electron, J equals T/m_0c^2 and δ is the density effect correction which gives the reduction in collision energy loss due to the dielectric polarization of the medium. One half the quantity in square brackets in Equation 2.1 is the stopping number per atomic electron, $L(\beta)$. In dosimetry attention is commonly focussed on the energy "imparted to the medium along the path rather than on the energy by the incident electron. Therefore, it is often useful to introduce a restricted mass collision stopping power $L(T, \Delta)/\rho$, as the average collisional energy loss per unit path-length in which the energy transferred to delta-rays is smaller than some chosen limit Δ , which is larger than the binding energies of the atomic electrons in the target material (ICRU 1984b). The formula for the restricted mass stopping power is the same as Equation 2.1 except that the function $F^-(J)$ is replaced by $F^-(J, \eta)$

$$F^-(J, \eta) = -1 - \beta^2 + \ln [4(1-\eta)\eta] + (1-\eta)^{-1} \\ + (1-\beta^2) [J^2\eta^2/2 + (2J+1)\ln(1-\eta)] \quad (2.2)$$

where η is the fractional energy cut-off, Δ/T .

The mass radiative stopping power cannot be given in a simple general form covering all energies and materials. In terms of the dimensionless, scaled, radiative energy-loss cross sections ($\phi_{\text{rad},n}$) and ($\phi_{\text{rad},e}$), the mass radiative stopping power may be written as (ICRU 1984b)

$$\frac{S_{\text{rad}}}{\rho} = \frac{\lambda r_e^2 m_0 c^2 (J+1)}{UA} \left[Z^2 (\phi_{\text{rad},n}) + Z (\phi_{\text{rad},e}) \right] \quad (2.3)$$

where λ is the fine structure constant. The cross sections $\phi_{\text{rad},n}$ and $\phi_{\text{rad},e}$ are given by

$$\phi_{\text{rad},n} = (\lambda r_e^2 Z^2)^{-1} \int_0^{T'} (\epsilon/E) \frac{d\Sigma_n}{d\epsilon} d\epsilon \quad (2.4a)$$

and

$$\phi_{\text{rad},e} = (\lambda r_e^2)^{-1} \int_0^{T'} (\epsilon/E) \frac{d\Sigma_e}{d\epsilon} d\epsilon \quad (2.4b)$$

where T' is the upper limit of the energy of the photons that can be emitted in electron-electron interactions

$$T' = m_0 c^2 T \left[T + 2m_0 c^2 - \beta (T + m_0 c^2) \right]^{-1} \quad (2.5)$$

$E = T + m_0 c^2$, the total energy of the incident electron, $d\Sigma_n/dk$ is

the differential cross section for the emission of a photon of energy \mathcal{E} due to the interaction of the electron with the screened Coulomb field of the atomic nucleus, and $d\Sigma_e/d\mathcal{E}$ is the corresponding cross section due to the Coulomb interaction with one of the atomic electrons.

For compounds the additivity rule is a fair approximation and the total mass stopping power is given by

$$\frac{S_{\text{tot}}}{\rho} = \sum_j w_j [S_{\text{col}}/\rho]_j + \sum_j w_j [S_{\text{rad}}/\rho]_j \quad (2.6)$$

where w_j is the fraction by weight of the j 'th constituent. More accurate values for the total mass stopping power for compounds may be obtained from ICRU report 37 (ICRU 1984b).

2.2.3 Continuous Slowing Down Approximation (CSDA) Range

In this approximation, energy-loss fluctuations are disregarded, and the rate of energy loss at any point along the path is assumed equal to the total stopping power. The CSDA range r_0 (in gcm^{-2}) may then be evaluated by integrating the reciprocal of the total stopping power

$$r_0 = \rho \int_{T_f}^{T_0} [S_{\text{tot}}(T)]^{-1} dT \quad (2.7)$$

from the initial incident electron energy T_0 down to some final energy T_f . The value of T_f is in principle adapted to the purpose for which the range is to be used. For radiation therapy, the value of T_f is normally set equal to zero.

2.2.4 Scattering

Elastic nuclear Coulomb scattering is the primary interaction mechanism causing therapeutic electrons to change direction, with very little energy loss, as they penetrate tissue. The cross section for electron-electron scattering is about a factor of Z less than for the electron-nuclear scattering and hence its overall contribution is relatively small. The therapeutic electrons undergo a large number of multiple nuclear coulomb scatterings as they penetrate tissue due to the long range coulomb potential. The number of large-angle single scattering events is comparatively rare but substantially increase the probability of backscattering and also give a significant contribution to central axis dose in small electron fields.

2.2.5 Single Scattering

The differential cross section per atom for scattering from a pure Coulomb potential through an angle between θ and $\theta+d\theta$ into the solid angle $2\pi \sin \theta d\theta$ was originally derived by Rutherford for non-relativistic energies and an unshielded

nucleus is given by

$$d\Sigma(\theta) = \frac{\pi e^4 Z^2 \sin \theta d\theta}{2 m_0^2 v^4 \sin^4(\theta/2)} \quad (2.8)$$

A more accurate cross section for electrons of relativistic energy and low atomic number materials in the range of biological tissue has been derived by Mott (1929, 1932) and McKinley and Feshback (1948). The ratio of their cross section R to the Rutherford cross section is given by

$$R = 1 - \beta^2 \sin^2(\theta/2) + \pi \lambda \beta \sin(\theta/2) \left[1 - \sin(\theta/2) \right] \quad (2.9)$$

where $\lambda = Z/137 \ll 0.2$.

The contribution of electron-electron scattering may be incorporated in an approximate way by replacing Z^2 by $Z(Z+1)$.

2.2.6 Multiple Scattering

There has been a wealth of scientific literature on the theory of small-angle multiple scattering of charged particles since the Rutherford analysis of alpha particle pencil beam scattering by gold foils. Naively, two angular regimes may be distinguished: a Gaussian distributed small angle regime due to small-angle multiple scattering and a large angle regime domi-

nated by single scattering. Although only approximate, the use of the Gaussian small-angle scattering distribution in electron radiotherapy is widespread due to its simplicity. The probability $P(\theta)d\theta$ of finding an electron from a point monodirectional source travelling with polar angle θ in a scattering medium, irrespective of azimuthal angle, is given in the Gaussian approximation by

$$P(\theta) d\theta = \frac{1}{\pi\overline{\theta^2}} \text{EXP}\left[-\frac{\theta^2}{\overline{\theta^2}}\right] d\theta \quad (2.10)$$

where $\overline{\theta^2}$ is the mean square scattering angle of the electrons and it is necessary only to evaluate $\overline{\theta^2}$ as a function of depth in the scattering medium. This function may be computed from the probability of single scattering, by considering the multiple scattering events in a layer of tissue to be the result of many independent single scattering events (Brahme 1971). The central limit theorem can then be applied to derive value of $\overline{\theta^2}$ and hence the mass angular scattering power (Section 2.2.7).

The small-angle scattering distribution is not Gaussian. The true distribution is more forward peaked at very small angles and lies above the simple Gaussian at larger angles due to the single scattering tail. The theory of Moliere (Scott

1963) is commonly used for more accurate calculations of the angular distribution when electron energy loss can be neglected. In this theory, the solution for the angular distribution is a series in which the first term is Gaussian and other terms are correction functions. Brahme et al (1981) have shown that it is possible to find a narrower Gaussian distribution which fits the central portion of the true angular distribution better than the Gaussian component of the Moliere theory.

$$\overline{\theta^2}_{1/e} = \left[1 - 1.33/B\right] \cdot \overline{\theta^2}_M \quad (2.11)$$

where $\overline{\theta^2}_{1/e}$ is the angle at which the true distribution falls to 1/e of its value at zero angle, $\overline{\theta^2}_M$ is the mean square angle of the Gaussian term in the Moliere series and B is a form factor related to depth in the scattering medium and defined by the Moliere theory. The value of $\overline{\theta^2}_M$ may also be related to the $\overline{\theta^2}$ of simpler pure Gaussian theories of small-angle multiple scattering.

Recently Peterson (1983) has applied the general theory of random walks on group spaces to the problem of angular distribution in multiple elastic scattering and obtained an exact solution for all angles. He states that "... the reason the forward distribution in multiple scattering is non-Gaussian is

that it arises as a random walk in a non-Euclidean space, whereas the central-limit theorem is associated in an essential way with random walks in Euclidean spaces and more particularly with the Euclidean translation group".

2.2.7 Mass Angular Scattering Power

The mass angular scattering power k/ρ is defined as the increase in mean square angle of scattering ($\overline{d\theta^2}$) per unit thickness (ρds) in terms of the mass traversed per unit sectional area (ICRU 1984, ICRU 1972, Brahme 1971).

$$\frac{k}{\rho} = \pi \left[\frac{2r_e Z}{(J+1)\beta^2} \right]^2 \cdot \frac{N_a}{M_a} \left\{ \ln \left[1 + \left(\frac{\theta_m}{\theta_\mu} \right)^2 \right] - 1 + \left[1 + \left(\frac{\theta_m}{\theta_\mu} \right)^2 \right]^{-1} \right\} \quad (2.12)$$

where θ_m is the cut-off angle due to the finite size of the nucleus. It is given by the ratio of the reduced de Broglie wavelength of the electron to the nuclear radius

$$\theta_m = \frac{2A^{-1/3}}{\lambda\beta(J+1)} \quad \text{for } \theta_m < 1 \text{ radian, } \theta_m = 1 \quad (2.13)$$

The screening angle, θ_μ is due to the screening of the nucleus by the orbital electrons. It is given by the ratio of the reduced de Broglie wavelength of the electron to the atomic radius

$$\theta_\mu = \frac{1.13 \lambda Z^{1/3}}{\beta(J+1)} \quad (2.14)$$

The contribution from electron-electron scattering may be approximated by replacing Z^2 by $Z(Z + 1)$ in Equation 2.12. The expression for mass angular scattering power accounts for large angle scattering up to θ_m , and may lead to systematic errors when incorporated into small-angle multiple scattering theories. Andreo and Brahme (1984) have defined a restricted mass scattering power in which θ_m is replaced by a cut-off angle γ to exclude deflection angles larger than this angle. They recommend a value for γ of 0.5 radian, on the basis of Monte Carlo data, to avoid a variation in results due to large angle single scattering events.

2.3 Characteristics of therapeutic beams

2.3.1 Dose

The absorbed dose $D(\vec{r})$ at a point \vec{r} is the energy deposited per unit mass at the point. In a pure electron field

the dose is given by (ICRU 1984a)

$$D(\vec{r}) = \frac{-1}{\rho(\vec{r})} \int_{4\pi} \int_0^{\infty} \left\{ \frac{dE(\vec{r})}{ds} \cdot \Phi_{E, \vec{\Omega}} + E(\vec{r}) \cdot \frac{d\Phi_{E, \vec{\Omega}}}{ds} \right\} dE d\Omega \quad (2.15)$$

where $\Phi_{E, \vec{\Omega}}$ is the electron fluence differential in energy and angle, E is the electron energy, $\vec{\Omega}$ is the unit vector in the direction of the electron motion, s is the pathlength traversed per unit area along the direction of the electron motion and $\rho(\vec{r})$ is the mass density at the point \vec{r} . The second term in brackets is the small contribution from electrons that stop within an interval ds (track-ends) and may be treated as a correction. The first term is the contribution from electrons that pass completely through the interval ds and thus only deposit a fraction of energy in that interval.

For broad uniform electron beams incident upon homogeneous media, and assuming delta-ray equilibrium, the dose at depth z may be approximated by

$$D(z) = \Phi(z) \cdot \frac{S_{col}(E)}{\rho} \quad (2.16)$$

where the mass collision stopping power has been assumed a linear

function over the electron energy spectrum and evaluated using the mean energy of the electrons at depth and $\Phi(z)$ is the primary electron fluence integrated over all energies and angles.

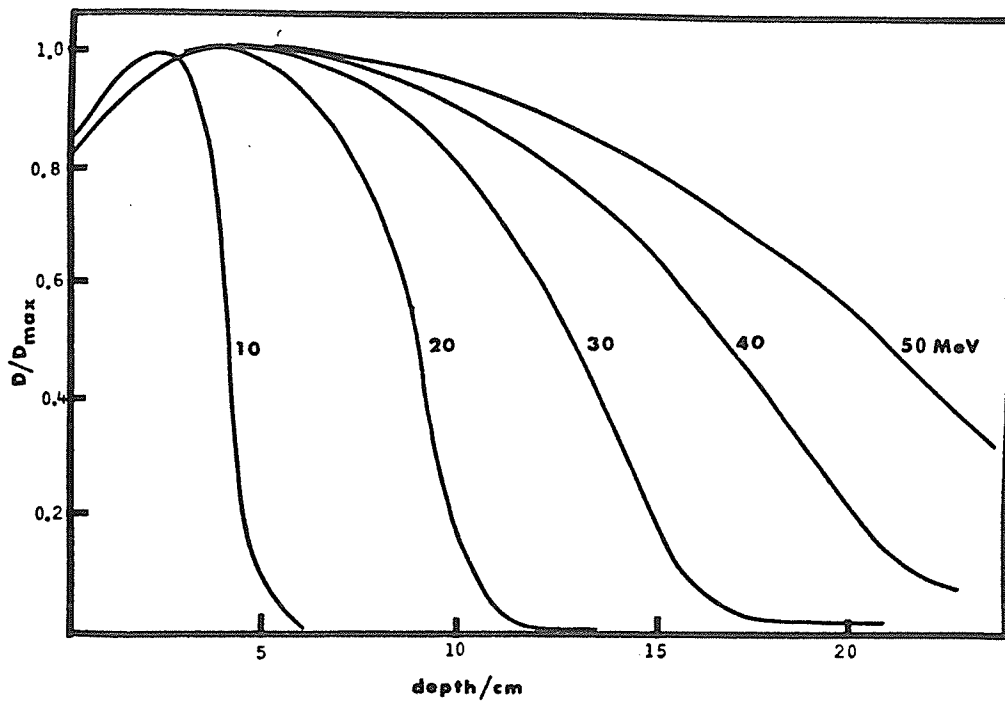
2.3.2 Depth Dose Curves

The therapeutic use of high energy electrons is advantageous because of their rapidly descending dose gradient with depth. The typical variation of absorbed dose with depth in a water medium along the central axis of a field, is shown in Figure 2.1 for several high energy broad electron beams. In this figure the absorbed dose is expressed as a percentage of the maximum dose for a given curve. The increase in dose from the surface to the dose maximum is known as "build-up" and is due to the increased skewness of the electron paths with depth. The increased skewness is caused mainly by elastic scattering interactions which increase the electron fluence and hence the absorbed dose. The fluence $\Phi(z)$ at depth z is related to the incident fluence $\Phi(0)$ at the surface for broad parallel electron beams by (Brahme 1975, Brahme 1981):

$$\Phi(z) = \Phi(0) / \langle \cos \theta \rangle \quad (2.17)$$

where θ is the angle between the direction of travel of the electron $\vec{\Omega}$ and the initial beam direction. This may be approximated at shallow depths using the small angle approximation of

Figure 2.1: Central Axis depth dose curves in water for therapeutic beam of energy in the range 0 - 50 MeV.



$\langle \text{Cos}\theta \rangle$ to be

$$\Phi(z) = \Phi(0) \left[1 + \frac{1}{2} \overline{\theta^2} \right] \quad (2.18)$$

where $\overline{\theta^2}(z)$ is the mean square scattering angle. Therefore the dose build-up is due to $\overline{\theta^2}(z)$ and increases with the atomic number of the medium and a reduction in beam energy. The rapid decrease in dose at depths beyond half the electron range is due to absorption, energy straggling and range straggling of electrons reducing the value of $\Phi(z)$ (Brahme and Svensson 1976)

2.3.3 Practical Range, R_p

The practical range is defined (ICRU 1984a) as the point where the tangent at the steepest point (the inflection point) on the almost straight descending portion of the depth versus absorbed dose curve (for a broad beam) meets the extrapolated bremsstrahlung background. Most measurements of R_p are based on depth-ionization curves.

2.3.4 Field Size and Isodose Curves

The size of a therapeutic electron beam must be variable to both cover the tumor or target and also minimize dose to surrounding normal tissue. This is achieved by using moveable high atomic number collimation in the accelerator treatment head to form a rectangular or circular beam. Shaping of this regular beam to accurately follow the spatial distribution of the target

volume requires additional collimation. This usually takes the form of a lead sheet in which a hole is cut to the desired shape of the treatment portal.

Isodose curves are essentially a two-dimensional map of dose contours and provide dose information at points off the central axis of the beam (Figure 2.2). It is common practice in treatment planning to enclose the target volume within the 80% or 90% isodose curve.

2.3.5 Inhomogeneities

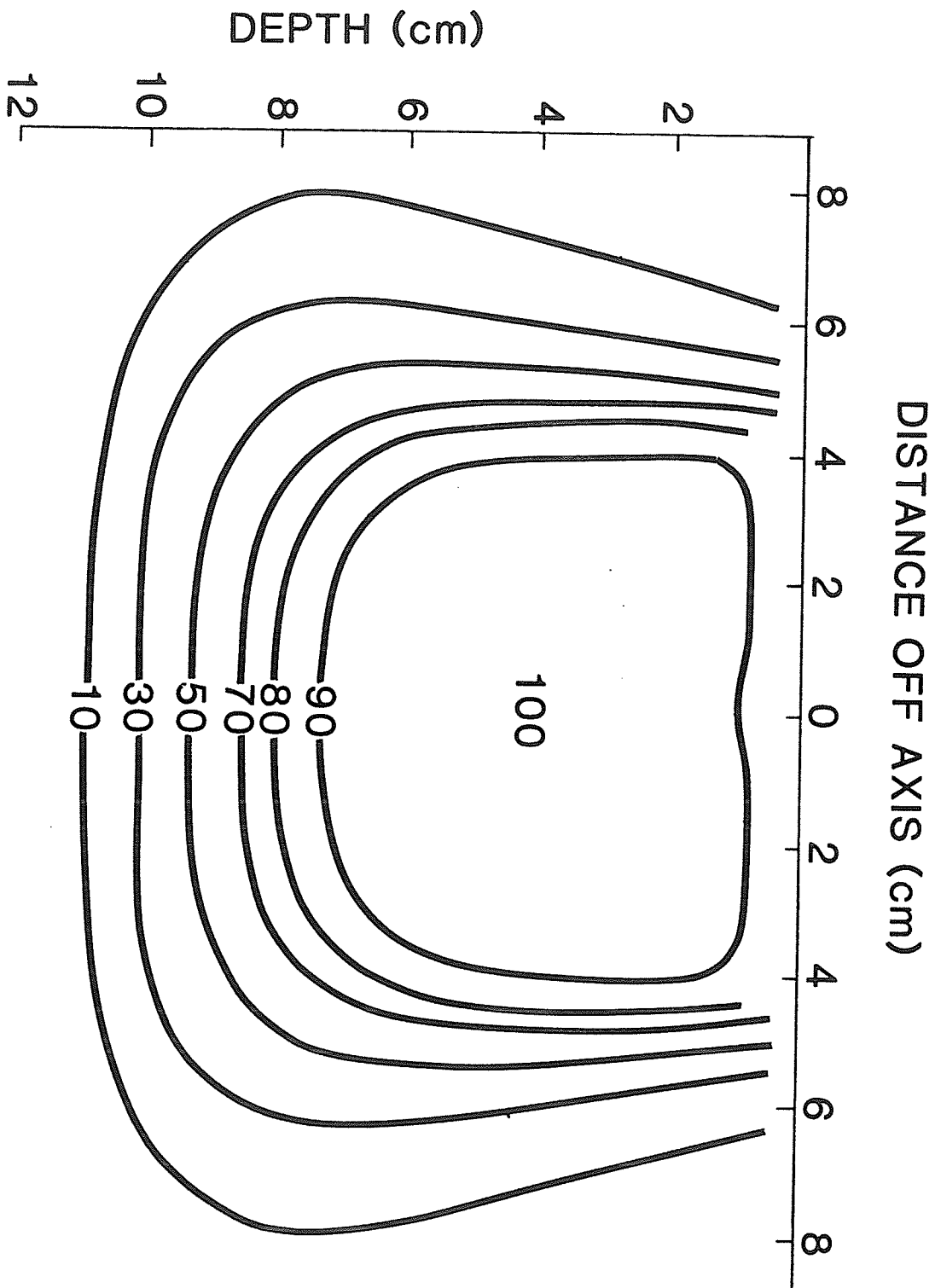
Inhomogeneities are media within the patient which have a density or atomic number that is substantially different from that of water. The principal inhomogeneities are bone, lung and air and their presence serves to distort the isodose distribution in the patient from the isodose distribution obtained in a uniform water medium.

The collision stopping power S_{col} is proportional to the electron density of the medium and is a slowly varying function of energy at high electron energies (MeV).

$$S_{col} \propto \frac{\rho_e L(\beta)}{\beta^2} \quad (2.19)$$

where ρ_e is the electron density (electrons cm^{-3}), β is the ratio of the electron velocity to that of light and $L(\beta)$ is the

Figure 2.2: Typical isodose curves in water for a 22 MeV electron beam.



stopping number per electron. Because of this relationship the penetration of an electron is primarily dependent upon the electron density of the tissues along its path. Table 2.1 lists the electron density and effective atomic number of media commonly encountered. From this data it can be deduced that bone will retard the penetration (in centimeters) of a given electron whereas air or lung will enhance the electrons range relative to that in a homogeneous water medium.

The extent of lateral scattering of an electron with depth depends upon the angular scattering power of the medium. The linear angular scattering power k is directly proportional to the electron density and atomic number of the medium.

$$k \propto \frac{\rho_e Z}{\beta^2} \quad (2.20)$$

where Z is the atomic number of the medium. Therefore the extent of lateral scattering in terms of unit electron mass thickness (electrons cm^{-2}) is increased in bone and air media relative to water.

Table 2.1

Physical properties of media
encountered in patients

Medium	Density (gcm^{-3})	Electron Density (ecm^{-3})	Relative Electron Density	Effective* Atomic Number
Water	1.00	3.343×10^{23}	1.000	6.60
Air	0.0012	0.004×10^{23}	0.0011	7.36
Muscle	1.06	3.440×10^{23}	1.029	6.57
Lung	0.32	1.060×10^{23}	0.317	6.57
Bone	1.65	5.800×10^{23}	1.735	8.76

* Calculated as $Z = \sum_i f_i Z_i$ where f_i is the fraction by electron number of element i of atomic number Z_i

Chapter 3

REVIEW OF DOSE COMPUTATION ALGORITHMS

3.1 Introduction

The important physical and clinical advantages of high energy electron beams compared to photon beams has not been fully exploited. This is due to the lack of an electron dose computation algorithm which can accurately predict dose in all clinical situations to within 5%. The older dose computation algorithms available in the sixties and seventies were broad beam approaches requiring a formidable quantity of measured data as input and therefore did not achieve widespread use. During the last decade computer algorithms have been under development which may account for body contour and the physical properties of the various tissues encountered in patients. This is achieved by considering the broad therapy electron beam to be comprised of the summation of many narrow pencil beams. The dose contribution from each elemental pencil beam can be described empirically or analytically and the total dose obtained by summation over all pencils. The most advanced clinically available pencil beam algorithm was introduced by Hogstrom et al (1981). Yet this algorithm can still produce errors in computed dose of up to 40% in clinically realistic situations (Cygler et al 1987). A major obstacle to the further development of accurate pencil beam dose computation algorithms is the lack of an analytical approach which can comprehensively include interaction processes other than small-angle multiple

scattering.

This Chapter presents a review of the dose computation algorithms used in radiotherapy. Broad beam approaches to dose calculation have been categorized and briefly discussed under the sub-headings empirical, Boltzmann transport equation, age diffusion equation and inhomogeneities. Several reviews of these broad beam approaches to dose calculation are also available in the literature by Sternick (1978), Nusslin (1979), Andreo (1985b) and Jette (1985a).

Pencil beam approaches to dose calculation have been reviewed in greater detail under the sub-headings empirical, analytical and inhomogeneities. State of the art reviews of the pencil beam approach at that time have been published by Hogstrom (1982) and Brahme (1985). The most recent developments have been included in this review.

3.2 Broad Beam Approaches to Electron Dosimetry

3.2.1 Empirical Methods

The introduction of electron accelerators to radiotherapy over thirty years ago, required that the dose at depth in tissue be known for each electron energy and field size available. Most important is the variation of dose with depth on the central axis of the therapy beam and commonly this is then multiplied at each depth by an off-axis ratio (OAR) which describes the

variation of dose at lateral positions away from the central axis. Laughlin et al (1953) were the first to provide an equation describing depth dose in water.

$$D(z) = 110 - 10 \text{ EXP} [\xi(z-z_m)] \quad (3.1)$$

where $D(z)$ is the percentage dose as a function of the depth z , z_m is depth of maximum dose and ξ is an empirically variable parameter adjusted for a best fit to measured data at depths greater than z_m . For unit density material, Bagne (1976) modified Laughlin et al's equation to include an extra degree of freedom which allowed closer fits to measured data for beam energies above 20 MeV. Other analytical expressions for describing central axis depth dose at depths greater than the dose maximum have been proposed by Czaikowsky (1972), Pacyniak and Pagnamenta (1974), Fehrentz (1977), Shabason and Hendee (1979), Ueda (1979) and Jette et al (1981). More recently, Strydom (1984) provided a modified form of the equation proposed by Shabason and Hendee (1979) which can be used to fit experimental data within 3% in the build-up region of the depth dose curve. All these analytical formulas are only useful for interpolation between measured data points.

The next step for empirically describing dose distributions in homogeneous media is to find a function for the off-axis ratio to characterize the distribution in two dimensions. Edwards and Coffey (1979) used the shape of the cumulative normal distribution function to describe the off-axis ratios (OAR) for large electron fields and Equation 3.1 for the central axis dose. Originally this function for the OAR was used because it had been successfully applied by Sterling et al (1964) to cobalt 60 beams.

$$\text{OAR} = \frac{1}{2} \left[1 - \text{ERF} \left(\frac{x-L}{\sqrt{2} \sigma} \right) \right] \quad (3.2)$$

where L is the half width of the field, x is the off-axis distance and σ is a fitting parameter found to be proportional to penumbra width. In retrospect the success of this function for electron fields is not surprising since it is exactly the same form that would be described by a Fermi-Eyges pencil beam integrated over the field area (described later in this chapter).

Other empirical approaches to the 2-dimensional representation of electron dose distributions in regular shaped fields have been proposed by Fehrentz et al (1977) and Tronc and Levailant (1978). Their algorithms require 5 or more fitting parameters to be optimized and do not

give an improvement over the simple OAR proposed by Edwards and Coffey (1979).

3.2.2 Boltzmann Transport Equation

Lewis (1950) presented a theoretical treatment of electron penetration in a scattering medium based on the Boltzmann equation and the continuous slowing down approximation. This equation was solved using the method of moments, which consists of forming a series representation of the angular flux, $F(E, \vec{r}, \vec{\Omega})$, using Legendre polynomials. Substituting this expansion into the transport equation, multiplying this equation by the appropriate set of orthonormal Legendre polynomials, and integrating over 4π steradians produces a coupled set of integro-differential equations in space and energy E in terms of Legendre coefficients. The spatial variable r in this set of equations may then be eliminated by applying spatial moments of the form Fx^n to the transport equation. This system of equations may then be solved for the moments and the desired depth dose reconstructed. The moment technique was later developed in its application to electron therapy by Spencer (1955), Awadi (1957), Kessarlis (1964), Kessarlis (1966), Kessarlis (1970), Liaw (1977) and Luo (1982).

3.2.3 The Age Diffusion Approximation

The age diffusion equation describes the electron

fluence at depth in a homogeneous medium under the assumption of isotropic scattering, the continuous slowing down approximation (CSDA) and no delta-ray production. The equation may be written as

$$\frac{\partial D(\vec{r}, \tau)}{\partial \tau} = K \nabla^2 D(\vec{r}, \tau) \quad (3.3)$$

where τ is the age parameter, \vec{r} is the position vector, D is the dose, K is a diffusion coefficient and ∇^2 is the Laplacian operator.

Kawachi (1975) was the first to present a solution to the Age Diffusion equation for the purpose of electron treatment planning by computer. His solution was obtained for a semi-infinite homogeneous phantom irradiated by a monoenergetic, parallel electron beam of rectangular field area. Only the two dimensional problem in lateral position x and depth z was considered, which is equivalent to considering the field length in the y direction infinite. The solution proposed by Kawachi is

$$D(z, x, \tau) = D_0 \left[\frac{SSD}{SSD+z} \right]^2 \left[\text{ERF} \frac{(a-x)}{2\sqrt{K\tau}} + \text{ERF} \frac{(a-x)}{2\sqrt{K\tau}} \right] \cos \left[\frac{2\pi z}{3R_p} - \frac{\pi}{6} \right] \cdot \text{EXP} \left[- \left\{ \frac{2\pi \sqrt{K\tau}}{3R_p} \right\}^2 \right] \quad (3.4)$$

where the inverse square law has been artificially substituted to account for beam divergence, D_0 is a normalization constant, a is half the field length in the x-direction at depth z for the diverging beam, R_p is the practical range and

$$\sqrt{K\tau} = \left(C \frac{z+P}{R_p} \right)^N \quad (3.5)$$

where C, P, N are empirical constants.

Inspection of this solution reveals that, for a field which is also infinite in the x-direction the error function terms become unity and therefore all the other terms in the solution simply describe the depth dose distribution for an infinite-sized field. Steban et al (1979) introduced error function terms in the second lateral dimension for fields of finite size in the y-direction and, except for an empirically variable factor to the field dimension to achieve improved fits to measured data, simply added a quadratic term to the argument of the cosine for closer agreement with experimental depth dose data. The inclusion of extra quadratic terms means that Equation 3.3 is no longer satisfied. Millan et al (1979) generalized the quadratic terms in the argument of the cosine to

$$\text{Cos} \left[\sum_{i=1}^n G_i (z/R_p)^{i-1} \right] \quad (3.6)$$

where $n = 5, 6$ or 7 for the parameterization of beams from a Sagittaire Therac 40 accelerator.

There have been other attempts to modify the original Kawachi solution. Nusslin (1979) proposed taking the brehmsstrahlung background into account by separating out photon and electron components to the dose while Pacyniak and Pagnamenta (1977) attempted to account for the generation of delta-ray electrons, by separately considering the contribution of primary and delta-ray electrons to the total dose as a function of depth z and age τ . To date there have been no further modifications to the original solution.

Luo (1982) attempted to improve the electron age-diffusion theory by considering the electrons undergoing small-angle scattering separately from diffusive electrons. Any large-angle scattered electrons from the small-angle scattering group are subtracted and considered secondary sources of diffusive electrons. The linearized Boltzmann equation is then used to compute the energy deposition by both groups of electrons. This approach is very complex and has only been applied by Luo (1982) to electrons of energy below 0.5 MeV. However, Luo states that the method has the potential of being applied to the calculations of electron energy deposition in the inhomogeneous media.

3.2.4 Inhomogeneous Media

Several broad beam approaches to computing dose in inhomogeneous media were developed in the 1960's and 1970's. The Dose Shifting Method (Pohlit 1960, Pohlit 1969), the Absorption Equivalent Thickness method (Laughlin et al 1953, Laughlin 1965, Laughlin et al 1965), the Absorption Coefficient method (Dahler et al 1969), the Coefficient of Equivalent Thickness method (Almond et al 1967, Boone et al 1967, Boone et al 1969) and the Modified Absorption Coefficient method (Bagne 1976), are all based on shifting a measured dose distribution in a uniform water phantom according to some physical relationship between the inhomogeneity and water (eg. density). The corrections are for large slab-type inhomogeneities and are only applicable to the central region of the beam. Extension to two or three dimensions is achieved by using ray projections from a "virtual" source and shifting the water reference dose according to the inhomogeneities encountered along these rays. Further correction factors are included for patient curvature, changes in SSD and the penumbra region of the beam, in addition to the variation of the basic parameters with beam energy and field size (Holt et al 1978).

The methods discussed above are unable to account for

scattering of electrons from the edges of inhomogeneities. Pohlit and Manegold (1976) suggested an empirical approach to this problem in which angles describing the maximum dose perturbation from the edge and the limit of the area influenced by electrons scattered from the edge are determined. The dose distribution is then corrected along these angles. Abou-Mandour and Harder (1978) used an alternative method of Partial Beam Substitution in which the total broad beam is divided into a number of smaller partial beams just encompassing the inhomogeneities. The dose distribution of the partial beam incident upon the inhomogeneity is corrected according to the isodose shift method (Harder and Abou-Mandour 1976) and additional corrections allow for the differential scattering properties of the inhomogeneity compared to water. This method is similar in principle to the pencil beam approach discussed later in this Chapter.

Recently, Brahme and Lax (1983) have defined water equivalent thickness for large slab inhomogeneity corrections in two ways. The thickness of water that produces the same amount of energy loss, or the thickness of water that produces the same mean square angular spread as an inhomogeneity. A universal scaling factor Γ is available for the dose and depth axis of a depth dose curve for lung

inhomogeneities (I) which have the same atomic number as water (W) but are of different density

$$R = \frac{S_{\text{tot,I}}}{S_{\text{tot,W}}} = \frac{k_I}{k_W} \quad (3.7)$$

where S_{tot} is the total linear stopping power and k is the linear angular scattering power. When the mean atomic number is different from that of water, two ways of inhomogeneity correction in the build-up region of a depth dose curve may be performed. Either the equivalent thickness of water t_e that produces the same amount of energy loss is used and corrected for the error in the angular spread $\Delta\bar{\theta}^2$

$$t_e = \frac{S_{\text{tot,I}}}{S_{\text{tot,W}}} \quad ; \quad \Delta\bar{\theta}^2 = \bar{\theta}_I^2 \cdot \left[\frac{1 - k_W \cdot S_{\text{tot,I}}}{k_I \cdot S_{\text{tot,W}}} \right] \quad (3.8)$$

where $\bar{\theta}_I^2$ is the increase in mean square scattering angle produced by the inhomogeneity, or the equivalent thickness of water t_s that produces the same mean square angular spread of the inhomogeneity is used and corrected for the error in the energy loss $\Delta\bar{E}$

$$t_s = \frac{k_I \cdot t_I}{k_W} \quad ; \quad \Delta\bar{E} = \bar{E}_I \cdot \left[1 - \frac{k_I \cdot S_{\text{tot,W}}}{k_W \cdot S_{\text{tot,I}}} \right] \quad (3.9)$$

where t_I is the thickness of the inhomogeneity and \bar{E}_I is the mean electron energy loss in the inhomogeneity.

3.3 Pencil Beam Approaches to Electron Dosimetry

3.3.1 Empirical Methods

Rozenfeld et al (1969) and Nath et al (1980) utilized the dose distribution data for a non-scanned accelerator electron beam to reproduce broad beam dose distributions. This was achieved by the development of algorithms which mimic the magnetic scanning action of their machines.

Elementary pencil beams may be produced from broad beams by collimation. Lillicrap et al (1975) produced an elementary circular pencil beam of 2.5 cm diameter using an evacuated collimation system. Measurements of dose in a perspex phantom along profiles at various depths and along the central of this pencil beam for 4 and 10 MeV energies were stored in a computer and used to generate broad beam distributions by summation over the broad beam area. The agreement between measured broad beam isodose distributions and those generated from the pencil beam data was good only when the radial profiles were normalized to the central-axis depth dose values measured in the broad beam.

Puel (1981), Abou-Mandour et al (1983), and McParland and Cunningham (1986), measured values of pencil beam spread directly from the dose distributions of small radii pencil beams produced by collimating a broad beam. This

simple method was shown to give results in fair agreement with Monte Carlo data over about the first two thirds of the electron range but at greater depths discrepancies arose.

Brahme et al (1981) produced a 2 mm diameter, almost monodirectional, pencil beam from the accelerator beam of a microtron using magnetic quadrupole focussing to avoid collimator produced bremsstrahlung. Their experimental results were in good agreement with Monte Carlo data for an initially point monodirectional, monoenergetic pencil beam of 22.5 MeV.

The integration of a pencil beam distribution over a line results in a narrow strip beam. McKenzie (1979) used empirical measurements on an elementary strip beam of 10 MeV energy to reconstruct the dose distribution from a broad beam incident at an oblique angle of 45° . He showed that this approach reproduced the measured data more accurately than the isodose shift method. However, for more extreme angles of incidence, strip beams less than the chosen 5 mm width are required for good agreement with measured data. Werner et al (1982) derived a semi-empirical method for obtaining pencil beam spread using a slit beam dose distribution method. Ekstrand and Dixon (1982) employed the approach of Werner et al (1982) to

examine the effects of irradiating an oblique surface with 6 MeV and 9 MeV electron beams. They showed that the central axis dose at shallow depths increased while the dose at normal treatment depths (80% isodose level) decreased. This effect was explained simply on the basis of slit beams. As oblique incidence increases, a point at shallow depth has an increased net gain of low energy electrons from adjacent slit beams.

3.3.2. Analytical Methods

Current analytical pencil beam approaches to broad beam electron dose computation are based on the pencil beam solution to the Fermi transport equation (Fermi 1941, Eyges 1948, Brahme 1975). Osman (1976) and Osman (1977) was the first to consider a broad therapeutic electron beam as composed of an infinite number of initially parallel and identical Gaussian pencil beams undergoing small-angle multiple scattering. He demonstrated that this approach could be used to compute dose distributions in homogeneous media using fluence decrement curves if the measured central axis dose data for the field considered was included as a normalization parameter.

The pencil beam solution to the Fermi transport equation does not reflect the true angular and radial distribution of a pencil beam (Scott 1963, Brahme 1971).

The true distributions at shallow depths in tissue are narrower than the Gaussian predictions at small angles and radii and broader at large angles and radii due to large-angle single scattering and delta-ray production. At depths over half the electron range the large-angle tail is lost due to absorption of the electrons which have undergone this type of scattering in the shallow depth region, and the angular and radial distribution is well predicted by a single Gaussian. The mean square radial spread of this single Gaussian decreases at depths close to the electron range due to range straggling. Brahme et al (1981) attempted to include large angle scattering events at shallow depths by describing the radial distribution of the pencil beam as a sum of three Gaussians rather than the single Gaussian

$$\Psi(r,z) = \sum_{i=1}^3 a_i \text{EXP}(-r^2 / b_i \bar{r}^2) \quad (3.10)$$

where a_i and b_i are depth dependent fitting parameters and \bar{r}^2 is the mean square radial spread. This distribution is based on the work of Nigam et al (1959) and Marion and Zimmerman (1967) which neglects range straggling and energy degradation of the electrons. Lax et al (1983) included all interaction processes by obtaining the

fitting parameters for the radial profiles from Monte Carlo data for point monidirectional beams in water. Range straggling effects at large depths causing a reduction in the mean square radial spread were taken into account by modulating the parameter b_1 with an empirical factor $Q(z)$ which was close to unity at shallow depths. This parameter fits the total absorbed dose including bremsstrahlung

$$Q(z) = \text{EXP} \left[-R^{12(1.5-R)} \right] \quad (3.11)$$

where $R = 0.95z/R_p$, R_p is the practical range of the electrons and z equal the depth. Lax et al (1983) showed that this Generalized Gaussian approach was superior to the single Gaussian in its predictions of small field central axis depth dose distributions from large field central axis depth dose data in water.

Werner et al (1982) measured the root mean square radial spread of a pencil beam from a strip beam. Their approach was based on Fermi-Eyges theory and they showed that measured values of pencil beam spread decreased to zero at the end of the electron range due to range straggling. The measured values of pencil beam spread, $\sigma(z)$, in water equivalent materials could be well fit by assuming all electrons scattered greater than some criti-

cal angle θ_{\max} are absorbed locally. The critical angle adopted for a best fit was $\pi/4$.

$$\sigma(z) = \sigma(z)_{FE} \operatorname{ERF} \left[\frac{\theta_{\max}}{\sqrt{2 \overline{\theta^2}(z)}} \right] \quad (3.12)$$

Interestingly, and quite coincidentally, this value for θ_{\max} corresponds exactly with the saturation value of 0.775 radian for the root mean square angular spread of electrons in thick homogeneous media measured by Roos et al (1973).

Bruinvis et al (1983) used Fermi-Eyges theory for dose computation in irregularly shaped fields. They employed different values of pencil beam spread for the central axis and penumbra regions, which in an unphysical way introduced an extra degree of freedom allowing closer fits to experimental data.

A basic assumption in Fermi-Eyges small angle scattering theory is that the path length travelled by electrons is equal to the depth in the scattering medium. This assumption is increasingly invalid with an increase in depth in the medium since the electrons on average in a pencil beam travel along skewed paths rather than straight lines. Andreo and Brahme (1981) have shown using Monte Carlo calculations that the average energy of the electron off the central axis of the pencil beam is reduced because

of the increase in path length on the average to get to an off-axis point. Jette (1985) has attempted to theoretically include the skewness of the electron path by retaining second-order terms in the Taylor series expansion of Equation 4.10 Chapter 4. The resulting transport equation is an inhomogeneous second-order differential equation. The solution to this equation under pencil beam boundary conditions is highly complex in comparison to the first order solution, but has the advantage that it will predict the component of build-up in broad beams due to the skewed path of the incident electrons in tissue.

3.3.3 Inhomogeneities

Goitein (1978) showed that the small-angle scattering Gaussian approximation of multiple scattering theory was capable of accurately predicting the characteristic "hot" and "cold" spot fluence perturbations observed beyond thin inhomogeneities (Pohlit and Manegold 1976). Analytical solutions for the fluence distribution beneath a single straight edge discontinuity in a large uniform parallel beam, demonstrated that the maximum perturbation was 50% and reduced as the difference in scattering power between the inhomogeneity and adjacent tissue decreased. In a companion paper Goitein et al (1978) showed the good agreement obtained between fluence perturbation data

measured behind edge inhomogeneities and the theoretical calculations for proton and electron beams. He also showed that the maximum perturbation for a single inhomogeneity-soft tissue interface could be increased by reinforcement from another inhomogeneity-soft tissue interface close by. Clinically this situation arises with small three-dimensional inhomogeneities or irradiation of the ribs. The perturbation of fluence in more complex geometries such as slant edged or sliver inhomogeneities require computer calculations. Goitein and Sisterson (1978) used Monte Carlo calculations to examine the effect of thin sliver inhomogeneities. They showed that the multiple scattering phenomenon imposes a limit to the size of structures which can cause significant dose perturbations. If the slivers are narrow, multiple scattering effects reduce their influence and it is adequate to measure the average density within a small volume and unnecessary to consider the details of structure within that volume.

Perry and Holt (1980) introduced a concept whereby the scattering of electrons from a pencil beam incident upon an inhomogeneous medium are represented by curved mean paths. These mean paths are computed on the basis of the Gaussian small-angle scattering approximation and

represent those electrons contained within a small volume about the mean path. The width at any depth of the profile of this volume is much smaller than the pencil beam itself. Contributions to dose, at a point, of the electrons moving along such paths through inhomogeneous tissue is computed by considering the electrons to encounter infinite slabs having the same projected intersections.

Hogstrom et al (1981) introduced a pencil beam algorithm for dose computation in inhomogeneous media which is currently commercially available. The algorithm considers the broad electron beam to be composed of ideal Fermi-Eyges pencil beams and employs the semi-infinite slab approximation for the inhomogeneous material encountered by the central axis of each pencil beam. Anatomical and tissue electron density information provided by a single x-ray computed tomography (CT) scan along the central plane of the beam is used for dose calculations. Anatomy on adjacent CT planes is considered identical to the central plane and therefore the dose calculations are two-dimensional. Electron density information is correlated to CT number, and to the ratios of linear stopping powers and linear angular scattering powers of tissue media to water. These relationships are used to scale the

depth dose on the central axis of a pencil beam penetrating inhomogeneous tissue from a water depth dose curve. The effective depth z_{eff} in water having approximately the same mean energy of electrons as the depth z in the inhomogeneous tissue is

$$z_{\text{eff}} = \int_0^z \frac{S_{\text{col,medium}}}{S_{\text{col,water}}} d\epsilon \quad (3.13)$$

where S_{col} is the collision stopping power. The mean energy at depth z is given by Harders equation (Harder 1964) and this energy determines the linear scattering power of the inhomogeneous tissue at depth z to that of water.

Lax and Brahme (1985) and Lax (1985) extended their Generalized Gaussian beam method from homogeneous to inhomogeneous media using the semi-infinite slab approximation for the central ray of the pencil beam. At present the algorithm is two-dimensional in that the patient anatomy in the central treatment plane is considered to extend across the whole beam width. On the basis of the small angle scattering approximation relationships are derived that scale dose distribution data from water to other homogeneous material in terms of scattering power and stopping power (Brahme 1975). Lax and Brahme (1985) show that these scaling laws hold even for scaling the pencil beam Monte Carlo data of Berger and Seltzer (1982).

A recent numerical pencil beam approach introduced by Storchi and Huizenga (1985) and Storchi and Huizenga (1986) improves upon the dose computation algorithm of Hogstrom et al (1981) by allowing the linear angular scattering power k for a pencil beam to be dependent on both the depth z in the medium and radial position r . Therefore, the semi-infinite slab approximation is not required. This algorithm is based on Fermi-Eyges theory and uses a procedure based on the moment method. They show that approximating the angular distribution at a point in a broad beam to be Gaussian and convolving this with the Gaussian scattering function for small angle scattering leads to the distribution function for the broad beam in direction, lateral position and depth. The moments of this function with respect to the direction of travel are used to compute the spatial distribution, mean angle of travel of the electrons at a given depth, and lateral position and mean square angle of travel at the same point. Each pencil beam at a depth z may then be propagated through the scattering medium to a depth $z + \Delta z$ and a new set of pencil beams redefined at this depth. This process is repeated for all depths up to the range of the electrons. In a comparison of this numerical approach with the algorithm due to Hogstrom et al (1981) for a

parallel beam of 13 MeV electrons incident upon a step water phantom, the numerical method gives a sharper hot spot than the Hogstrom et al algorithm in agreement with experimental results. The numerical approach has recently been extended by Storchi and Huizenga (1986) to empirically incorporate interaction mechanisms secondary to small-angle multiple scattering by using measured electron depth dose data. This is achieved by multiplying the convolution kernel with a function $(1 + \Delta q(E))$, where E is the mean electron energy in point r at depth z and the function $q(E)$ is calculated from the central axis dose of an infinitely broad beam in water $g(z)$.

$$q = \frac{d}{dz} [\ln g(z)] \quad (3.14)$$

The function q is related to the local mean electron energy and may be used to incorporate the effects of a spectrum of electron energies at the same depth introduced by inhomogeneities.

3.4 Discussion

Empirical broad beam approaches to computing dose in homogeneous media are very limited because, in common with all empirical approaches, they lack predictive power for changes in treatment conditions. Analytic expressions for central axis depth dose data are only useful for interpolation between measured data points. While, off-axis ratio (OAR) expressions are

restricted to rectangular or circular fields and require a large quantity of measured input data to optimize free variables. Therefore empirical broad beam approaches to electron dose computation offer little advantage over simply storing the measured data and using it for treatment planning.

Analytical descriptions of central axis depth curves using solutions to the Boltzmann Transport equation derived by the moment method are limited to ideal beams (for example, a monoenergetic and monodirectional electron beam of uniform incident intensity with linear dimensions much larger than the electron range, incident upon a homogeneous semi-infinite scattering medium). In addition to these initial constraints, an infinite number of moments are needed to reconstruct a unique flux, but in practice a finite number are used and the solution is therefore not unique. Further because of the series expansions used, many terms are required to describe deep-penetration trends and similarly it is difficult to treat backscattering or regions near the source. These limitations prevent use of this technique for treatment planning. However, the technique is an important analytical aid to understanding the behaviour of electrons penetrating tissue and provides tests for Monte Carlo techniques.

Describing the penetration of therapeutic high energy electrons in low atomic number tissues by the Age Diffusion

transport equation is wrong for almost all depths. The Age Diffusion equation is based on isotropic scattering, however, the scattering of electrons at shallow depth is highly anisotropic in the forward direction and the small-angle scattering assumption is more appropriate. Roos et al (1973) have shown that for therapeutic energy electrons in low atomic number materials, the mean square angle of travel does not reach the diffusive value of 0.6 rad^2 within the CSDA range. If we also consider that because of bremsstrahlung production most therapeutic electrons will not reach their CSDA range before being absorbed, then it is clear that the description of electron penetration provided by the Age Diffusion equation is inappropriate.

However, in contrast to these arguments we have seen the application of solutions to the Age Diffusion equation to electron treatment planning having some degree of success. This apparent paradox is resolved when we examine the solution to the Age Diffusion equation for the spatial fluence from a point isotropic source. It is a Gaussian, exactly the same form as the solutions to the Fokker-Planck and Fermi equations for a pencil beam of electrons undergoing small-angle scattering. These small-angle scattering solutions are applicable over most of the electron range and the fact that the Age Diffusion solution is fortuitously also Gaussian for a point source accounts for the success of Age Diffusion theory to modelling broad beam electron

dose distributions in homogeneous media.

The Steban et al (1979) modification to the Kawachi (1975) solution of the Age Diffusion equation requires the optimization of six variables to obtain good agreement with experimental data. This optimization procedure must be repeated for each beam energy and therefore requires a large amount of electron dose distribution data before suitable values of the six variables can be determined. Even so, the optimized values are unable to accurately reproduce depth dose data in small fields for beams of low energy because of the large initial rise in the depth dose gradient for such beams. It was for just this reason that Steban et al (1979) and Millan et al (1979) added quadratic terms to the argument of the cosine in the original Kawachi solution. In fact, much better agreement with experimental data is achieved by replacing the cosine and exponential terms describing the central axis depth dose distribution with the analytic expression due to Strydom (1984).

The older methods used for inhomogeneity corrections, such as the AET, Absorption Coefficient, CET and MAC methods, require a very large set of measured data to give results that are accurate enough to be clinically acceptable. Even so, these methods are unable to predict the hot and cold spots near edges of an inhomogeneity where differential scattering effects between an inhomogeneity and water is considerable.

The dose shifting method of Pohlit and Manegold (1976) which attempts to account for scattering from the edges of inhomogeneities cannot deal with a complex patient geometry in which the shape and orientation of inhomogeneities is essentially arbitrary. The partial beam substitution method (Abou-Mandour and Harder 1978) is a little more successful in this respect, since the broad beam is split into partial beams and dose is corrected for differential scattering in the inhomogeneity compared to water. In the limit of small partial beams this approach is closely analogous to the pencil beam approach discussed in the next section but does not have the same potential because it lacks a theoretical basis.

All the above broad beam approaches to inhomogeneous media do not predict dose in the build-up region of therapeutic beams accurately. Brahme and Lax (1983) have shown that corrections to fluence and dose based on multiple scattering theory enable the dose in the build-up region to be scaled for inhomogeneous media. However, the approach is restricted to large beams incident upon idealized slab inhomogeneities greater in area than the beam width and which are of constant thickness lying parallel to the phantom surface.

Broad beam approaches to computing dose in inhomogeneous media are limited because they are based on isodose shifting techniques, which are strictly only applicable to beams incident upon slab in homogeneities of infinite lateral extent.

Corrections to the algorithms are required for many treatment variables such as patient surface contour, SSD, beam energy and penumbra regions. Measured data sets must be obtained for all of these treatment variables. This is a formidable task and therefore these approaches to dose computation have not been adopted widely.

The use of empirical pencil beam or slit beam (McKenzie 1979, Ekstrand and Dixon 1982) approaches to electron dose computation are limited to homogeneous media. Measurements must be performed for each beam energy and SSD, and the accuracy of reproduction of broad beam penumbra is dependent upon the initial width of the empirical pencil beam used to derive basic dose data. Furthermore, the basic dose data for a pencil beam is difficult to obtain accurately. Empirical pencil beams formed by collimation are simple to devise (Lillicrap et al 1975, Puel 1981, Abou-Mandour et al 1983, McParland and Cunningham 1986) but the high collimator produced bremsstrahlung to electron dose ratio at depths over the second half of the incident electron range is problematical. Brahme et al (1981) avoided this problem by producing a pencil beam from magnetic focussing of a microtron accelerator beam. However, this is not a simple process which could be implemented easily in a clinical setting, especially for types of linear accelerators other than the microtron.

Theoretical and analytical expressions for describing electron pencil beams in tissue offer the greatest potential for

accurately computing dose in both homogeneous and inhomogeneous tissue media with a minimum amount of experimental input data. The solution to the Fermi transport equation for a pencil beam boundary condition is currently the most popular theoretical research tool used to compute electron dose in tissue for broad therapeutic electron beams. However, the calculation of dose from broad beams using only Fermi multiple scattering theory is inadequate. For an infinitely broad field this theory predicts a constant dose with depth in the scattering medium. This is because Fermi theory considers only the transport of the incident primary electrons which are assumed to not lose energy, are not absorbed, and only undergo small-angle scattering interactions. These limitations require that central axis depth dose data for an infinitely large field (i.e. field length greater than the range) in tissue be used as normalization data. The incorporation of secondary interaction effects into the Fermi-Eyges formalism to avoid the use of empirical depth dose data is the aim of current research. Jette (1985) introduced a Second-Order theory to include the skewness of the primary electron path and thereby accounted for one component of the dose build-up in central axis depth dose curves. The contribution to dose of other interaction effects have been discussed by Jette et al (1985) but they did not provide any practical applications of their calculations for pencil beam approaches. Other modifications of Fermi-Eyges theory have been empirical such as those for

range straggling by Werner et al (1982) and Lax et al (1983).

Alternative methods to try to overcome the shortcomings associated with Fermi-Eyges theory have included the use of Monte Carlo results. The Generalized Gaussian approach developed by Brahme et al (1981) and Lax et al (1983) incorporates large angle scattered electrons by fitting the spatial profiles of Monte Carlo generated pencil beams to the sum of three Gaussians, rather than the single Gaussian predicted in the small angle scattering theory. Lax et al (1983) have shown that the Generalized Gaussian approach is superior to Fermi Eyges theory because it is able to more accurately predict the central axis dose distribution in very small fields from a large field central axis dose distribution. More recently Bruinvis (1987) has attempted to model range straggling effects and uses Monte Carlo data to fix free variables in this model. The use of Monte Carlo data in pencil beam dose computation methods is advantageous but limits these methods to dealing only with homogeneous media.

The approach of Bruinvis et al (1983) to the computation of dose in homogeneous media utilized two sets of values of pencil beam spread. One set for the central region of the beam for changes in central axis depth dose with field size and shape and the other set for predicting penumbra. Non-unique values of pencil beam spread is obviously inconsistent with the physical situation and this approach therefore lacks predictive power and is unlikely to yield good agreement with measured data for

arbitrary changes in SSD and surface contour.

The series of papers by Goitein (1978), Goitein et al (1978) and Goitein and Sisterson (1978) demonstrated how the Gaussian approximation of small angle scattering theory could be used to predict the characteristic hot and cold spot fluence perturbations observed beyond inhomogeneities. However, the practical implementation of the dose computation algorithm is limited since the inhomogeneities are considered infinitely thin with the same axial density as the true inhomogeneity. Corrections for the presence of inhomogeneities are simple using Fermi-Eyges theory if it is assumed that the inhomogeneity encountered by a particular pencil beam extends across its whole width (Abou-Mandour and Harder 1978, Hogstrom et al 1981, Werner et al 1982). This is termed the semi-infinite slab approximation by Lax (1986). Presently, the most advanced dose computation algorithm available for inhomogeneous media is due to Hogstrom et al (1981). This algorithm is based on Fermi-Eyges theory for a pencil beam and is notable for its completeness and integration with the anatomical and electron density information provided by X-ray computed tomography. However this algorithm makes approximations which can lead to substantial dose computation errors. The dose scaling procedure used is only approximate (Brahme and Lax 1983) and introduces systematic errors into the algorithm, in addition to the basic limitations of Fermi-Eyges theory, the semi-infinite

slab approximation and the two dimensional representation of patient anatomy. Hogstrom and Almond (1983) and Hogstrom et al (1984) conducted a dosimetric evaluation of their algorithm using a two-dimensional anthropomorphic head phantom. They showed that, in general, accuracies of $\pm 4\%$ in the treatment volume or ± 4 mm in regions of sharp dose gradients found in the penumbra and distal edge of the beam could be expected. In addition, there is the possibility of substantial dose errors behind heterogeneities long and parallel to the beam or deep beneath the skin surface. Further detailed evaluation of this algorithm by Cygler et al (1987) has shown that discrepancies between measured and computed data may be as large as 40% for three-dimensional inhomogeneities encountered clinically.

The Hogstrom et al (1981) pencil beam algorithm and the Lax and Brahme (1985) Generalized Gaussian algorithm are only two-dimensional and based on the semi-infinite slab approximation for the central ray of the pencil beams. The limitations due to the semi-infinite slab approximation have been theoretically analyzed by Brahme and Nilsson (1984) and Nilsson and Brahme (1986). They conclude that near the edge of an inhomogeneity and behind small inhomogeneities substantial dose errors may occur due to the linear angular scattering and stopping powers on each side of the interface being different. This error increases as the inhomogeneity thickness increases and the electrons near the end of their range. However, Lax (1986) states that the semi-infinite slab

approximation gives acceptable results over the first half of the electron range even for an inhomogeneity with very different stopping and scattering properties from water and discrepancies at depth are due to differences in the energy between those electrons that have passed through the inhomogeneity and those which have not.

The semi-infinite slab approximation can be avoided. One method is to use the mean path concept introduced by Perry and Holt (1980) and generalized to include energy loss by Jette (1984). However, the determination of all mean paths in each pencil beam for all the pencil beams comprising the broad beam is prohibitive in terms of computing time (Hogstrom 1985). A more attractive approach is to use the numerical algorithm of Storchi and Huizenga (1985). This iterative algorithm allows the linear scattering power of the medium to be a function of both depth and radial position in a pencil beam and redefines the pencil beam into a number of new pencil beams at each depth increment up to the electron range. A theoretical solution to the Fermi transport equation has also recently been obtained by Jette (1986a) for a pencil beam boundary condition in which the linear scattering power is a function of both depth and radial position. This work is still in its initial stages and it remains for future work to determine its importance for dose computations in patients. The approach is still obviously limited due to

assuming a sole interaction mechanism of small-angle multiple scattering.

The use of Fermi-Eyges scattering theory for the computation of electron dose in inhomogeneous tissue using pencil beams has recently received a great deal of attention. However, the approach is relatively new and requires development to overcome the inherent limitations of simple Fermi-Eyges theory. To logically tackle these problems, pencil beam descriptions of therapeutic electron beams in air and in homogeneous media should be fully developed and investigated.

3.5 Conclusions

Empirical broad beam approaches to electron dose computation are very limited since they have no predictive power for changes in treatment conditions and are suitable only for homogeneous media. Analytical solutions to the Boltzmann transport equation for broad beams are complex and also limited to "ideal" beams incident upon homogeneous media. This makes the approach unsuitable for routine treatment planning. A broad beam approach which has had some measure of success in homogeneous media is the solution to the age diffusion equation initially derived by Kawachi (1975). However, this approach requires the optimization of 6 variables which necessitates a large measured data set and has no predictive power for changes in SSD and beam energy or field shape. In addition, the age diffusion equation is derived from the Boltzmann transport equation on the assumption of

isotropic scattering. This assumption is inappropriate for the scattering of therapeutic high energy electrons. Therefore, the success this algorithm has achieved is fortuitously based on the point source solution being a Gaussian, exactly the same form as for small angle scattering transport equations.

Broad beam calculations of dose in inhomogeneous media are strictly only applicable to media with semi-infinite slab inhomogeneities. Extension of these algorithms to 2 and 3 dimensional inhomogeneities is artificial using ray projections from a virtual source. The methods developed require a formidably large measured data set to account for treatment set-up variables and thereby achieve clinically acceptable results. These methods have not been widely adopted.

Empirical pencil beam or slit beam approaches to electron dose computation may account for surface contour. However, because the approach is empirical, basic data must be derived at each beam energy and the approach is limited to homogeneous media. Analytical pencil beam approaches based on Fermi-Eyges theory offer the greatest potential for accurately computing electron dose in both homogeneous and inhomogeneous media. However, the analytical approach is relatively new, and theoretical models of accelerator beams have not yet been developed which can accurately describe the therapeutic beam in air, homogeneous tissue media, or inhomogeneous tissue media without the use of empirical input data. To achieve accurate patient dose com-

putation results ($< 5\%$ error) with a minimum amount of measured input data, theoretical modifications to the simple Fermi-Eyges theory are required in tissue media. These modifications should account for the interaction processes which are secondary to small-angle multiple scattering such as large-angle scattering, range straggling, delta-ray production and bremsstrahlung production.

Chapter 4

FERMI-EYGES THEORY AND
APPLICATIONS TO ELECTRON
RADIOTHERAPY

4.1 Introduction

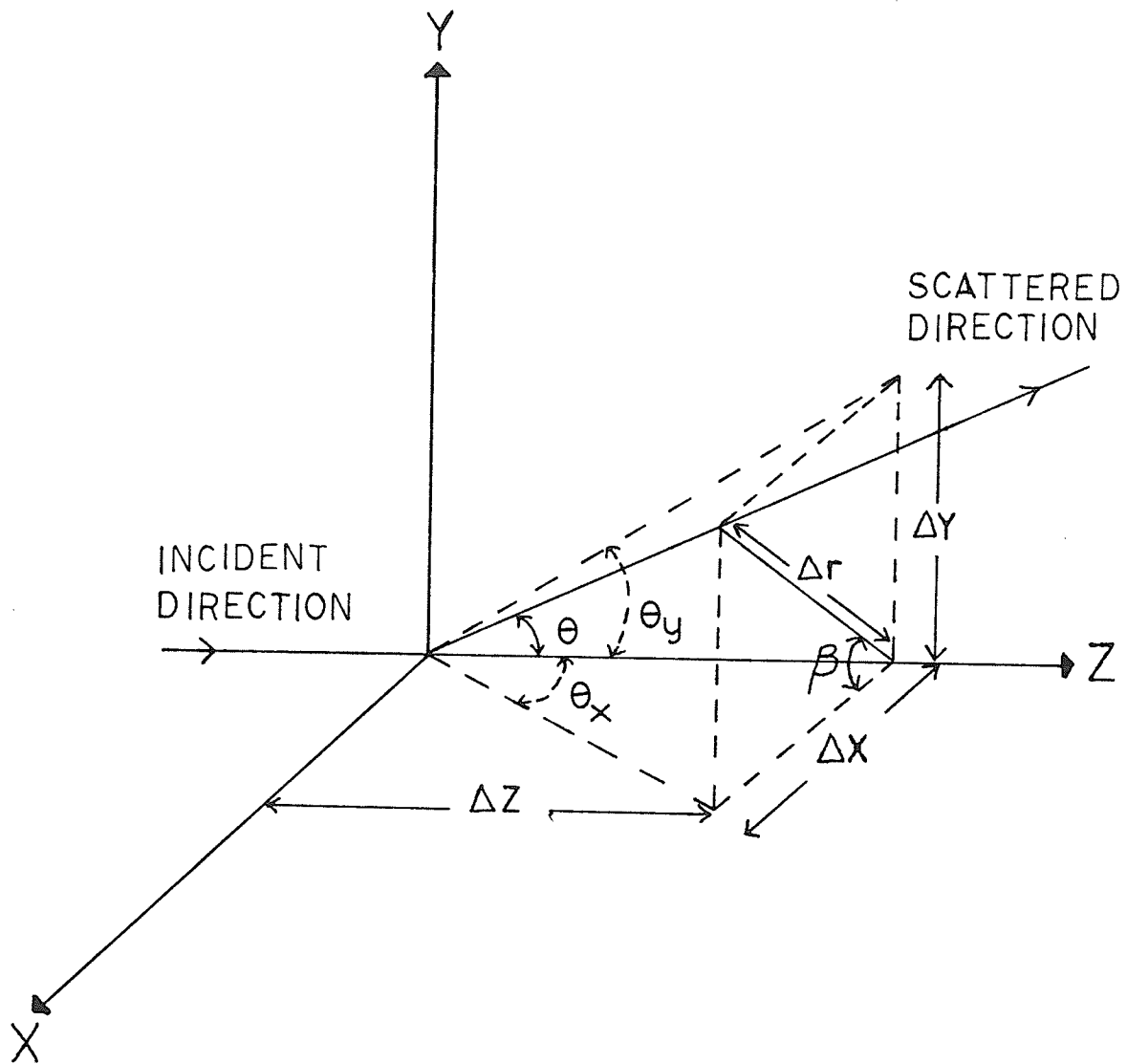
This chapter presents a detailed examination of the Fermi transport equation derivation, closely following Rossi and Griesen (1941). The solution of this transport equation for a point monodirectional pencil beam is also examined for a homogeneous medium. A mathematical analysis of the use of this solution for generating broad beam fluence and angular distributions is described for a broad parallel beam of electrons and a broad diverging beam of electrons produced by scanning a pencil beam over large angles. The distribution computed for the broad diverging beam are compared to those from a point isotropic source.

4.2 The Fermi Equation and Solutions

Rossi and Greisen (1941) cite Fermi as having originally derived the transport equation for electrons which undergo elastic small-angle multiple scattering in passing through a semi-infinite medium. Figure 4.1 shows the relationships between the polar angle θ and its projections θ_x and θ_y on to the (z,x) and (z,y) planes for an electron originally travelling parallel to the z axis. Since we have azimuthal symmetry and small-angle scattering, the relationships may be summarized as follows

$$\theta^2 = \theta_x^2 + \theta_y^2 = 2\theta_x^2 = 2\theta_y^2 \quad (4.1)$$

Figure 4.1: Trigonometrical relationships between the polar angle θ and its projections θ_x and θ_y on to the (z,x) and (z,y) planes for an electron originally travelling parallel to the z -axis



GEOMETRICAL RELATIONS

$$\text{TAN } \theta_x = \text{TAN } \theta \cdot \text{COS } \beta$$

$$\text{TAN } \theta_y = \text{TAN } \theta \cdot \text{SIN } \beta$$

for small angles

$$\theta_x = \theta \text{ COS } \beta$$

$$\theta_y = \theta \text{ SIN } \beta$$

or similarly upon averaging over azimuthal angles

$$\overline{\theta^2} = \overline{\theta_x^2} + \overline{\theta_y^2} = 2\overline{\theta_x^2} = 2\overline{\theta_y^2} \quad (4.2)$$

In the following derivations, outlined by Rossi and Greisen (1941), a probability $P_{\Delta Z}(\theta_x)d\theta_x$ is defined which is, the probability that an electron traversing the thickness ΔZ of a scattering medium will be deflected through a projected polar angle $(\theta_x, d\theta_x)$ regardless of the detailed multiple scattering processes within ΔZ . In fact, Rossi and Griesen (1941) did not use an explicit expression for $P_{\Delta Z}(\theta_x)$ but assumed it was symmetrical in θ_x and defined it by its first three moments.

$$P_{\Delta Z}(\theta_x) = P_{\Delta Z}(-\theta_x) \quad (4.3)$$

$$\int_{-\infty}^{+\infty} P_{\Delta Z}(\theta_x)d\theta_x = 1 \quad (4.4)$$

$$\int_{-\infty}^{+\infty} \theta_x P_{\Delta Z}(\theta_x)d\theta_x = 0 \quad (4.5)$$

$$\int_{-\infty}^{+\infty} \theta_x^2 P_{\Delta Z}(\theta_x)d\theta_x = \frac{k \cdot \Delta Z}{2} \quad (4.6)$$

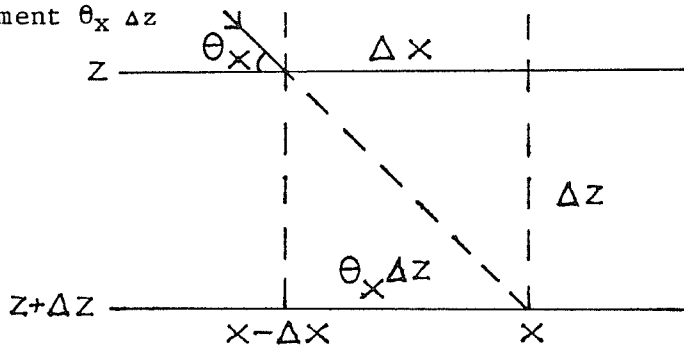
where k is the linear angular scattering power ($\text{radian}^2\text{cm}^{-1}$) of the medium and $P_{\Delta Z}(\theta_x)$ has been assumed so sharply peaked about $\theta_x=0$ that limits of integration have been redefined from 0 to and extended to $-\infty$ to $+\infty$.

The probability $F(x,y,z,\theta) dx dy d\theta$ of finding an electron at

depth z and lateral coordinates (x,y) , travelling with polar angle $(\theta d\theta)$ to the z axis, is symmetric in both the (x,z) and (y,z) planes, for a monidirectional point source of electrons incident normally upon the scattering medium at the origin of the coordinate system. This cylindrical symmetry of the problem allows the analysis of the scattering to proceed in either the (x,z) or (y,z) plane since

$$F(z,x,y,\theta) dx dy d\theta = F(z,x,\theta_x) dx d\theta_x F(z,y,\theta_y) dy d\theta_y \quad (4.7)$$

The function $F(z,x,\theta_x)$ changes in going from z to $z + \Delta z$ because both the position distribution and the angular distribution are modified by traversal of the layer Δz . Neglecting any scattering in the layer Δz , the position distribution is modified because electrons travelling at an angle θ_x undergo a lateral displacement $\theta_x \Delta z$

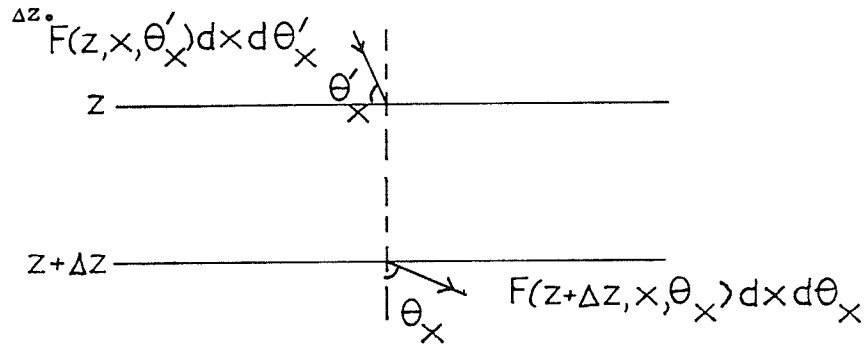


in traversing Δz . Therefore, particles having a lateral displacement x at $z + \Delta z$ are those which had a lateral displacement $x - \theta_x \Delta z$ at z . Hence neglecting the change in the angular

distribution

$$\begin{aligned}
 F(z+\Delta z, x, \theta_x) &= F(z, x - \theta_x, z, \theta_x) \\
 &= F(z, x, \theta_x) - \theta_x \cdot \Delta z \frac{\partial F}{\partial x} \quad (4.8)
 \end{aligned}$$

Now, neglecting any change in the position in the layer Δz , there are $F(z, x, \theta_x') dx d\theta_x'$ electrons in $(\theta_x', d\theta_x')$ at z and lateral position x . A fraction $P_{\Delta z}(\theta_x - \theta_x') d\theta_x$ of these electrons is scattered into the angular interval $(\theta_x, d\theta_x)$ in traversing Δz .



$$F(z+\Delta z, x, \theta_x) = \int_{-\infty}^{+\infty} F(z, x, \theta_x') P_{\Delta z}(\theta_x - \theta_x') d\theta_x' \quad (4.9)$$

The function $F(z, x, \theta_x')$ may be expanded in a Taylor series about $(\theta_x - \theta_x')$, since $P_{\Delta z}(\theta_x - \theta_x')$ is sharply peaked about θ_x' and we obtain

$$F(z+\Delta z, x, \theta_x) = F(z, x, \theta_x) + \frac{1}{2} \cdot \overline{\theta_x^2} \cdot \frac{\partial^2 F}{\partial \theta_x^2} \Delta z \quad (4.10)$$

Hence the total change in the distribution function $F(z, x, \theta_x)$ in

traversing Δz is obtained from equations (4.8) and (4.10) to be

$$\frac{\partial F(z,x,\theta_x)}{\partial z} = -\theta_x \frac{\partial F}{\partial x} + \frac{k}{4} \frac{\partial^2 F}{\partial \theta_x^2} \quad (4.11)$$

where $\overline{\theta_x^2}$ has been replaced by $k/2$. Including the independent component of scattering in the (y,z) plane, this equation becomes

$$\frac{\partial F(z,x,y,\theta_x,\theta_y)}{\partial z} = -\theta_x \frac{\partial F}{\partial x} - \theta_y \frac{\partial F}{\partial y} + \frac{k}{4} \left[\frac{\partial^2 F}{\partial \theta_x^2} + \frac{\partial^2 F}{\partial \theta_y^2} \right] \quad (4.12)$$

The solution for a point monidirectional source incident normally at the origin was found by Fermi to be

$$F(z,x,y,\theta_x,\theta_y) = F(z,x,\theta_x) \cdot F(z,y,\theta_y) \quad (4.13)$$

$$F(z,x,\theta_x) = \frac{1}{[2\pi(A_0 A_2 - A_1^2)]^{1/2}} \text{EXP} \left[\frac{-(A_0 x^2 - 2A_1 x \theta_x + A_2 \theta_x^2)}{2(A_0 A_2 - A_1^2)} \right]$$

where

$$A_i = \frac{1}{2} \int_0^z k(z-\epsilon)^i d\epsilon \quad \text{and } i=0,1,2$$

The linear angular scattering power k is considered a constant in the original derivation because energy loss of the electrons was neglected. Energy loss has been incorporated to a limited extent by Eyges (1948) who considered k a known function of the depth z in the scattering medium $k(z)$. As stated earlier, the boundary condition on the solution derived by Fermi (Equation 4.13) is that at $z=0$, $F(0,x,\theta_x) = \delta(x) \cdot \delta(\theta_x)$. The transport

equation may also be solved analytically for a number of other simple boundary conditions including the point isotropic source (Jette and Pagnamenta 1982, Jette et al 1983) and the point source with an initial Gaussian distribution of angles. Table 4.1 summarizes these solutions to the Fermi equation.

Several observations regarding the solution given in Equation (4.13) are noteworthy. The exponent of the equation may be rewritten as

$$\left[-\frac{x^2}{2A_2} \right] - \frac{[\theta_x - (A_1/A_2)x]^2}{2[A_0 - (A_1^2/A_2)]} \quad (4.14)$$

This means that for a point at depth z and lateral position x in the pencil beam, the projected angular distribution of the electrons passing through the point is Gaussian with variance $\overline{\theta_x^2}(z,x)$

$$\overline{\theta_x^2}(z,x) = A_0 - (A_1^2/A_2) \quad (4.15)$$

or

$$\overline{\theta_x^2}(z,x) = \frac{kz}{8} \quad \text{for } k = \text{constant} \quad (4.16)$$

This projected Gaussian-angular distribution is inclined to the z -axis about a projected mean angle of travel $\overline{\theta_x}(z,x)$

$$\overline{\theta_x}(z,x) = \frac{A_1 \cdot x}{A_2} \quad (4.17)$$

or

$$\overline{\theta_x}(z,x) = \frac{3}{2} \cdot \frac{x}{z} \quad \text{for } k = \text{constant} \quad (4.18)$$

Table 4.1

Solutions to the Fermi Equation in the z-x plane

Type of Point Source	Boundary condition at z=0, x=0	Solution *
Monodirectional Normal	$\delta(x) \cdot \delta(\theta_x)$	$\frac{1}{\sqrt{2\pi D}} \text{EXP} - \frac{(A_0 x^2 - 2A_1 x \theta_x + A_2 \theta_x^2)}{2D}$
Isotropic	$\delta(x)$	$\frac{1}{\sqrt{2\pi C}} \text{EXP} - \frac{(\theta_x - x/z)^2}{2C}$
Initial Gaussian angular distribution	$\delta(x) \text{EXP} \left[-\frac{(\theta_x - \theta_0)^2}{2\theta_x^2} \right]$	$\frac{1}{\sqrt{2\pi B}} \text{EXP} - \left[\frac{A_0 (x - \theta_0 z)^2 - 2A_1 x \theta_0 + A_2 \theta_0^2}{2B} \right]$

* where $B = A_0 A_2 - A_1^2$ and $A_1 = \overline{\theta_x^2} (\omega z^2 + A_1)$
 $C = A_0 - 2A_1/z + A_2/z^2$
 $D = A_0 A_2 - A_1^2$

Integration of the function $F(z, x, \theta_x)$ over all angles θ_x gives the spatial probability distribution $F(z, x)$ irrespective of the angle of travel (for small angle scattering the integration limits may be extended to $\pm\infty$)

$$F(z, x) = \int_{-\infty}^{+\infty} F(z, x, \theta_x) d\theta_x \quad (4.19)$$

$$F(z, x) = \frac{1}{\sqrt{2\pi A_2}} \cdot \text{EXP} \left[-\frac{x^2}{2A_2} \right] \quad (4.20)$$

Therefore, the solution predicts that the point source of electrons which is initially monodirectional along the z-axis spreads out laterally to form a Gaussian spatial distribution. The variance $\sigma^2(z)$ of this spatial Gaussian increases with depth

$$\sigma^2(z) = A_2 \quad (4.21)$$

or

$$\sigma^2(z) = \frac{kz^3}{6} \quad \text{for } k = \text{constant} \quad (4.22)$$

Similarly, integration of the function $F(z, x, \theta_x)$ over all lateral positions x gives the angular probability distribution $F(z, \theta_x)$ irrespective of lateral position.

$$F(z, \theta_x) = \int_{-\infty}^{+\infty} F(z, x, \theta_x) dx \quad (4.23)$$

$$F(z, \theta_x) = \frac{1}{\sqrt{2\pi A_0}} \cdot \text{EXP} \left[-\frac{\theta_x^2}{2A_0} \right] \quad (4.24)$$

Thus, not only does the solution predict that the projected angular distribution of the electrons passing through each point (z, x) is Gaussian (Equation 4.14), it also predicts that all the electrons at a given depth z have a Gaussian projected angular distribution with variance $\overline{\theta_x^2}(z)$

$$\overline{\theta_x^2}(z) = A_0 \quad (4.25)$$

or

$$\overline{\theta_x^2}(z) = \frac{kz}{2} \quad \text{for } k = \text{constant} \quad (4.26)$$

Finally, integration of Equation (4.24) over all angles θ_x or equivalently integration of Equation (4.20) over all lateral positions x gives

$$F(z) = \int_{-\infty}^{+\infty} F(z, \theta_x) d\theta_x = \int_{-\infty}^{+\infty} F(z, x) dx = 1 \quad (4.27)$$

This indicates that the Fermi Transport equation only describes the small-angle multiple scattering process. The incident electrons are not absorbed with depth in the scattering medium and other processes which create additional electron fluence,

such as delta-rays or bremsstrahlung produced electrons, are neglected.

4.3 Applications in Electron Radiotherapy

To accurately determine the absorbed dose distribution in a patient from a broad electron beam incident at the surface, the electron fluence at a given location must be computed.

Therefore, interest may be focussed on the spatial probability distribution $F(z,x,y)$ given by the product of Equation (4.20) with its equivalent in the y -direction

$$F(z,x,y) = \frac{1}{2\pi A_2} \text{EXP} \left[\frac{-(x^2 + y^2)}{2A_2} \right] \quad (4.28)$$

Isoprobability curves may be defined (Jette et al 1983) as the locus of points for which $F(z,x,y)$ is a constant. The cylindrical symmetry of the problem allows us to choose the (z,x) plane without loss of generality, and the locus of points is specified by

$$x = \pm \left(-2A_2 \ln [2\pi A_2 F(z,x,0)] \right)^{1/2} \quad (4.29)$$

4.3.1 Parallel Rectangular Broad Beams

The fluence from a broad parallel rectangular electron field may be described by summation of the pencil beam solution over the broad beam area. This summation is

a simple convolution integral if the electrons are incident normally to the scattering medium with unit planar fluence within the broad beam area and zero outside.

Defining the broad beam rectangular area by $-a < x < a$ and $-b < y < b$, we continue to work in two-dimensions with trivial extension to the third dimension.

$$\begin{aligned} \tilde{F}(z, x, \theta_x) &= \int_{-a}^{+a} F(z, x-x', \theta_x) dx' \\ &= \frac{1}{2} \frac{\text{EXP}(-\theta_x^2 / 2A_0)}{\sqrt{2\pi A_0}} \\ &\quad \cdot \left[\text{ERF} \frac{a + [x - (A_1/A_0)\theta_x]}{[2(A_2 - (A_1^2/A_0))]^{1/2}} \right. \\ &\quad \left. + \text{ERF} \frac{a - [x - (A_1/A_0)\theta_x]}{[2(A_2 - (A_1^2/A_0))]^{1/2}} \right] \quad (4.30) \end{aligned}$$

In the limit $|a| \rightarrow \infty$, $\text{ERF}(\infty) = 1$ and the angular distribution of the electrons at any point (z, x) in the broad beam is Gaussian. Comparison of Equation (4.30) with Equation (4.24) reveals that, in the limit, compensation by adjacent pencil beams is such that the angular distribution at a point (z, x) in the broad beam is identical to the pencil beam angular probability distribution, irrespective of lateral position. Strictly, for $|a| < \infty$ the angular distribution at a point (z, x) in the broad beam given by Equation (4.30) is not Gaussian. However,

Storchi and Huizenga (1985) have shown that to a fairly good approximation the angular distribution in θ_x at (z,x) may be considered a Gaussian function with mean and mean square deviation given by the first three moments of $\tilde{F}(z,x,\theta_x)$ with respect to θ_x .

$$\langle \theta_x \rangle (z,x) = \tilde{F}_1(z,x) / \tilde{F}_0(z,x) \quad (4.31)$$

$$\langle \theta_x^2 \rangle (z,x) = \tilde{F}_2(z,x) / \tilde{F}_0(z,x) - [\langle \theta_x \rangle]^2 \quad (4.32)$$

$$\text{where } \tilde{F}_i(z,x) = \int_{-\infty}^{+\infty} \theta_x^i \tilde{F}(z,x,\theta_x) d\theta_x ; i=0,1,2 \quad (4.33)$$

Specifically these moments are,

$$\tilde{F}_0(z,x) = \frac{1}{2} \left[\frac{\text{ERF}(x+a)}{\sqrt{2A_2}} - \frac{\text{ERF}(x-a)}{\sqrt{2A_2}} \right] \quad (4.34)$$

$$\tilde{F}_1(z,x) = \frac{A_1}{\sqrt{2\pi A_2}} \left[\frac{\text{EXP} \frac{-(x-a)^2}{2A_2}}{2A_2} - \frac{\text{EXP} \frac{-(x+a)^2}{2A_2}}{2A_2} \right] \quad (4.35)$$

$$\begin{aligned} \tilde{F}_2(z,x) = \frac{1}{2} A_0 \left[\frac{\text{ERF} \frac{(x+a)}{\sqrt{2A_2}}}{\sqrt{2A_2}} - \frac{\text{ERF} \frac{(x-a)}{\sqrt{2A_2}}}{\sqrt{2A_2}} \right] \\ - \frac{2A_1^2}{A_2} \left[\frac{(x+a) \cdot \text{EXP} - \frac{(x+a)^2}{2A_2}}{\sqrt{2\pi A_2}} \right. \\ \left. - \frac{(x-a) \cdot \text{EXP} - \frac{(x-a)^2}{2A_2}}{\sqrt{2\pi A_2}} \right] \quad (4.36) \end{aligned}$$

The first moment $\tilde{F}_0(z,x)$ defines the spatial fluence probability distribution for the parallel broad beam, which in three dimension is given by

$$\begin{aligned} \tilde{F}(z,x,y) &= \tilde{F}_0(z,x) \cdot \tilde{F}_0(z,y) \\ &= \frac{1}{4} \left[\frac{\text{ERF} \frac{(x+a)}{\sqrt{2A_2}}}{\sqrt{2A_2}} - \frac{\text{ERF} \frac{(x-a)}{\sqrt{2A_2}}}{\sqrt{2A_2}} \right] \\ &\quad \left[\frac{\text{ERF} \frac{(y+b)}{\sqrt{2A_2}}}{\sqrt{2A_2}} - \frac{\text{ERF} \frac{(y-b)}{\sqrt{2A_2}}}{\sqrt{2A_2}} \right] \quad (4.37) \end{aligned}$$

The central axis fluence distribution is found by setting $x=y=0$ in Equation (4.37) to obtain

$$\tilde{F}(z,0,0) = \frac{\text{ERF} \frac{a}{\sqrt{2A_2}}}{\sqrt{2A_2}} \cdot \frac{\text{ERF} \frac{b}{\sqrt{2A_2}}}{\sqrt{2A_2}} \quad (4.38)$$

The central axis distribution predicted is initially flat for intermediate sized square fields since $a \gg (2A_2)^{1/2}$ and therefore $F(z,0,0)=1$. Equation 4.38 does not predict any of the dose build-up seen in clinical beams. A descending fluence gradient is due only to lateral scatter disequilibrium when $a < (2A_2)^{1/2}$.

4.3.2 Diverging Rectangular Broad Beams

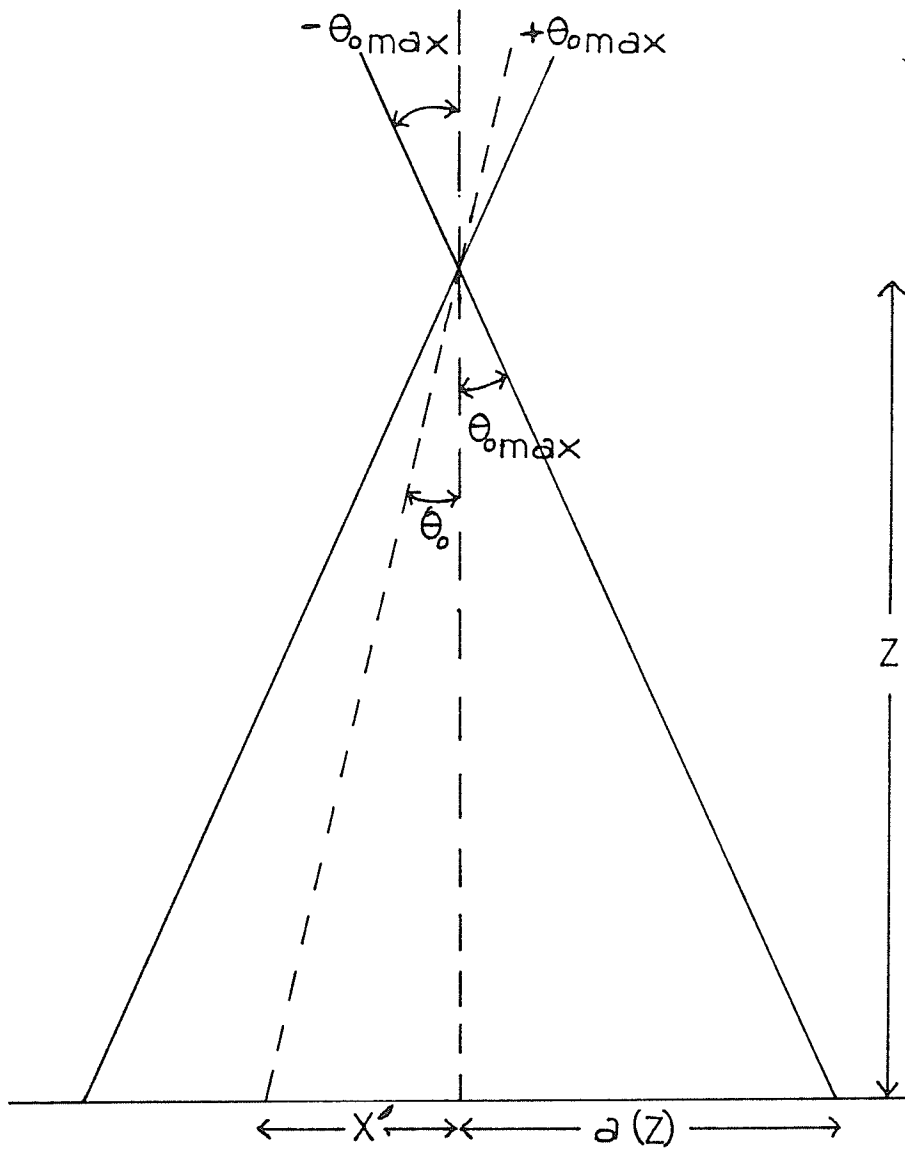
The fluence from a broad diverging rectangular electron field may be described by scanning a pencil beam over the broad beam area. The geometry is shown in Figure 4.2, again we proceed with the analysis in two dimensions with trivial extension to the third dimension y . The broad beam rectangular area is defined by $-a < x < a$ and $-b < y < b$ where $|a|$ and $|b|$ are now functions of the depth z in the scattering medium due to geometric divergence. The angles through which the pencil beam is scanned is related to the depth and instantaneous lateral position x' of the central axis of the pencil beam by,

$$\theta_0 \approx \tan \theta_0 = \frac{x'}{z} \quad (4.39)$$

and the maximum angle $\theta_{0\max}$ through which the beam is scanned is given by

$$\theta_{0\max} \approx \tan \theta_{0\max} = \frac{a}{z} \quad (4.40)$$

Figure 4.2: Geometry for a pencil beam scanned over a wide angle
 0_0 between the limits $-\theta_{\text{omax}} < \theta_0 < +\theta_{\text{omax}}$.



For a monodirectional pencil beam inclined at an angle θ_0 to the surface of the scattering medium the boundary condition on the Fermi transport equation is $F(0, x, \theta_x) = \delta(x) \cdot \delta(\theta_x - \theta_0)$. The solution is simply obtained from Fermi's original solution by rotation of the coordinate axis under the small angle assumption such that $z' = z$, $x' = x - \theta_0 z$, $y' = y - \theta_0 z$, $\theta_x' = \theta_x - \theta_0$ and substitution into Equation (4.13) gives

$$F(z, x, \theta_x, \theta_0) = \frac{1}{\sqrt{2\pi(A_0 A_2 - A_1^2)}} \cdot \text{EXP} \left[\frac{-A_0(x - \theta_0 z)^2 - 2A_1(x - \theta_0 z)(\theta_x - \theta_0) + A_2(\theta_x - \theta_0)^2}{2(A_0 A_2 - A_1^2)} \right] \quad (4.41)$$

In an analysis which is completely analogous to that for the parallel broad beam given in section 4.3.1, we may compute the angular distribution at a point (z, x) in the diverging broad beam by integrating over all θ_0 (Appendix 4.1).

$$\begin{aligned} \tilde{F}(z, x, \theta_x) &= \int_{-\theta_0 \max}^{+\theta_0 \max} F(z, x, \theta_x, \theta_0) d\theta_0 \\ &= \frac{1}{z} \int_{-a}^{+a} F(z, x, \theta_x, x') dx' \end{aligned}$$

$$\begin{aligned}
\tilde{F}(z,x,\theta_x) &= \frac{-100-}{z\sqrt{2\pi(A_0-2A_1/z+A_2/z^2)}} \frac{1}{2(A_0-2A_1/z+A_2/z^2)} \text{EXP} \frac{-(\theta_x - x/z)^2}{2(A_0-2A_1/z+A_2/z^2)} \\
&\quad \frac{1}{2} \left\{ \text{ERF} \left[a + \frac{x(A_1-A_0/z) - \theta_x(A_2-A_1/z)}{z(A_0-2A_1/z+A_2/z^2)} \right] \sqrt{\frac{2(A_0A_2-A_1^2)}{(A_0-2A_1/z+A_2/z^2)}} \right. \\
&\quad \left. + \text{ERF} \left[a - \frac{x(A_1-A_0/z) - \theta_x(A_2-A_1/z)}{z(A_0-2A_1/z+A_2/z^2)} \right] \sqrt{\frac{2(A_0A_2-A_1^2)}{(A_0-2A_1/z+A_2/z^2)}} \right\}^{1/2} \quad (4.43)
\end{aligned}$$

In the limit $|a| \rightarrow \infty$, $\text{ERF}(\infty) = 1$ and the angular distribution of the electrons at any point (z,x) in the diverging broad beam is a Gaussian about a mean angle $\langle \theta_x \rangle(z,x) = x/z$. In fact, in this limit, the angular distribution at a point (z,x) in the broad beam is identical to the angular probability distribution for an isotropic source (Table 4.1). Strictly, for $|a| < \infty$ the angular distribution at a point (z,x) in the diverging broad beam is not Gaussian. However, in analogy with the parallel beam case, it may be assumed that the angular distribution in θ_x at (z,x) for the diverging broad beam is Gaussian to a good approximation. The mean and mean square deviation of the angular distribution at (z,x) is given by the first three moments of $F(z,x,\theta_x)$ with respect to θ_x (Equations 4.31, 4.32 and 4.33).

These moments have been derived by Huizenga and

Storchi (1986) for a pencil beam with an initial Gaussian distribution of angles. The form of their equations is identical to the results derived in Appendix 4.2 for the present case of a monodirectional pencil beam initially inclined at an angle to the scattering medium and then scanned over a finite angle. The first three moments are

$$\tilde{F}_0(z,x) = \frac{1}{z} \cdot \frac{1}{2} \left[\text{ERF} \frac{(x+a)}{\sqrt{2A_2}} - \text{ERF} \frac{(x-a)}{\sqrt{2A_2}} \right] \quad (4.44)$$

$$\tilde{F}_1(z,x) = \frac{x \tilde{F}_0}{z} + \frac{1}{z} \frac{[A_1 - (A_2/z)]}{\sqrt{2\pi A_2}} \cdot \left[\text{EXP} - \frac{(x-a)^2}{2A_2} - \text{EXP} - \frac{(x+a)^2}{2A_2} \right] \quad (4.45)$$

$$\tilde{F}_2(z,x) = \left[A_0 - 2A_1/z + A_2/z^2 - x^2/z^2 \right] \tilde{F}_0 + 2\tilde{F}_1 \cdot x/z \quad (4.46)$$

$$+ \frac{(A_1 - A_2/z)^2}{A_2 z} \left[\frac{(x-a) \cdot \text{EXP} - (x-a)^2}{\sqrt{2\pi A_2}} - \frac{(x+a) \cdot \text{EXP} - (x+a)^2}{2A_2} \frac{1}{\sqrt{2\pi A_2}} \frac{1}{2A_2} \right]$$

The first moment $F_0(z,x)$ defines the spatial fluence probability distribution for the diverging broad beam, which in three dimensions is given by

$$\tilde{F}(z,x,y) = \tilde{F}_0(z,x) \cdot \tilde{F}_0(z,y)$$

$$\tilde{F}(z,x,y) = \frac{1.1}{z^4} \left[\frac{\text{ERF} \left(\frac{x+a}{\sqrt{2A_2}} \right) - \text{ERF} \left(\frac{x-a}{\sqrt{2A_2}} \right)}{\sqrt{2A_2}} \right] \cdot \left[\frac{\text{ERF} \left(\frac{y+b}{\sqrt{2A_2}} \right) - \text{ERF} \left(\frac{y-b}{\sqrt{2A_2}} \right)}{\sqrt{2A_2}} \right] \quad (4.47)$$

Comparison with the parallel broad beam case

(Equation 4.37) reveals that the divergent beam includes an inverse square law term ($1/z^2$) and, of course, the field dimensions a and b are depth dependent. It is interesting to note the value of $\langle \theta_x^2 \rangle (z,x)$ in the central region of the large diverging beam i.e. for $(2A_2)^{1/2} \ll a$ and $x \ll a$.

$$\langle \theta_x^2 \rangle (z,x) = \tilde{F}_2 / \tilde{F}_0 - \left[\tilde{F}_1 / \tilde{F}_0 \right]^2 \quad (4.48)$$

$$\langle \theta_x^2 \rangle (z,x) = A_0 - 2A_1/z + A_2/z^2 \quad (4.49)$$

or

$$\langle \theta_x^2 \rangle (z,x) = \frac{kz}{6} \quad \text{for } k = \text{constant} \quad (4.50)$$

This is just the value for an isotropic point source. We may therefore consider the scanned pencil beam source as an isotropic source if we are concerned only with the central region of a broad beam. The value of $\langle \theta_x^2 \rangle (z,x)$

decreases in the penumbra region of the beam (i.e. when $x \approx a$) and the value in a large field at $x=a$ is

$$\langle \theta_x^2 \rangle = \frac{(A_0 - 2A_1/z + A_2/z^2) - 2[A_1 - (A_2/z)]^2}{\pi A_2} \quad (4.51)$$

$$\text{or } \langle \theta_x^2 \rangle = \frac{kz}{6} \left[1 - \frac{1}{2\pi} \right] \quad \text{for } k = \text{constant} \quad (4.52)$$

where σ^2 is the spatial variance of a pencil beam and equals A_2 . However, if the angle over which the beam is scanned is small, the value of $\langle \theta_x^2 \rangle (z,x)$ in the central region of the field produced falls below the isotropic value given by Equation (4.49).

4.4 Conclusions

The small angle multiple scattering theory of Fermi-Eyges is particularly simple. The source electrons are considered to have an infinite range and other interaction processes which produce additional electrons in the scattering medium are ignored. This theory adequately describes the scattering of therapeutic energy electrons in air over distances of the order of metres. Broad parallel therapeutic electron beams may be described by the summation of monodirectional pencil beams over the broad beam area. Broad diverging therapeutic electron beams may be described by a monodirectional pencil beam scanned over a large angle. The fluence distribution derived for a broad parallel beam is similar

to a broad diverging beam, except that there is an additional inverse square law term and the field size increases with depth in the scattering medium for the diverging beam. The geometry most often encountered in external beam therapy is the diverging beam. For diverging electron beams produced by scanning, the angular distribution in the central region of the beam (where the fluence is constant) is identical to that produced by an isotropic point source. It is possible therefore to describe the therapeutic broad beams produced by an electron accelerator which uses magnetic quadrupole scanning, in terms of a collimated isotropic source.

Appendix 4.1

Derivation of distribution function for a broad beam produced by scanning a pencil beam.

The distribution function $\tilde{F}(z, x, \theta_x, \theta_0)$ for a monodirectional electron pencil beam incident at the origin of coordinates at an angle θ_0 to the z-axis is given by Equation 4.42 as

$$\tilde{F}(z, x, \theta_x, \theta_0) = \frac{1}{\sqrt{2\pi(A_0 A_2 - A_1^2)}} \cdot \text{EXP} \left[-\frac{(\theta_x - \theta_0)^2 A_2 - 2(\theta_x - \theta_0)(x - \theta_0 z) A_1 + (x - \theta_0 z)^2 A_0}{2(A_0 A_2 - A_1^2)} \right] \quad (\text{A4.1})$$

The distribution function for the broad diverging beam produced by scanning this pencil beam over a large angle such that θ_0 varies, $-\theta_{0\text{max}} < \theta_0 < +\theta_{0\text{max}}$ is given by

$$\tilde{F}(z, x, \theta_x) = \int_{-\theta_{0\text{max}}}^{+\theta_{0\text{max}}} \tilde{F}(z, x, \theta_x, \theta_0) d\theta_0 \quad (\text{A4.2})$$

This equation may be expressed as

$$\tilde{F}(z, x, \theta_x) = \frac{1}{\sqrt{2\pi}e} \int_{-\theta_{0\text{max}}}^{+\theta_{0\text{max}}} \text{EXP} \left[-\frac{(b\theta_0^2 + c\theta_0 + d)}{2e^2} \right] d\theta_0 \quad (\text{A4.3})$$

where

$$\begin{aligned}
 b &= A_2 - 2A_1z + A_0z^2 > 0 \\
 c &= -2A_2\theta_x + 2A_1\theta_x z + 2A_1x - 2A_0xz \\
 d &= A_2\theta_x^2 - 2A_1\theta_x x + A_0x^2 \\
 e^2 &= A_0A_2 - A_1^2 > 0
 \end{aligned}$$

and the integral may be split

$$\begin{aligned}
 \tilde{F}(z, x, \theta_x) &= \frac{1}{\sqrt{2\pi}e} \cdot \text{EXP}\left[-\frac{d}{2e^2}\right] \cdot \left\{ \int_{-\theta_{\max}}^0 \text{EXP}\left[-\frac{b}{2e^2}\theta_0^2 - \frac{c}{2e^2}\theta_0\right] d\theta_0 \right. \\
 &\quad \left. + \int_0^{+\theta_{\max}} \text{EXP}\left[-\frac{b}{2e^2}\theta_0^2 - \frac{c}{2e^2}\theta_0\right] d\theta_0 \right\} \quad (\text{A4.4})
 \end{aligned}$$

Making the substitutions

$$\frac{b}{2e^2} = \frac{1}{4\beta} \quad \text{and} \quad \frac{c}{2e^2} = \gamma \quad (\text{A4.5})$$

allows the use of the standard integrals

$$\int_0^{\infty} \text{EXP}\left[-\frac{1}{4\beta}\theta_0^2 - \gamma\theta_0\right] d\theta_0 = \sqrt{\pi\beta} \text{EXP}(\beta\gamma^2) \cdot [1 - \text{ERF}(\gamma\sqrt{\beta})] \quad (\text{A4.6})$$

and

$$\int_{\theta_{\max}}^{\infty} \text{EXP}\left[-\frac{1}{4\beta}\theta_0^2 - \gamma\theta_0\right] d\theta_0 = \sqrt{\pi\beta} \text{EXP}(\beta\gamma^2) \cdot [1 - \text{ERF}(\gamma\sqrt{\beta} + \theta_{\max}/2\sqrt{\beta})] \quad (\text{A4.7})$$

and we obtain, using the identities $\theta_{\max} = a/z$, $\gamma = c/2e^2$ and $\beta = 2e^2/4b$

$$\tilde{F}(z, x, \theta_x) = \frac{1}{2\sqrt{\beta}} \cdot \text{EXP} \left[-\frac{(4bd - c^2)}{8be^2} \right] \cdot \left[\text{ERF} \left(\frac{a + 2\gamma\beta z}{2z\sqrt{\beta}} \right) + \text{ERF} \left(\frac{a - 2\gamma\beta z}{2z\sqrt{\beta}} \right) \right] \quad (\text{A4.8})$$

Substituting for the values of b, c, d and e^2 given in Equation A4.3 we find

$$\frac{4bd - c^2}{8be^2} = \frac{(\theta_x - x/z)^2}{2(A_0 - 2A_1/z + A_2/z^2)} \quad (\text{A4.9})$$

$$2\gamma\beta z = \left[\frac{x(A_1 - A_0 z) - \theta_x(A_2 - A_1 z)}{z(A_0 - 2A_1/z + A_2/z^2)} \right] \quad (\text{A4.10})$$

$$2z\sqrt{\beta} = \left[\frac{2(A_0 A_2 - A_1^2)}{(A_0 - 2A_1/z + A_2/z^2)} \right]^{1/2} \quad (\text{A4.11})$$

Appendix 4.2

Derivation of moments for the angular electron distribution in a
broad diverging beam

The distribution function $F(z, x, \theta_x, \theta_0)$ for a monodirectional electron pencil beam incident at the origin of coordinates at an angle θ_0 to the z - axis is given by Equation 4.42 as

$$F(z, x, \theta_x, \theta_0) = \frac{1}{\sqrt{2\pi(A_0 A_2 - A_1^2)}} \cdot \text{EXP} \left[-\frac{(\theta_x - \theta_0)^2 A_2 - 2(\theta_x - \theta_0)(x - \theta_0 z) A_1 + (x - \theta_0 z)^2 A_0}{2(A_0 A_2 - A_1^2)} \right] \quad (\text{B4.1})$$

It is convenient to rearrange this into the form

$$F(z, x, \theta_x, \theta_0) = \frac{1}{\sqrt{2\pi A_2}} \text{EXP} \left[-\frac{(x - \theta_0 z)^2}{2A_2} \right] \cdot \frac{1}{\sqrt{2\pi(A_0 - A_1^2/A_2)}} \text{EXP} \left[-\frac{\{(\theta_x - \theta_0) - (x - \theta_0 z) A_1/A_2\}^2}{2(A_0 - A_1^2/A_2)} \right] \quad (\text{B4.2})$$

This pencil beam is now scanned over a large angle such that θ_0 varies, $-\theta_{0\text{max}} < \theta_0 < +\theta_{0\text{max}}$ producing a broad electron beam as shown in Figure 4.2. The moments of the broad beam distribution with respect to angle θ_x are defined as

$$\tilde{F}_i(z, x) = \int_{-\theta_{0\text{max}}}^{+\theta_{0\text{max}}} \int_{-\infty}^{+\infty} \theta_x^i F(z, x, \theta_x, \theta_0) d\theta_x d\theta_0 \quad (\text{B4.3})$$

This equation is solved most easily by performing the integration with respect to θ_x first.

First Moment, $F_0(z, x)$

$$F(z, x, \theta_0) = \int_{-\infty}^{+\infty} F(z, x, \theta_x, \theta_0) d\theta_x \quad (B4.4)$$

$$= \frac{1}{\sqrt{2\pi A_2}} \text{EXP} \left[-\frac{(x - \theta_0 z)^2}{2A_2} \right] \cdot \int_{-\infty}^{+\infty} \frac{d\theta_x}{\sqrt{2\pi(A_0 - A_1^2/A_2)}} \text{EXP} \left[-\frac{\{(\theta_x - \theta_0) - (x - \theta_0 z)A_1/A_2\}^2}{2(A_0 - A_1^2/A_2)} \right]$$

The integral I is computed to be unity by making the substitutions

$$\alpha = (A_0 - A_1^2/A_2) \quad (B4.5)$$

$$\Gamma = \{(\theta_x - \theta_0) - (x - \theta_0 z)A_1/A_2\} / \alpha \quad (B4.6)$$

and using the identity

$$\int_{-\infty}^{+\infty} \text{EXP} \left[-\frac{\Gamma^2}{2} \right] = 2\sqrt{\frac{\pi}{2}} \quad (B4.7)$$

Now,

$$\tilde{F}_0(z, x) = \int_{-\theta_{\max}}^{+\theta_{\max}} F(z, x, \theta) \cdot d\theta \quad (B4.8)$$

Making the substitution $\theta_0 = x'/z$, we obtain

$$\tilde{F}_0(z, x) = \frac{1}{z} \int_{-x'_{\max}}^{+x'_{\max}} \frac{1}{\sqrt{2\pi A_2}} \text{EXP} \left[-\frac{(x - x')^2}{2A_2} \right] dx' \quad (B4.9)$$

which may be evaluated by making a further substitution

$$\tilde{F}_0(z, x) = \frac{1}{z} \int_{+(x+x'_{\max})/\sqrt{A_2}}^{+(x-x'_{\max})/\sqrt{A_2}} \frac{-1}{\sqrt{2\pi}} \text{EXP} \left[-\frac{\Gamma^2}{2} \right] d\Gamma \quad (\text{B4.10})$$

or

$$\tilde{F}_0(z, x) = \frac{1}{z} \cdot \frac{1}{2} \cdot \left[\text{ERF} \left(\frac{x' - x}{\sqrt{2A_2}} \right) - \text{ERF} \left(\frac{-x' - x}{\sqrt{2A_2}} \right) \right] \quad (\text{B4.11})$$

Second Moment, $\tilde{F}_2(z, x)$

$$F_1(z, x, \theta_0) = \int_{-\infty}^{+\infty} \theta_x F(z, x, \theta_x, \theta_0) d\theta_x \quad (\text{B4.12})$$

making the substitutions given in Equations B4.5 and B4.6 and using the identity

$$\int_{-\infty}^{+\infty} \Gamma \text{EXP} \left[-\frac{\Gamma^2}{2} \right] d\Gamma = 0 \quad (\text{B4.13})$$

we obtain

$$F_1(z, x, \theta_0) = \frac{1}{\sqrt{2\pi A_2}} \cdot [(x - \theta_0 z) A_1 / A_2 + \theta_0] \cdot \text{EXP} \left[-\frac{(x - \theta_0 z)^2}{2A_2} \right] \quad (\text{B4.14})$$

Making the substitution $\theta_0 = x/z$, we can compute the second moment

$$\begin{aligned} \tilde{F}_1(z, x) &= \frac{1}{z} \int_{-x'_{\max}}^{+x'_{\max}} F_1(z, x, x') \cdot dx' \\ &= \frac{1}{z} \int_{-x'_{\max}}^{+x'_{\max}} \frac{1}{\sqrt{2\pi A_2}} \cdot \frac{A_1}{A_2} (x-x') \cdot \text{EXP} \left[-\frac{(x-x')^2}{2A_2} \right] dx' \\ &\quad + \frac{1}{z^2} \int_{-x'_{\max}}^{+x'_{\max}} \frac{1}{\sqrt{2\pi A_2}} \cdot x' \cdot \text{EXP} \left[-\frac{(x-x')^2}{2A_2} \right] dx' \end{aligned} \quad (\text{B4.15})$$

The first integral in this Equation I_1 , is easily evaluated upon making the substitution $U = (x-x')^2 / 2A_2$

$$I_1 = \frac{1}{z} \cdot \frac{A_1}{\sqrt{2\pi A_2}} \cdot \left\{ \text{EXP} \left[-\frac{(x-x'_{\max})^2}{2A_2} \right] - \text{EXP} \left[-\frac{(x+x'_{\max})^2}{2A_2} \right] \right\} \quad (\text{B4.16})$$

The second integral I_2 is split into two by the substitution

$\Gamma = (x-x')/\sqrt{A_2}$ and recognizing one part as $F_0(z, x)$ we have

$$I_2 = \frac{1}{z^2} \cdot \frac{A_2}{\sqrt{2\pi A_2}} \cdot \int_{+(x+x'_{\max})/\sqrt{A_2}}^{+(x-x'_{\max})/\sqrt{A_2}} \Gamma \cdot \text{EXP} \left[-\frac{\Gamma^2}{2} \right] d\Gamma + \frac{x}{z} \tilde{F}_0(z, x) \quad (\text{B4.17})$$

The integral in the equation for I_2 is evaluated by setting

So that

$$\begin{aligned} I_2 &= -\frac{1}{z^2} \cdot \frac{A_2}{\sqrt{2\pi A_2}} \cdot \left\{ \text{EXP} \left[-\frac{(x-x'_{\max})^2}{2A_2} \right] - \text{EXP} \left[-\frac{(x+x'_{\max})^2}{2A_2} \right] \right\} \quad (\text{B4.18}) \\ &\quad + \frac{x}{z} \cdot F_0(z, x) \end{aligned}$$

Adding Equations B4.16 and B4.18 for the second moment we obtain

$$\begin{aligned} \tilde{F}_1(z,x) = & \frac{1}{z} \cdot \frac{(A_1 - A_2/z)}{\sqrt{2\pi A_2}} \left\{ \text{EXP} \left[-\frac{(x-x'_{\max})^2}{2A_2} \right] - \text{EXP} \left[-\frac{(x+x'_{\max})^2}{2A_2} \right] \right\} \\ & + \frac{x}{z} \cdot \tilde{F}_0(z,x) \end{aligned} \quad (\text{B4.19})$$

Third Moment, $\tilde{F}_2(z,x)$

$$F_2(z,x,\theta_0) = \int_{-\infty}^{+\infty} \theta_x^2 F(z,x,\theta_x,\theta_0) d\theta_x \quad (\text{B4.20})$$

Making the substitutions given in Equations B4.5 and B4.6 and using the identities given in Equations B4.7 and B4.13 in addition to the identity

$$\int_{-\infty}^{+\infty} \Gamma^2 \cdot \text{EXP} \left[-\frac{\Gamma^2}{2} \right] d\Gamma = 2\sqrt{\frac{\pi}{2}} \quad (\text{B4.21})$$

then we obtain

$$\begin{aligned} F_2(z,x,\theta_0) = & \frac{1}{\sqrt{2\pi A_2}} \cdot \left[(A_0 - A_1^2/A_2) + [(x - \theta_0 z) A_1/A_2 + \theta_0]^2 \right] \\ & \cdot \text{EXP} \left[-\frac{(x - \theta_0 z)^2}{2A_2} \right] \end{aligned} \quad (\text{B4.22})$$

Making the substitution $\theta_0 = x'/z$, we can compute the third moment

$$\begin{aligned}
 \tilde{F}_2(z, x) &= \frac{1}{z} \cdot \int_{-x'_{\max}}^{+x'_{\max}} F_2(z, x, x') dx' \\
 &= \frac{1}{z} \cdot \int_{-x'_{\max}}^{+x'_{\max}} (A_0 - A_1^2/A_2) \cdot \lambda dx' \\
 &= \frac{1}{z} \cdot \int_{-x_{\max}}^{+x_{\max}} (x-x')^2 \frac{A_1^2}{A_2} \cdot \lambda dx' \\
 &= \frac{1}{z^2} \int_{-x_{\max}}^{+x_{\max}} 2x'(x-x') \frac{A_1}{A_2} \cdot \lambda dx' + \frac{1}{z^3} \int_{-x'_{\max}}^{+x'_{\max}} x'^2 \cdot \lambda dx'
 \end{aligned}$$

$$\text{where } \lambda = \frac{1}{\sqrt{2\pi A_2}} \text{EXP} \left[-\frac{(x-x')^2}{2A_2} \right] \quad (\text{B4.23})$$

The first integral I_1 in Equation B4.23 is recognizable as $\tilde{F}_0(z, x)$

$$I_1 = (A_0 - A_1^2/A_2) \cdot \tilde{F}_0(z, x) \quad (\text{B4.24})$$

The second integral I_2 is evaluated by making the substitution $\Gamma = (x-x')/\sqrt{A_2}$

$$I_2 = \frac{1}{z} \cdot \frac{A_1^2}{A_2} \cdot \frac{1}{\sqrt{2\pi}} \cdot \int_{+(x+x'_{\max})/\sqrt{A_2}}^{+(x-x'_{\max})/\sqrt{A_2}} \Gamma \cdot \Gamma \cdot \text{EXP} \left[-\frac{\Gamma^2}{2} \right] d\Gamma \quad (\text{B4.25})$$

Integrating by parts we obtain

$$I_2 = -\frac{1}{z} \frac{A_1^2}{A_2 \sqrt{2\pi}} \cdot \left\{ \frac{(x+x'_{\max})}{\sqrt{A_2}} \cdot \text{EXP} \left[-\frac{(x+x'_{\max})^2}{2A_2} \right] \right. \\ \left. - \frac{(x-x'_{\max})}{\sqrt{A_2}} \cdot \text{EXP} \left[-\frac{(x-x'_{\max})^2}{2A_2} \right] \right\} + \frac{A_1^2}{A_2} \tilde{F}_0(z, x) \quad (B4.26)$$

The third integral I_3 of Equation B4.23 is similarly computed by making the substitution $\Gamma = (x-x')/\sqrt{A_2}$ to obtain

$$I_3 = -\frac{1}{z^2} \frac{2A_1 x}{\sqrt{2\pi A_2}} \cdot \int_{+(x+x'_{\max})/\sqrt{A_2}}^{+(x-x'_{\max})/\sqrt{A_2}} \Gamma \cdot \text{EXP} \left[-\frac{\Gamma^2}{2} \right] d\Gamma \\ + \frac{1}{z^2} \frac{2\sqrt{A_2} A_1}{\sqrt{2\pi A_2}} \cdot \int_{+(x+x'_{\max})/\sqrt{A_2}}^{+(x-x'_{\max})/\sqrt{A_2}} \Gamma^2 \text{EXP} \left[-\frac{\Gamma^2}{2} \right] d\Gamma \quad (B4.27)$$

These integrals have been previously evaluated for Equations B4.18 and B4.25, therefore we have

$$I_3 = -\frac{1}{z^2} \frac{2A_1 x}{\sqrt{2\pi A_2}} \cdot \left\{ \text{EXP} \left[-\frac{(x-x'_{\max})^2}{2A_2} \right] - \text{EXP} \left[-\frac{(x+x'_{\max})^2}{2A_2} \right] \right\} \\ + \frac{1}{z^2} \frac{2\sqrt{A_2} A_1}{\sqrt{2\pi A_2}} \cdot \left\{ \frac{(x+x'_{\max})}{\sqrt{A_2}} \text{EXP} \left[-\frac{(x+x'_{\max})^2}{2A_2} \right] \right. \\ \left. - \frac{(x-x'_{\max})}{\sqrt{A_2}} \text{EXP} \left[-\frac{(x-x'_{\max})^2}{2A_2} \right] \right\} + \frac{1}{z} \frac{A_1}{2} \tilde{F}_0(z, x) \quad (B4.28)$$

The fourth and final integral I_4 of Equation B4.23 is again computed by making the substitution $\Gamma = (x-x')/\sqrt{A_2}$ to obtain

$$\begin{aligned}
 I_4 = & -\frac{1 \cdot A_2^{3/2}}{z^3 \sqrt{2\pi A_2}} \int_{+(x+x'_{\max})/\sqrt{A_2}}^{+(x-x'_{\max})/\sqrt{A_2}} \Gamma^2 \cdot \text{EXP} \left[-\frac{\Gamma^2}{2} \right] d\Gamma \\
 & + \frac{1 \cdot 2A_2 x}{z^3 \sqrt{2\pi A_2}} \int_{+(x+x'_{\max})/\sqrt{A_2}}^{+(x-x'_{\max})/\sqrt{A_2}} \Gamma \cdot \text{EXP} \left[-\frac{\Gamma^2}{2} \right] d\Gamma \\
 & - \frac{1 \cdot \sqrt{A_2} x^2}{z^3 \sqrt{2\pi A_2}} \int_{+(x+x'_{\max})/\sqrt{A_2}}^{+(x-x'_{\max})/\sqrt{A_2}} \text{EXP} \left[-\frac{\Gamma^2}{2} \right] d\Gamma \quad (B4.29)
 \end{aligned}$$

Again, all these integrals have been previously evaluated for Equations B4.10, B4.18 and B4.25, therefore we have

$$\begin{aligned}
 I_4 = & -\frac{1 \cdot A_2}{z^3 \sqrt{2\pi A_2}} \left\{ (x-x'_{\max}) \text{EXP} \left[-\frac{(x+x'_{\max})^2}{2A_2} \right] \right. \\
 & \left. - (x-x'_{\max}) \text{EXP} \left[-\frac{(x-x'_{\max})^2}{2A_2} \right] \right\} \\
 & + \frac{A_2}{z^2} \cdot \tilde{F}_0(z, x) \\
 & - \frac{1 \cdot 2A_2 x}{z^3 \sqrt{2\pi A_2}} \left\{ \text{EXP} \left[-\frac{(x-x'_{\max})^2}{2A_2} \right] - \text{EXP} \left[-\frac{(x+x'_{\max})^2}{2A_2} \right] \right\} \\
 & + \frac{x^2}{z^2} \cdot \tilde{F}_0(z, x) \quad (B4.30)
 \end{aligned}$$

Gathering terms for the third moment $F_2(z, x)$ and simplifying we obtain

$$\begin{aligned} \tilde{F}_2(z, x) &= \left[A_0 - \frac{2A_1}{z} + \frac{A_2}{z^2} + \frac{x^2}{z^2} \right] \cdot \tilde{F}_0(z, x) \\ &+ \left[\frac{A_1 - A_2}{z} \right] \cdot \frac{2x}{\sqrt{2\pi A_2}} \cdot \frac{1}{z^2} \cdot \left\{ \text{EXP} \left[-\frac{(x - x'_{\max})^2}{2A_2} \right] \right. \\ &\quad \left. - \text{EXP} \left[-\frac{(x + x'_{\max})^2}{2A_2} \right] \right\} \quad (B4.31) \\ &+ \left[\frac{A_1 - A_2}{z} \right]^2 \cdot \frac{1}{A_2 z} \cdot \left\{ \frac{(x - x'_{\max}) \cdot \text{EXP} \left[-\frac{(x - x'_{\max})^2}{2A_2} \right]}{\sqrt{2\pi A_2}} \right. \\ &\quad \left. - \frac{(x + x'_{\max}) \cdot \text{EXP} \left[-\frac{(x + x'_{\max})^2}{2A_2} \right]}{\sqrt{2\pi A_2}} \right\} \end{aligned}$$

Chapter 5

APPLICATION OF FERMI-EYGES SCATTERING THEORY TO
MAGNETICALLY SCANNED THERAPEUTIC ELECTRON BEAMS IN AIR

5.1 Introduction

Treating broad electron beams as a summation of pencil beams has grown in popularity because it is a convenient computational tool which may be used to calculate dose from irregularly shaped treatment fields (Brahme et al 1981) or account for patient contour (Lillicrap et al 1975, Loyd and Rosen 1985). Current theoretical pencil beam approaches to electron dose computation use a solution to the electron transport equation first derived by Fermi (Rossi and Greisen 1941). This theory only accounts for the dominant electron interaction process of multiple small-angle scattering but energy loss has also been incorporated to a limited extent by using the Eyges solution (Eyges 1948) to the Fermi transport equation. The neglect of the remaining higher-order interaction processes of large-angle scattering, delta-ray production, electron absorption and bremsstrahlung production, requires present tissue dose computation algorithms based on Fermi-Eyges theory (Hogstrom et al 1981, Storchi and Huizenga 1985) to use empirically derived input data. These algorithms may therefore be legitimately termed semi-empirical. Attempts to remove this empiricism by inclusion of higher-order interaction effects into the theory are the subject of current research (Jette et al 1985, Jette 1986b). In spite of these difficulties, the use of Fermi-Eyges theory in electron dose computation algorithms offers the promise of a strong theoretical basis to

account for heterogeneities (Perry and Holt 1980, Goitein et al 1978) and compared to other semi-empirical algorithms (Rozenfeld et al 1969, Kawachi 1975, Nath et al 1980) allows a significant reduction in the number of measurements required as input data.

The application of this theory to model broad therapeutic electron beams produced by linear accelerators is not trivial, even in the air space above patients, which is a region where energy loss and higher-order interaction processes are negligibly small. This has led previous workers to resort to empirical procedures for obtaining input parameters to the Fermi-Eyges theory by considering air scattering as equivalent to a fictitious scattering layer of tissue over the actual surface (Van Gasteren 1984, Werner et al 1982) or to determine theoretical input parameters from measured data rather than calculations from first principles (Hogstrom 1985). In contrast, ICRU report 35 (ICRU 1984a) presents a detailed analysis of broad beam characterization on the basis of Fermi theory. This particular approach suffers from several practical drawbacks. It poses major problems in implementation because of the large number of theoretical parameters and uncertainties as to how they could be experimentally determined. Furthermore, it does not include the effects of the collimation system and its formalism is not appropriate for magnetically scanned electron beam linear accelerators because it was developed for a scattering-foil type accelerator.

This chapter presents a simple scheme which may be used to characterize magnetically scanned broad electron beams from the Sagittaire Therac 40 linear accelerator in the air space above the patient. The accelerator model utilizes the solution to the Fermi transport equation derived by Jette et al (1983) for a point isotropic electron source to accurately predict the shape of broad beam profiles for any beam geometry and energy, with or without collimation and shielding and also the beam output in air. The predictive power of this model supports its use as an important component of treatment planning dose calculations and provides a logical first step toward a theoretical understanding of the behaviour of therapeutic electrons at depth in tissue.

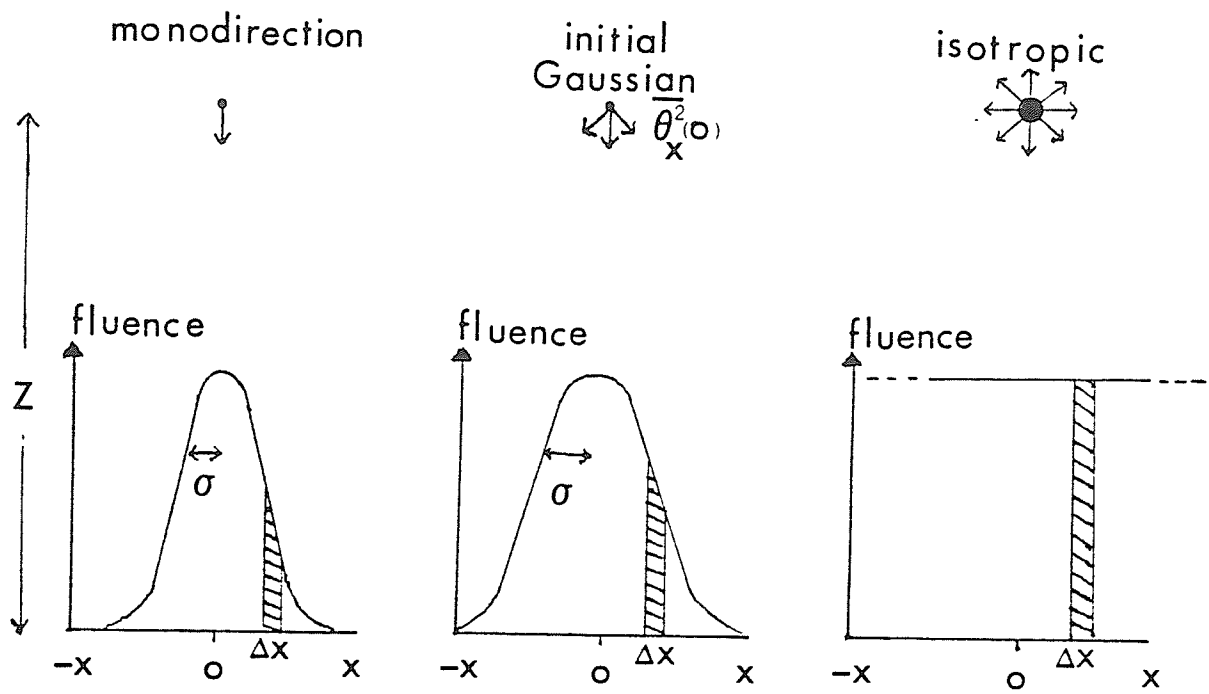
5.2 Fermi-Eyges Theory

The Fermi transport equation is a second-order differential equation which describes the diffusion of electrons under small-angle scattering conditions. This equation was originally solved in closed form to provide the distribution function for a point, monodirectional, monoenergetic source of electrons incident upon a semi-infinite scattering medium. This particular solution (Rossi and Greisen 1941) defines a Gaussian spatial distribution of electrons at depth and a Gaussian angular distribution of electrons independent of lateral position, although the most probable angle of travel increases with lateral position. The transport equation may also be solved in closed form for a number

of other simple boundary conditions (Huizenga 1986). These include the point isotropic source (Jette et al 1981) and the point source with an initial Gaussian distribution of angles (ICRU 1984a).

The solution for a monodirectional point source or a point source with an initial Gaussian angular distribution is commonly called a pencil beam. Magnetic scanning of a pencil beam over a large angular range produces a broad diverging beam. The angular distribution of the electrons in the broad beam at depth in the scattering medium is different from that of a single pencil beam. Indeed, neglecting field edge effects, the angular distribution at depth in the scanned broad beam is independent of any initial Gaussian angular distribution associated with the pencil beam and equals that due to an isotropic source (Chapter 4, Equation 4.49). Figure 5.1 schematically represents the electron distribution from the three different point sources incident upon a semi-infinite air medium under small-angle scattering conditions. The table inset to Figure 5.1 lists three of the parameters which are commonly used to describe the electron distribution emanating from a point source. Advantage is taken of the rotational symmetry of the distribution to quote only the parameter values projected on to the (z,x) plane. The parameters listed are the most probable direction of travel of the electrons $\bar{\theta}_x(z,x)$ at depth z and lateral position x, the mean square angle of travel of all

Figure 5.1: Spatial fluence, most probable angle of travel and mean square angle of travel of electrons from three point sources incident upon a semi-infinite air medium.



$\overline{\theta_x(z,x)}$ only includes electrons in Δx
 $\overline{\theta_x^2(z)}$ includes all electrons

TYPE OF POINT SOURCE	$\overline{\theta_x(z,x)}$	$\overline{\theta_x^2(z)}$	$\sigma^2(z)$
Monodirectional	$\frac{3}{2} \cdot \frac{X}{Z}$	$k \cdot \frac{Z}{2}$	$k \cdot \frac{Z^3}{6}$
Initial Gaussian Angular Distribution	$\frac{3}{2} \cdot \frac{X}{Z}$	$\overline{\theta_x^2(0)} + k \cdot \frac{Z}{2}$	$\overline{\theta_x^2(0)} \cdot Z^2 + k \cdot \frac{Z^3}{6}$
ISOTROPIC	$\frac{X}{Z}$	$k \cdot \frac{Z}{6}$	—

the electrons $\overline{\theta_x^2}(z)$ at depth z and the variance of the Gaussian spatial spread σ^2 of a pencil beam at depth z in the air medium. The table insert to Figure 5.1 also shows that the projected mean square angle of travel $\overline{\theta_x^2}(z)$ for an isotropic point source is a factor of three less than for the monodirectional point source. The value of $\overline{\theta_x^2}(z)$ depends strongly on beam energy through the linear angular scattering power k (Equation 5.1). The procedure described by Jette et al (1985) was used to calculate k at each beam energy.

$$\overline{\theta_x^2}(z) = \frac{k(E)z}{6} \quad (5.1)$$

where $k(E)$ is the linear angular scattering power of air at the energy E of the electron beam, and is given in Table 5.1 for selected beam energies.

5.3 Relationship Between Broad Beams and Pencil Beams

The spatial distribution of electron fluence $F(z,x,y)$ for a magnetically scanned broad rectangular field may be computed by considering the electron source as an isotropic point source. This isotropic source is composed of a set of diverging pencil beams about the most probable direction of travel of the electrons and is collimated to form the field

$$F(z,x,y) = \frac{1}{z^2} \cdot \frac{1}{4} \cdot \left[\frac{\text{ERF}\left(\frac{a-x}{\sqrt{2}\sigma}\right) - \text{ERF}\left(\frac{-a-x}{\sqrt{2}\sigma}\right)}{\right] \cdot \left[\frac{\text{ERF}\left(\frac{b-y}{\sqrt{2}\sigma}\right) - \text{ERF}\left(\frac{-b-y}{\sqrt{2}\sigma}\right)}{\right] \quad (5.2)$$

Table 5.1

Variation of linear scattering power k in air with electron beam energies of the Sagittaire Therac 40 accelerator

Nominal Electron Beam Energy (MeV)	Linear Scattering* Power of air (cm ⁻¹)
7	25.93x10 ⁻⁵
10	13.17x10 ⁻⁵
13	7.96x10 ⁻⁵
16	5.33x10 ⁻⁵
19	3.81x10 ⁻⁵
22	2.86x10 ⁻⁵
25	2.22x10 ⁻⁵
28	1.78x10 ⁻⁵
32	1.32x10 ⁻⁵

$$* k(E) = k_0 \left[\frac{m_0 c^2 (E + m_0 c^2)}{E(E + 2m_0 c^2)} \right]^2$$

$$\text{where } k_0 = 16 \pi r_e^2 N_0 \rho \sum_i f_i Z_i (Z_i + 1) \ln(204 Z_i^{-1/3}) / A_i$$

E = beam energy in MeV, $m_0 c^2 = 0.511$ MeV

r_e = the classical electron radius = 2.817938×10^{-13} cm

N_0 = Avogadro's Number = 6.022045×10^{23} atoms per gram atom

ρ = density = 1.205×10^{-3} gcm⁻³

f_i = fraction by weight of element Z_i of atomic number A_i

where $a(z)$ is the half-field width at depth z defined by the collimation system in the x -direction, $b(z)$ is the half-field length at depth z defined by the collimation system in the y -direction, x and y are lateral coordinates, and σ is the root mean square spatial spread of a pencil beam at depth z when defined at the level of the collimation.

Considering the broad electron beam as a set of diverging pencil beams is advantageous because, whenever collimation is introduced, the broad beam may be redefined at the level z of the collimation as a new set of diverging pencil beams and propagated according to Fermi-Eyges theory (Figure 5.2). The root mean square (rms) spatial spread $\sigma(z)$ of the pencil beams at z is then given by (ICRU 1984a)

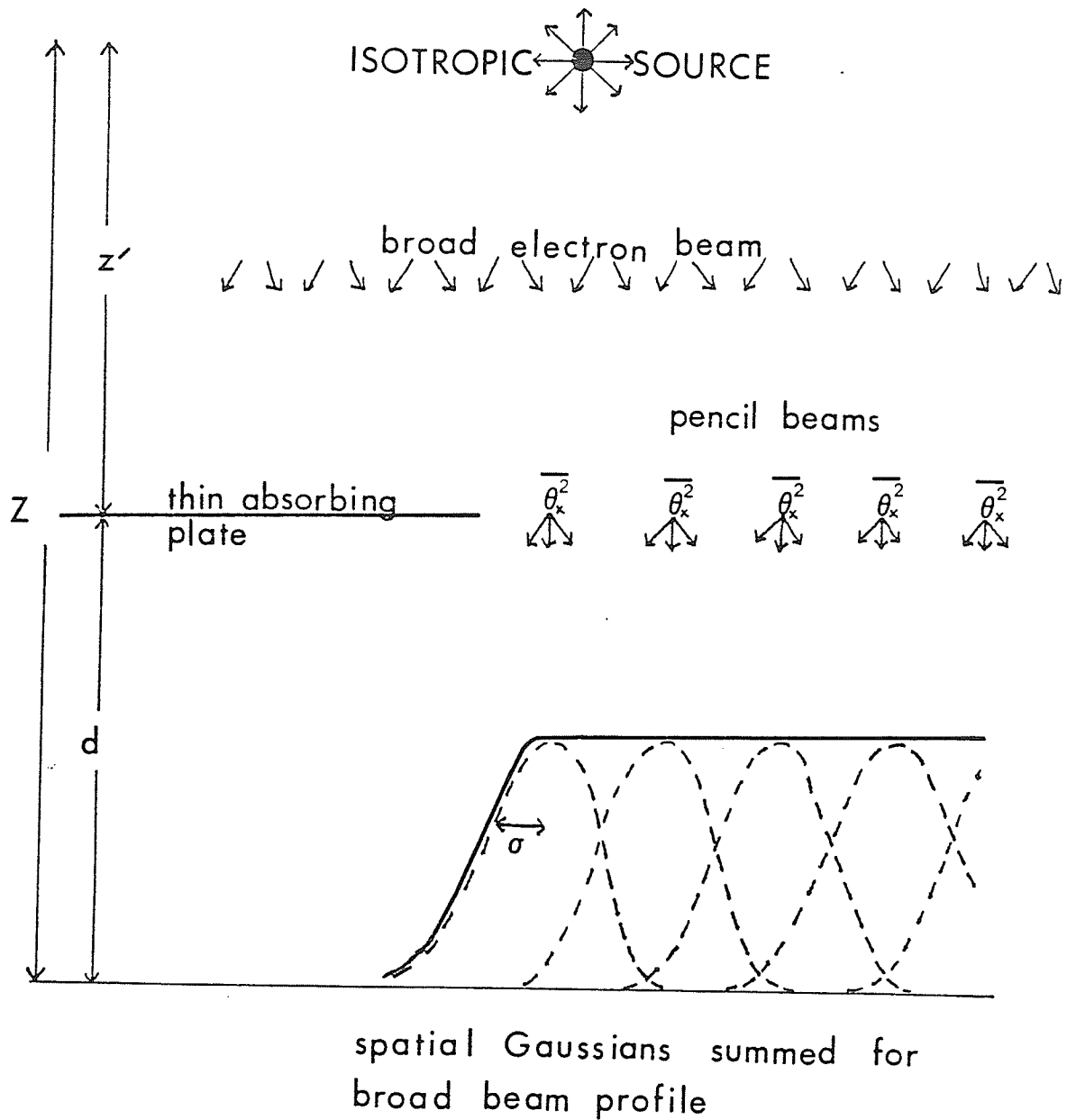
$$\sigma^2(z) = \overline{\theta_x^2}(z') \cdot d^2 + \sigma^2 \text{ mcs}(d) \quad (5.3)$$

where $\overline{\theta_x^2}(z')$ is the mean square angle of travel of the electrons at depth z' from the source. The term $\sigma^2 \text{ mcs}$ is due to multiple coulomb scattering in the distance d of air between z' and z and may be computed using Equation 5.4.

$$\sigma^2 \text{ mcs} = k(E) \cdot d^3/6 \quad (5.4)$$

Relationships between broad beam penumbra width, formed below collimation and the value of rms pencil beam spread $\sigma(z)$ may be derived from Equation 5.2 (Van Gasteren 1984, Hogstrom 1985). The penumbra width $W(z)$ is defined as the distance bet-

Figure 5.2: Spatial variance of a Gaussian pencil beam at depth z when defined at a collimator positioned at distance z' beyond an isotropic point source.



VARIANCE OF SPATIAL GAUSSIAN AT DEPTH z

$$\sigma^2(z) = \overline{\theta_x^2}(z')d^2 + \sigma_{mcs}^2(d)$$

ween the intersections of the tangent at the 50% point with the 100% and 0% dose levels of a normalized beam profile (Figure 5.3). Using this definition, the relationship between penumbra width $W(z)$ and $\sigma(z)$ for a large square field is (Van Gasteren 1984)

$$W(z) = \sqrt{2\pi} \sigma(z) \quad (5.5)$$

Figure 5.4 shows how closely the values of $\sigma(z)$ derived from Equation 5.5 using the penumbra width of a 20 x 20 cm² field predict measured beam profiles when substituted into Equation 5.2. The agreement between the predicted and measured profiles is very good. The small discrepancies which occur close to the 100% level are due to the beams produced by magnetic scanning in the Sagittaire accelerator being limited to a $\pm 5\%$ uniformity in the centre of large fields.

In the more general cases of a square field of arbitrary size or one which is blocked parallel to a field edge to form a rectangular field, the relationships between $W(z)$ and $\sigma(z)$ are more complex and must be solved iteratively. Appendix 5.1 derives these more general relationships which should be used instead of Equation 5.5, for the computation of $\sigma(z)$ where appropriate.

5.4 Lateral Scatter Disequilibrium

The central axis fluence $F(z,0,0)$ for a diverging square field may be derived from Equation 5.2 assuming the field colli-

Figure 5.3: Definition of penumbra width for the central plane of a broad beam profile.

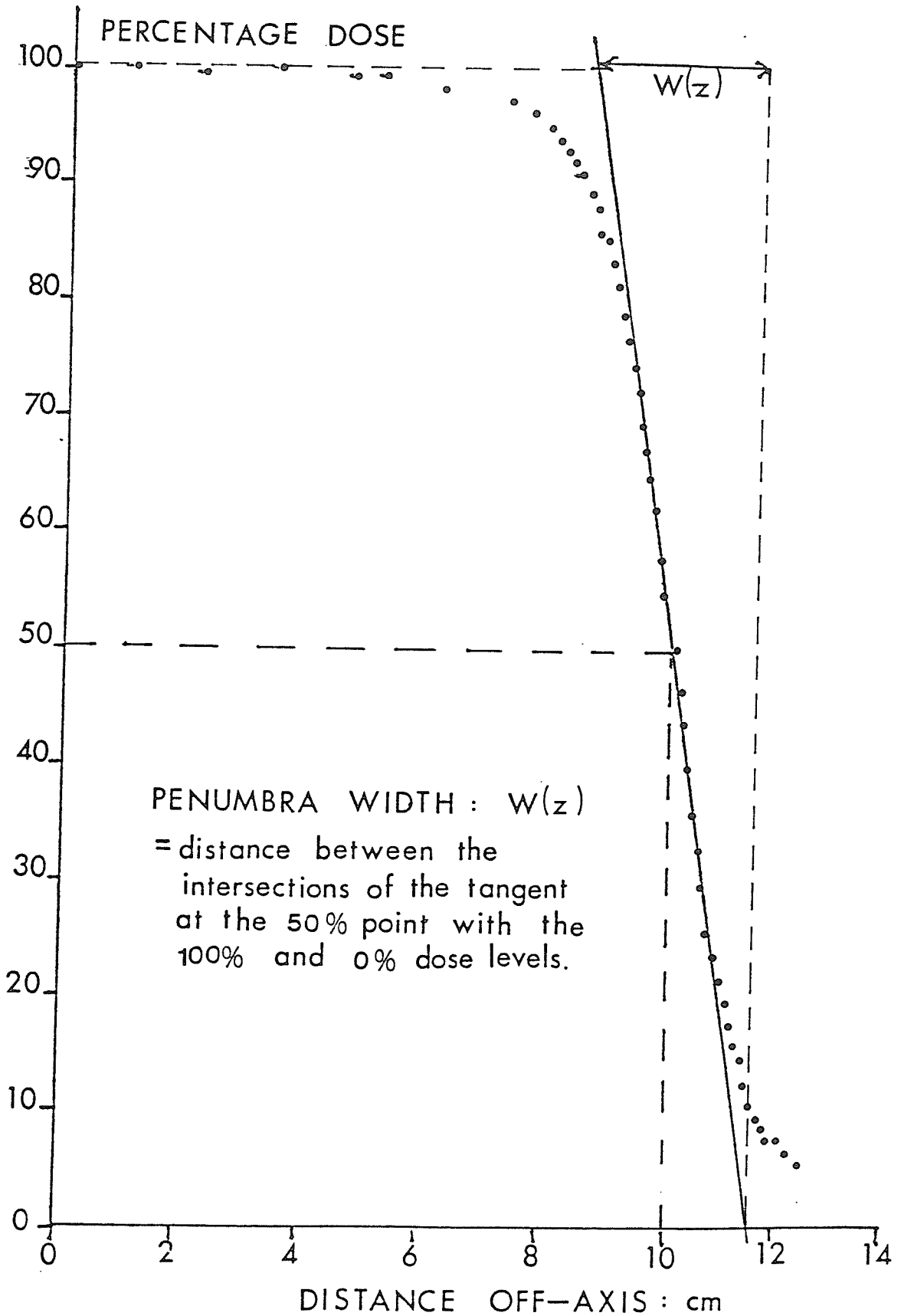
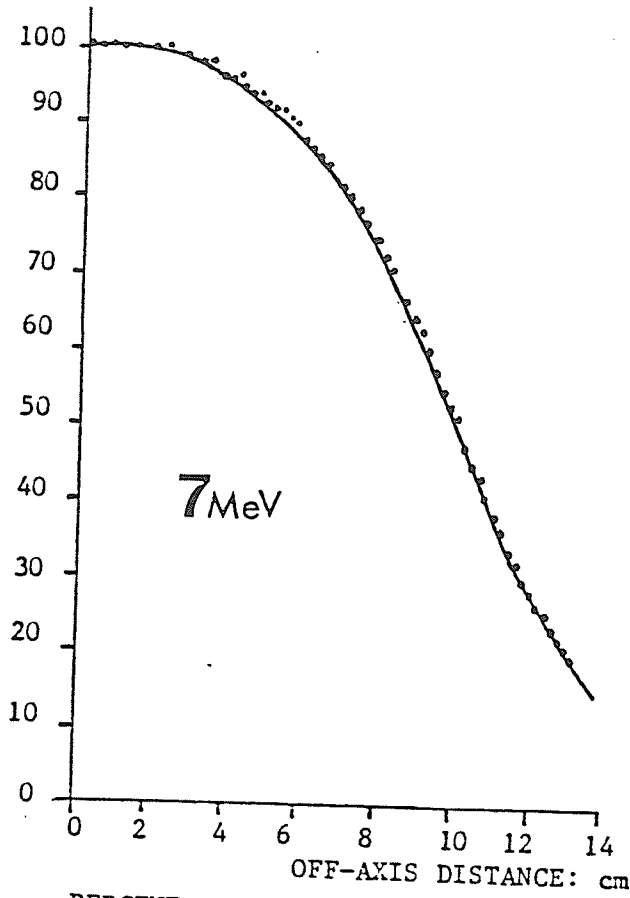
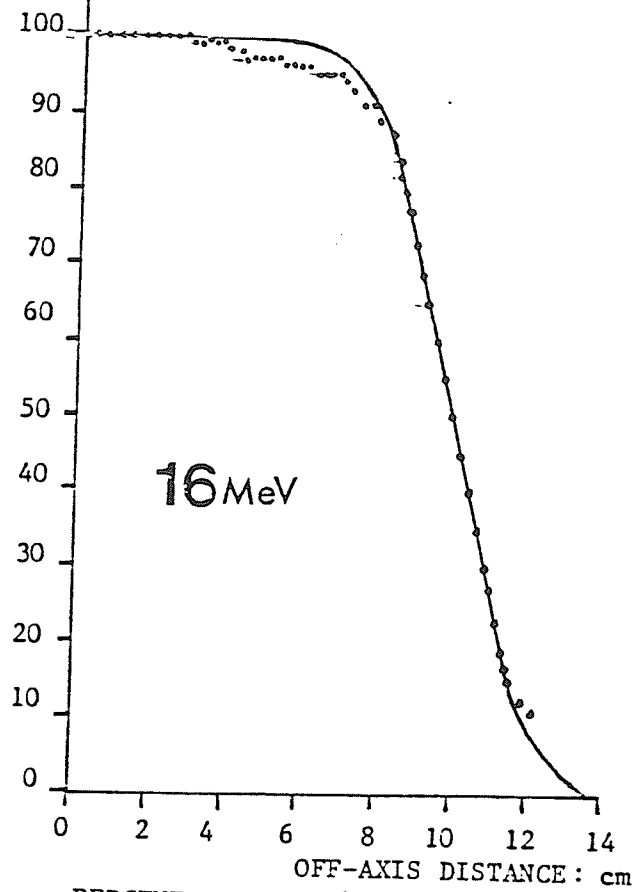


Figure 5.4: Comparison of predicted beam profiles (full lines) for a 20 x 20 cm field to the measured data for 7, 16, 22 and 32 MeV energies. Only half the profile is shown.

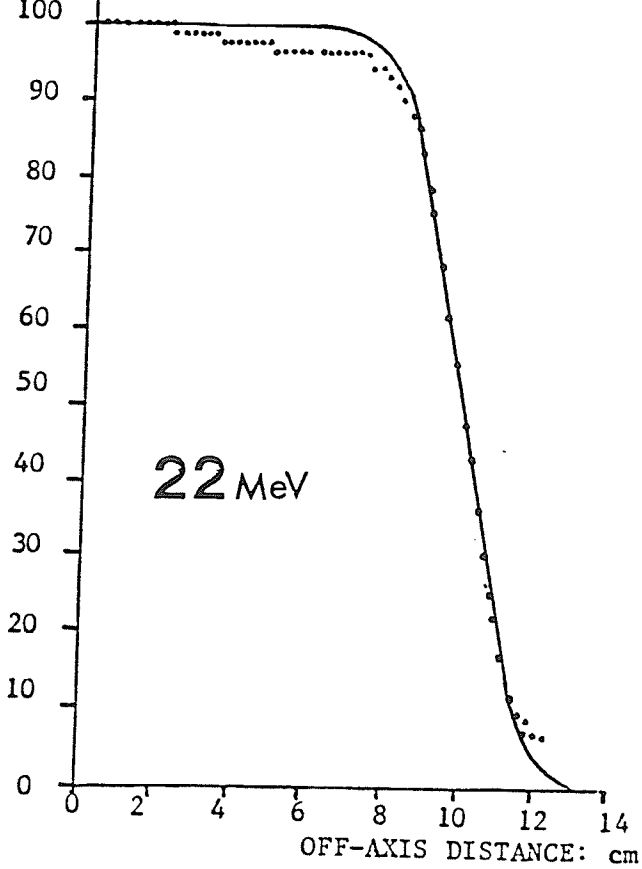
PERCENTAGE DOSE



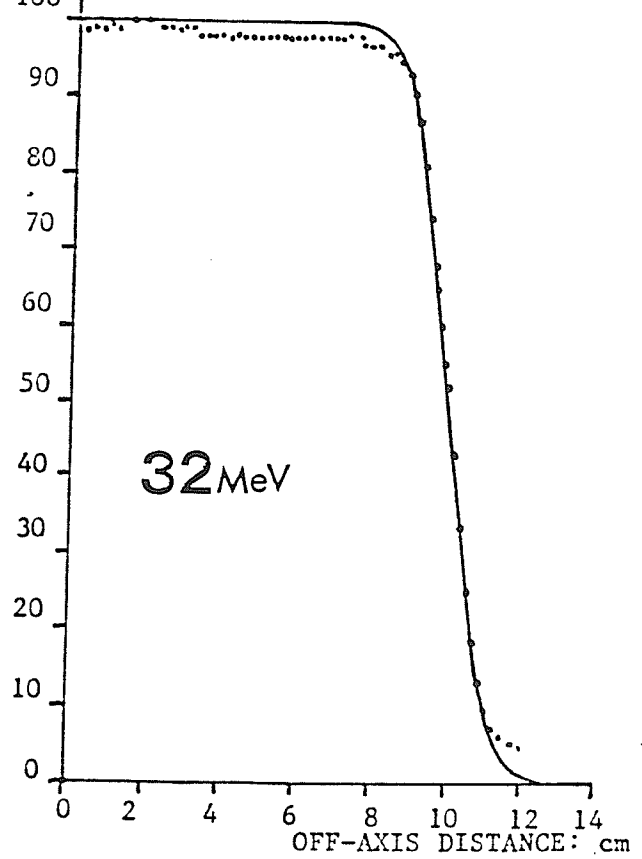
PERCENTAGE DOSE



PERCENTAGE DOSE



PERCENTAGE DOSE



mation is coplanar in the x and y direction.

$$F(z,0,0) = \frac{1}{z^2} \left[\text{ERF} \frac{a}{\sqrt{2}\sigma} \right]^2 \quad (5.6)$$

Lateral scatter disequilibrium for a rectangular field (Mills et al 1985) occurs when the penumbra width is greater than or approximately equal to half the corresponding field dimension (i.e. $a \lesssim \sigma$). This results in the error function term in Equation 5.6 decreasing below unity and reduces the fluence on the central axis of the beam below that expected on the basis of the simple inverse square law. A further consequence of lateral scatter disequilibrium is the increase in full width at half maximum (FWHM) of the field profile $F(z,x,0)$ when normalized to the central axis value $F(z,0,0)$.

$$\frac{F(z,x,0)}{F(z,0,0)} = \frac{\text{ERF}[(a-x)/\sqrt{2}\sigma] - \text{ERF}[(-a-x)/\sqrt{2}\sigma]}{2\text{ERF}(a/\sqrt{2}\sigma)} \quad (5.7)$$

The value of the FWHM is given by $2x$, where x is the solution to Equation 5.7 when the ratio $F(z,x,0)/F(z,0,0)$ equals 1/2. This value of x is obtained iteratively from the equation

$$\text{ERF} \frac{a}{\sqrt{2}\sigma} = \text{ERF} \frac{(a-x)}{\sqrt{2}\sigma} - \text{ERF} \frac{(-a-x)}{\sqrt{2}\sigma} \quad (5.8)$$

5.5 Accelerator Model for Broad Beam Penumbra Formation

The Sagittaire Therac 40 (Aucouturier 1970) is a linear accelerator capable of producing electron beams in the energy range 7 MeV to 32 MeV in steps of 3 MeV (Figure 5.5). The accelerator beam is focussed by an achromatic 127° magnet before emerging from an aluminum exit window. This beam is then scanned in a raster fashion within a cone of half-angle equal to 14° by a magnetic quadrupole. Broad therapeutic electron beams produced by this magnetic scanning are modelled by an isotropic point source (Figure 5.6).

The scanned beam passes through a four quadrant monitor chamber which is used to measure dose rate, the integrated dose and to check the symmetry of the scanning action. The dimensions of the useful beam is limited by the cone shaped primary collimator, situated in the treatment head, to a 50 cm diameter field at 100 cm SSD (Figure 5.5). The field size can be reduced by a variable double collimator system from a 36 cm x 36 cm field down to a minimum of a 2 cm x 2 cm field at 100 cm source surface distance (SSD). This collimation system is symmetrical and non-coplanar in the x and y directions. It consists of two thick lead blocks in each lateral direction separated by some distance in the z direction, with the block edges aligned along a diverging ray emanating from the source. At greater distances in the z direction the broad beam may be further restricted by

Figure 5.5: Schematic of the treatment head of the Sagittaire
Therac 40 accelerator.

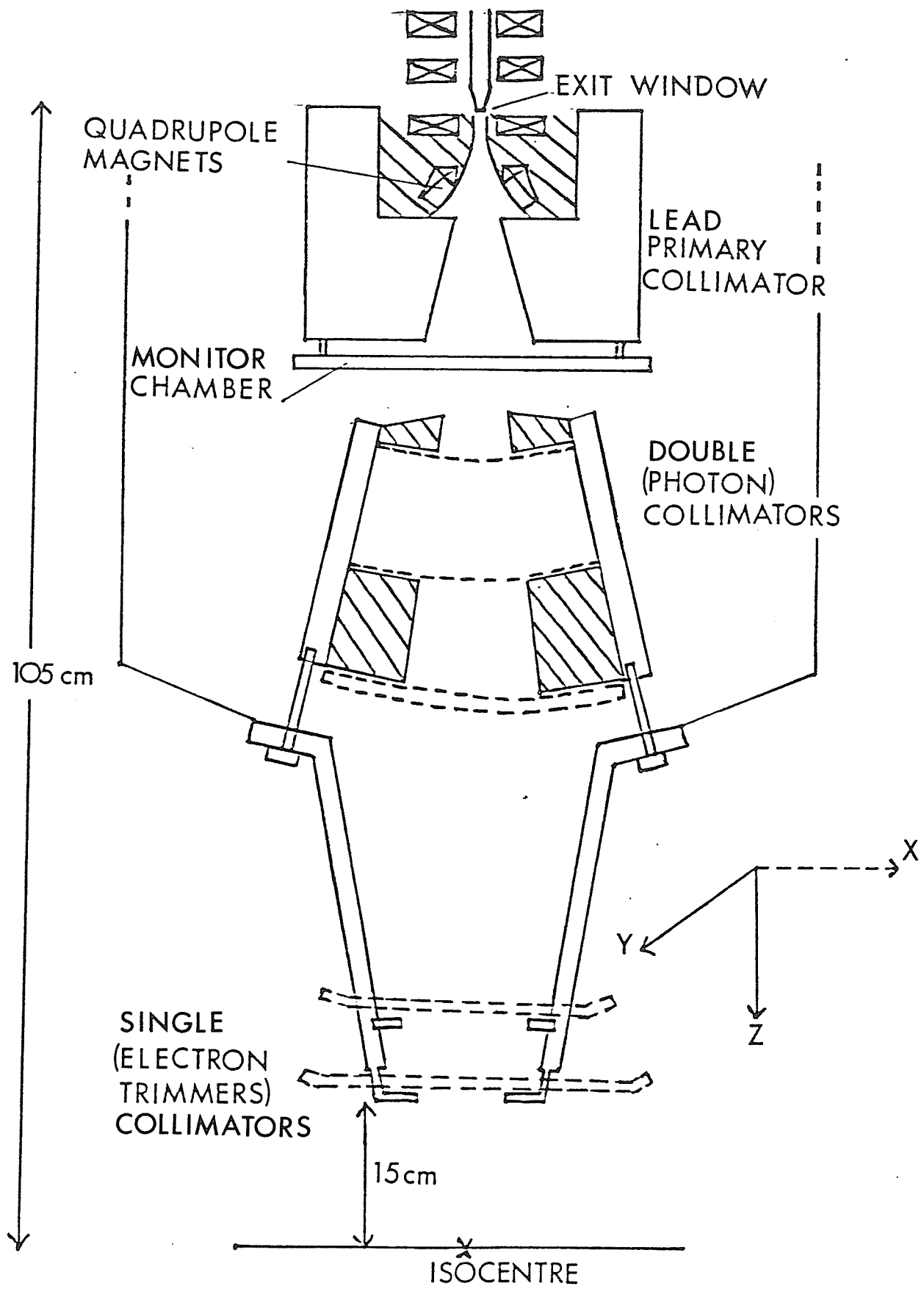
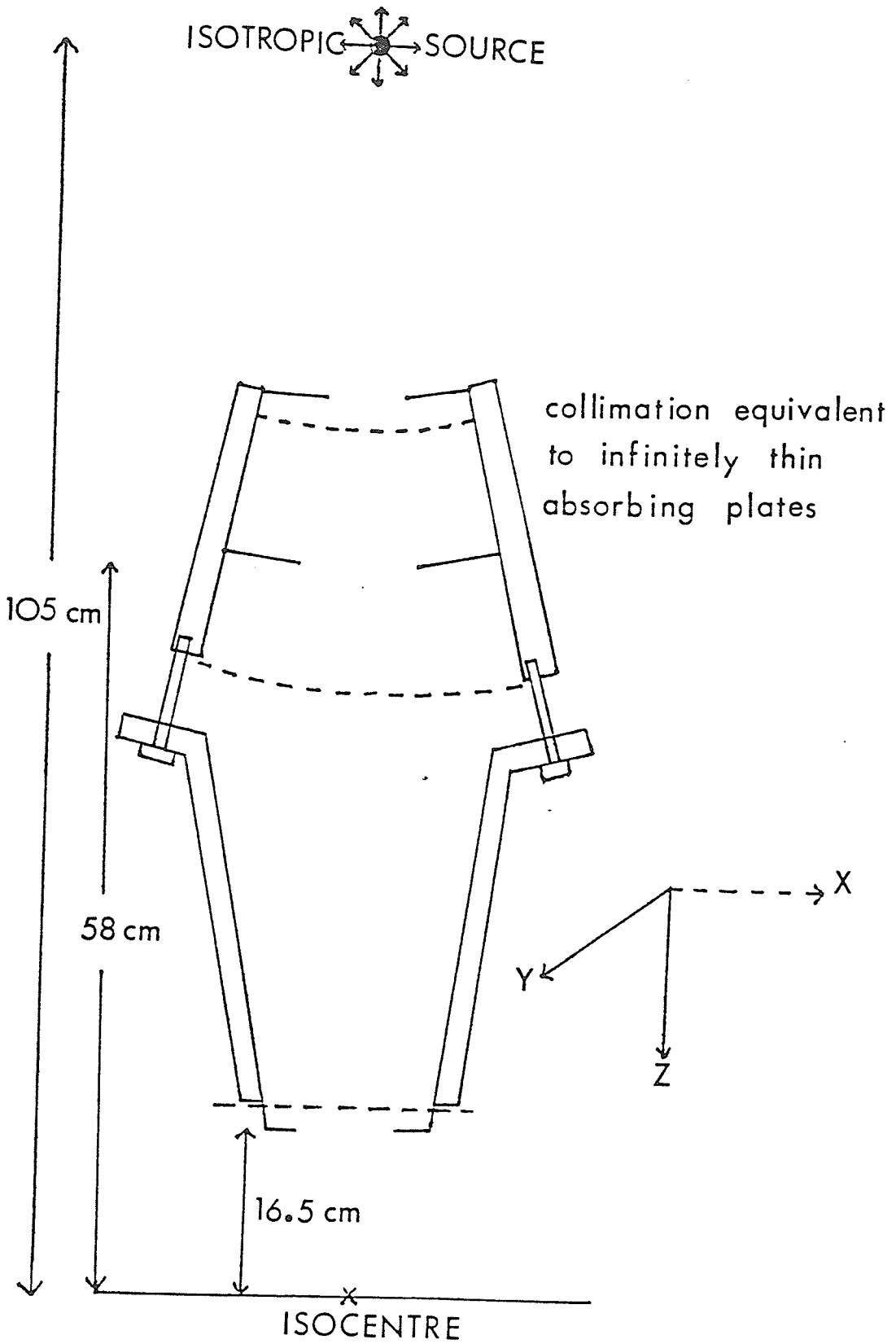


Figure 5.6: Accelerator model used to compute broad beam dose distributions.



shielding or single collimators sometimes known as trimmers. The trimmers are used clinically to compensate for the loss of field flatness and increased penumbra width at low electron beam energies. Each trimmer is attached to one of the double collimators and moves in synchrony such that it always protrudes about four centimeters into the field formed by the double collimator system. The trimmers are composed of two symmetrical and non-coplanar lead blocks in the x and y directions but only the lower lead block is responsible for penumbra formation and hence the label single collimator for a trimmer. The maximum field size possible at 100 cm SSD with trimmers attached is reduced to 28 cm x 28 cm. Normally a SSD of 100 cm is used for treatment, however, the minimum available is about 90 cm with trimmers attached and 60 cm without.

Each of the thick lead blocks responsible for penumbra formation is modelled as an infinitely thin absorbing plate. The model is a good approximation and is discussed in detail in the results section. This plate is assumed to be located at a level corresponding to the thick lead block surface closest to the radiation source (Figure 5.6).

5.6 Materials and Method

In-air beam profile measurements were obtained perpendicularly to the central axis of the therapy electron beam using Kodak Industrex M film. The film was pinned to a wooden box

frame and held perpendicular to the incident beam. Metal supports attached to the wooden box frame were used to position lead blocks in the field at various heights above the film. For convenience, the film was retained within the manufacturers opaque paper cassette when used. An optical density-dose calibration curve was obtained at the depth of dose maximum in a tissue equivalent phantom composed of Temex (Stacey et al 1961), for each electron beam energy. The film was found to be linear within two percent for doses in the range 5 - 30 cGy. To ensure greatest sensitivity in this linear region for penumbra measurements, the maximum of each profile was made to correspond to an optical density in the range 1.5 - 2.0. Films from the same batch were used in each specified experiment and developed under identical conditions using hand processing. The films were then read manually by a Sargent-Welch densitometer (Densichron model PPD) using a 1 mm diameter light aperture.

The radiation output factor in air is defined as the ratio of the ionization on the central axis of a field of interest at 100 cm SSD to that of a reference field size. The reference field size adopted in this work was a 36 cm x 36 cm square field. In-air ionization measurements were performed using a Capintec Farmer Type PR-06C ionization chamber of 0.65 ml sensitive volume, inner axial length 2.2 cm and inner diameter of 0.7 cm. Selected beam energies of 7,10,16,22 and 32 MeV were investigated

for square field sizes in the range 3 cm x 3 cm to 36 cm x 36 cm at various SSD.

In this work errors were determined by computing the standard deviation of not less than five repeat measurements for selected data points. This is indicated by an error bar on data symbols for the graphs.

5.7 Results

5.7.1 Static Beam Profile Measurements

The magnetic quadrupole scanning mechanism for the accelerator was switched-off and static accelerator beam profiles measured at 60,80,90 and 100 cm SSD. Figure 5.7 shows the measured static beam profiles in the x and y directions at 100 cm SSD for a 22 MeV beam energy. A Gaussian regression fit to these data, shown as a full line in Figure 5.7, demonstrates a smaller root mean square deviation in the x-direction compared to the y-direction. This indicates the static beam to be elliptical in shape. Figure 5.8 shows that the measured rms spread of the static accelerator beam with SSD may be well fit by the predicted spread of a pencil beam with an initial Gaussian angular distribution, according to Fermi-Eyges theory (see the table insert to Figure 5.1). Equation 5.3 defines the straight line plot in Figure 5.8 whose gradient is the initial mean square angular spread of the

Figure 5.7: Static accelerator beam profiles in the X and Y directions at 100 cm SSD for a 22 MeV beam. Gaussian regression fit shown as a full curve.

X-DIRECTION

Y-DIRECTION

22MEV AT 100CM

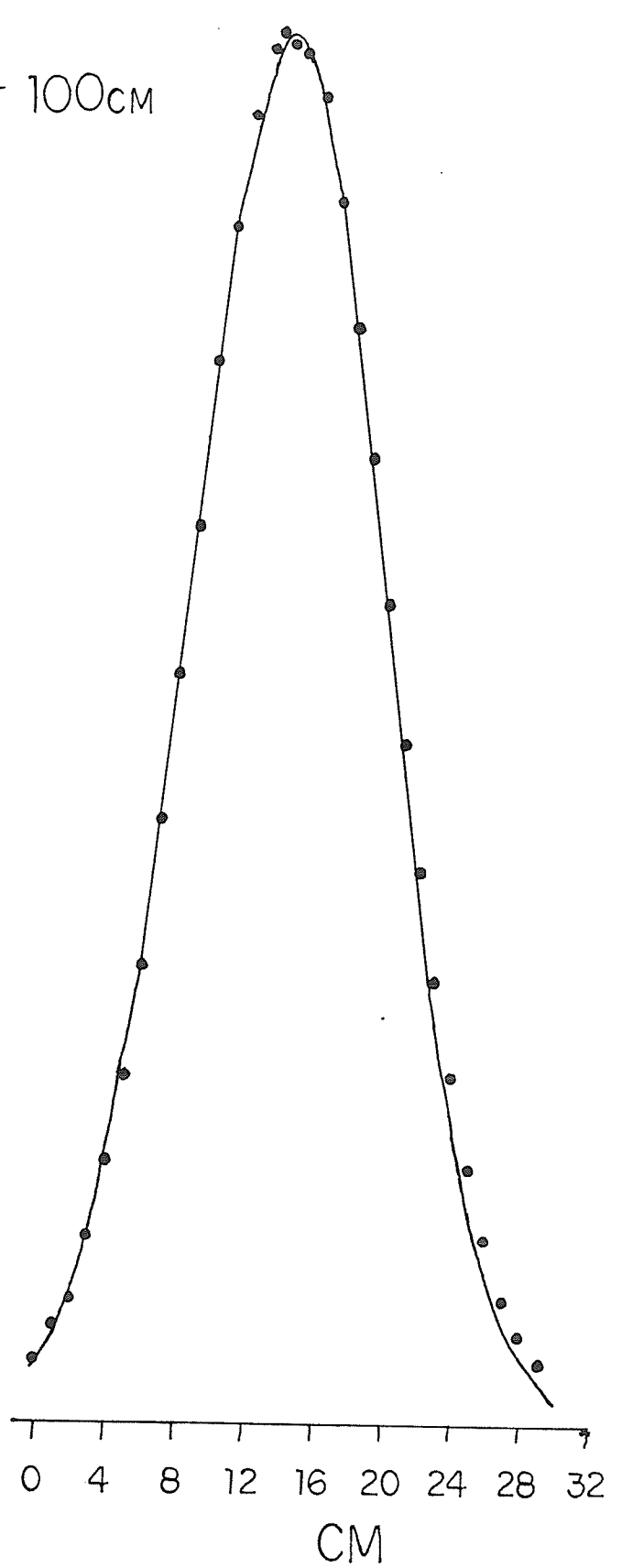
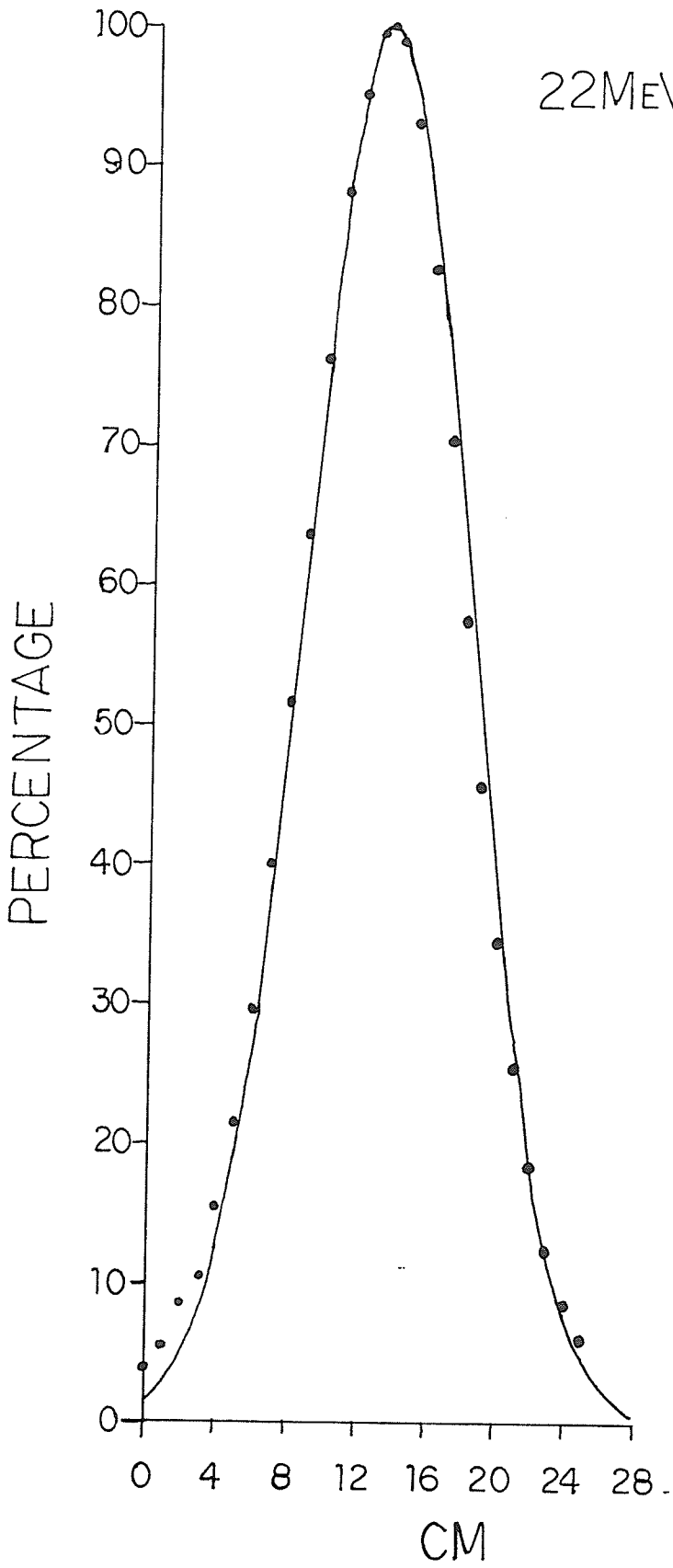
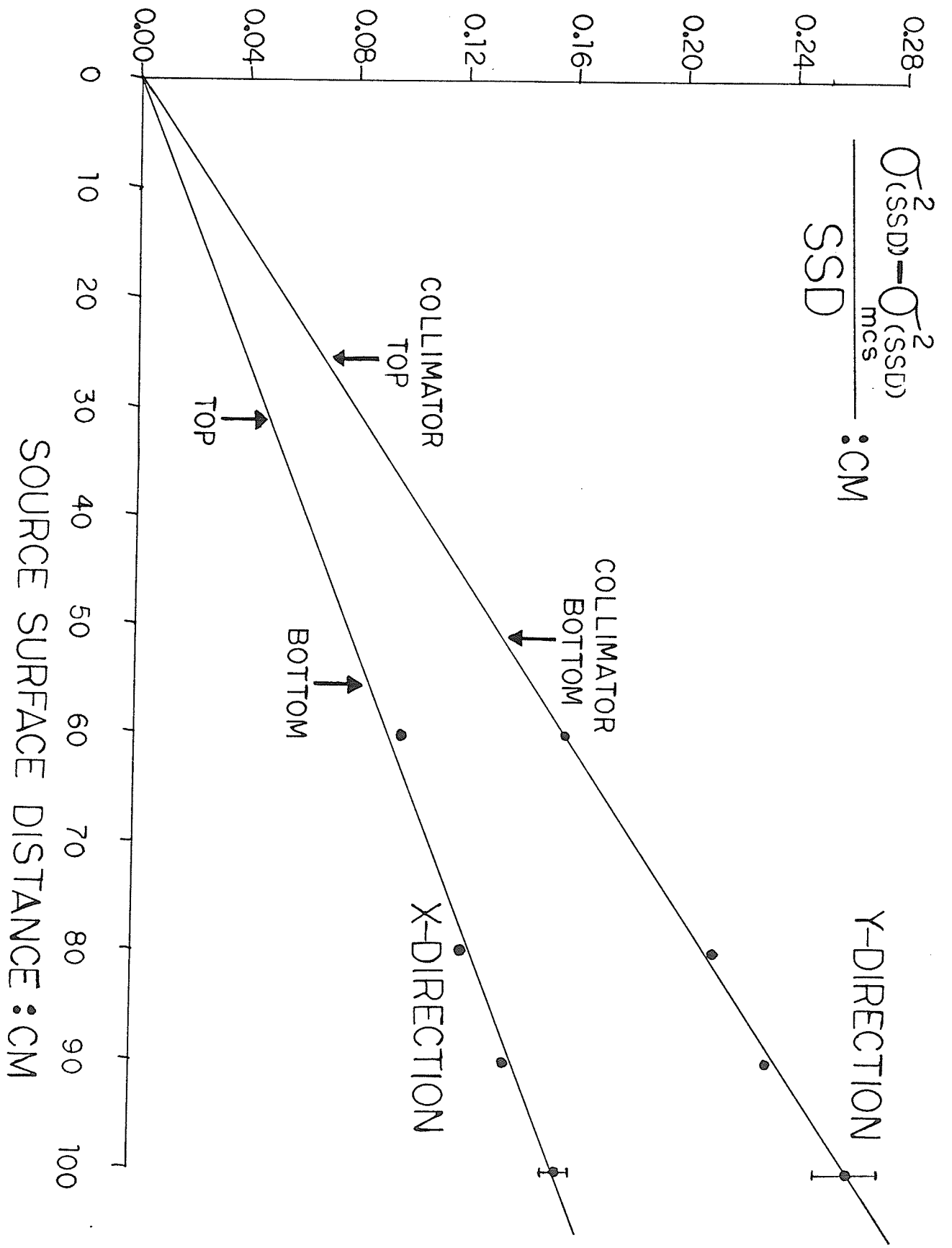


Figure 5.8: Fit of the variance for the Gaussian accelerator static electron beam in air with SSD to obtain the variance of the Gaussian initial angular distribution of an equivalent pencil beam.



pencil beam. The initial mean square angular spread $\overline{\theta_x^2}(0)$ is given by the measured data to be 1.552×10^{-3} radian² and 2.626×10^{-3} radian² in the x and y directions respectively. All further measurements that follow were performed using the magnetically scanned broad beam.

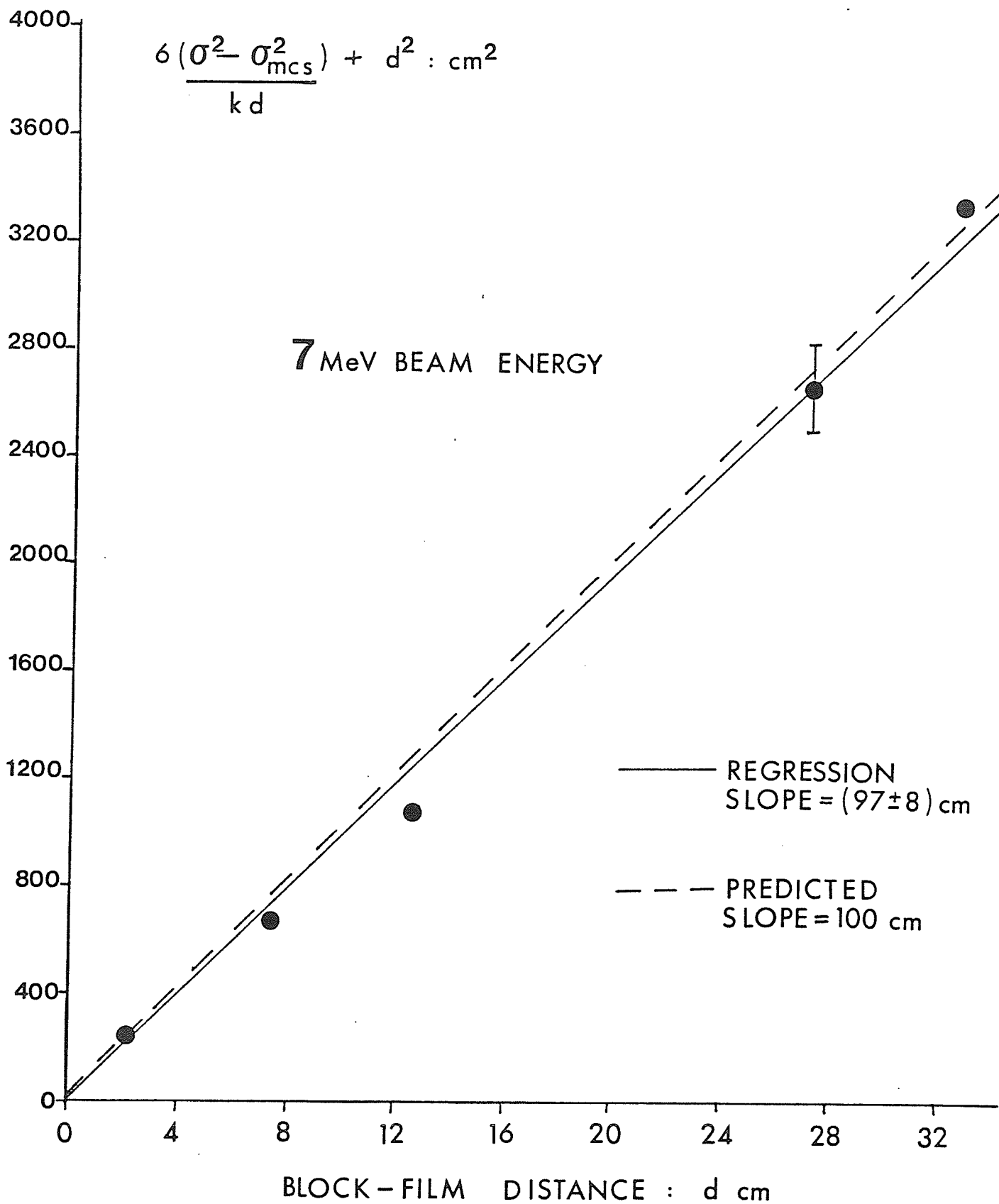
5.7.2 Verification of the Isotropic Point Source Location

Substitution of Equation 5.1 into Equation 5.3 and noting z' is equal to $z-d$ results (after some algebraic manipulation) in the equation

$$6(\sigma^2 - \sigma^2_{mcs})/kd + d^2 = zd$$

This equation suggests that measurement of the variation in penumbra width formed by a lead block edge, with distance d below the block may be used to verify that the source is located at the exit window of the accelerator. A 1.6 cm thick straight-edged lead block was positioned centrally to screen half a 20×20 cm² field defined at 100 cm SSD along a line parallel to the field edge. The block was moved along the central axis to various heights above a film placed at 100 cm SSD and the penumbra width formed on the film measured for a 7 MeV beam energy. The corresponding values of $\sigma(z)$ were derived from the penumbra width measurements using Equation A5.6. Figure 5.9 shows a plot of these data for $6(\sigma^2 - \sigma^2_{mcs})/kd + d^2$ versus d . A linear regression fit resulted in a straight

Figure 5.9: Determination of the isotropic source position.
The full line is a regression fit to the data
and the dashed line is predicted on the basis of
an isotropic source at the exit window of the
accelerator.



line of gradient equal to (97 ± 8) cm. This gradient is the experimentally determined source-film distance (z in Figure 5.2). The dashed line shown in Figure 5.9 is the gradient of 100 cm predicted for an isotropic source at the exit window of the accelerator. This shows that within experimental error the measured data locates the isotropic source at the exit window of the accelerator.

5.7.3 Penumbra Width Below Thick Lead Collimation

The data plotted in Figure 5.9 verified the assumption regarding the isotropic source location. However, implicit in the calculations is also the assumption that the 1.6 cm thick straight-edged block is equivalent to an infinitely thin plate located at a position corresponding to the centre of the block. It was therefore also necessary to investigate the validity of this implicit assumption by examining the variation of penumbra width formed below thick lead collimation with both collimator thickness and the angle the face of the collimator has with the central axis of the beam.

The variation of the penumbra width formed below large straight-edged lead blocks with increasing lead block thickness was measured for 7, 16 and 22 MeV beams on the central axis of a 20×20 cm² field defined at 100 cm SSD. The corresponding values of $\sigma(z)$ derived from

Equation A5.6 are plotted versus block thickness in Figure 5.10. For these measurements the lead blocks were positioned to screen half the field along a line parallel to the field edge with their lower surface located 25.6 cm above a film. This film was oriented perpendicular to the central axis of the beam at 100 cm SSD. The full lines in Figure 5.10 indicate theoretical predictions based on an isotropic source at the accelerator exit window and the treatment of the thick straight-edged lead blocks as an infinitely thin absorbing plate located at a position corresponding to the centre of the block. Under identical geometrical conditions the change in penumbra width below 5.1 cm thick lead blocks with the angle of the edge to the central axis of a 7 MeV beam was measured. Figure 5.11 shows the corresponding values of $\sigma(z)$ derived using Equation A5.6 versus angle of the block edge. The data of Figure 5.11 is compared to theoretical predictions (dashed lines) based on an isotropic source at the exit window and the treatment of the 5.1 cm thick angled block as an infinitely thin absorbing plate, located at one of three positions which correspond to the top, centre and bottom of the block.

5.7.4 Predictive Power and Limitations of Model for a Single Collimator

5.7.4.1 Lateral Position

In square fields defined by the double

Figure 5.10: Variation of $\sigma(z)$ derived from penumbra measured below a large straight edged block on the central axis of a $20 \times 20 \text{ cm}^2$ field with block thickness. Full lines show the theoretically predicted values.

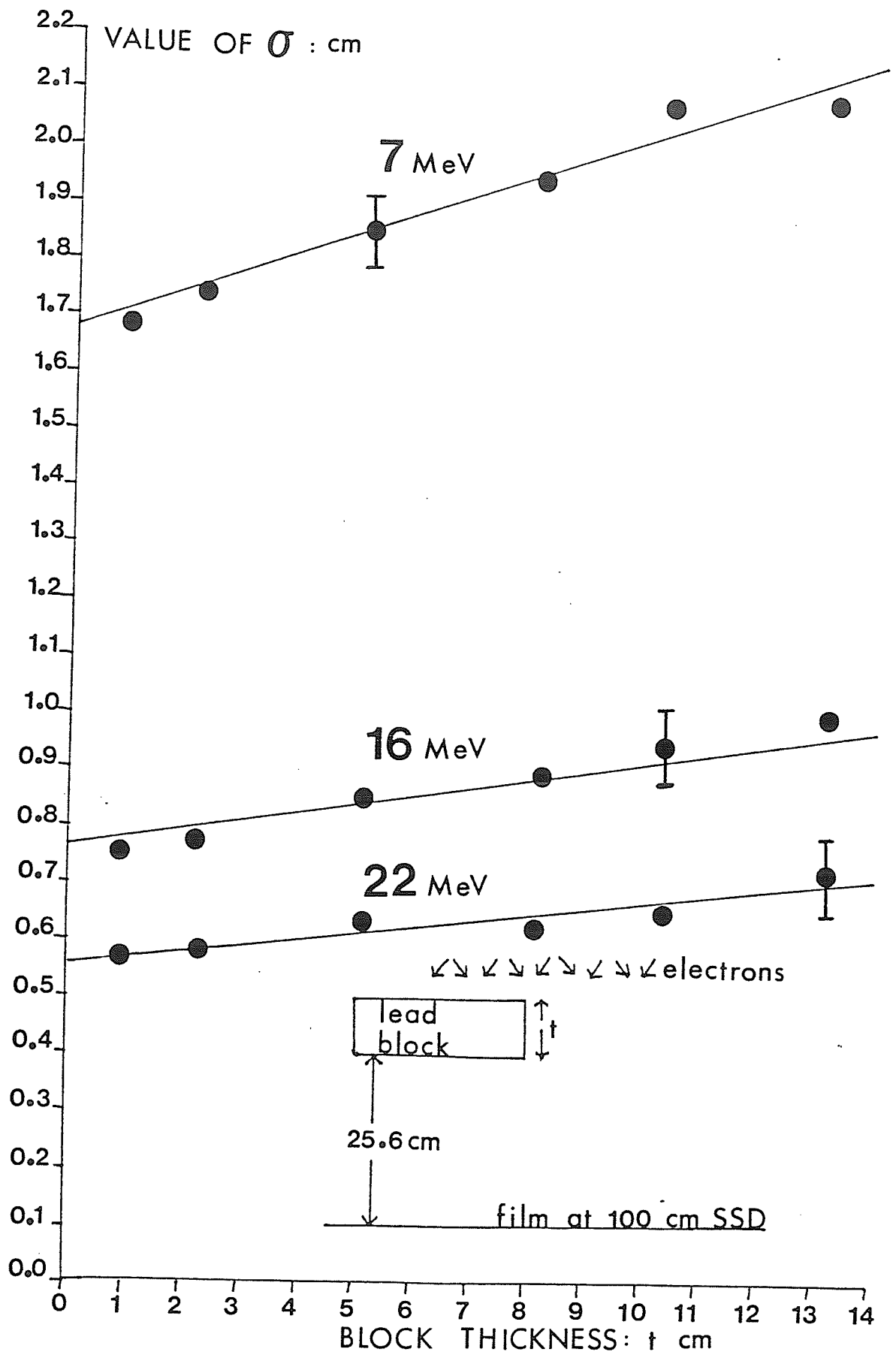
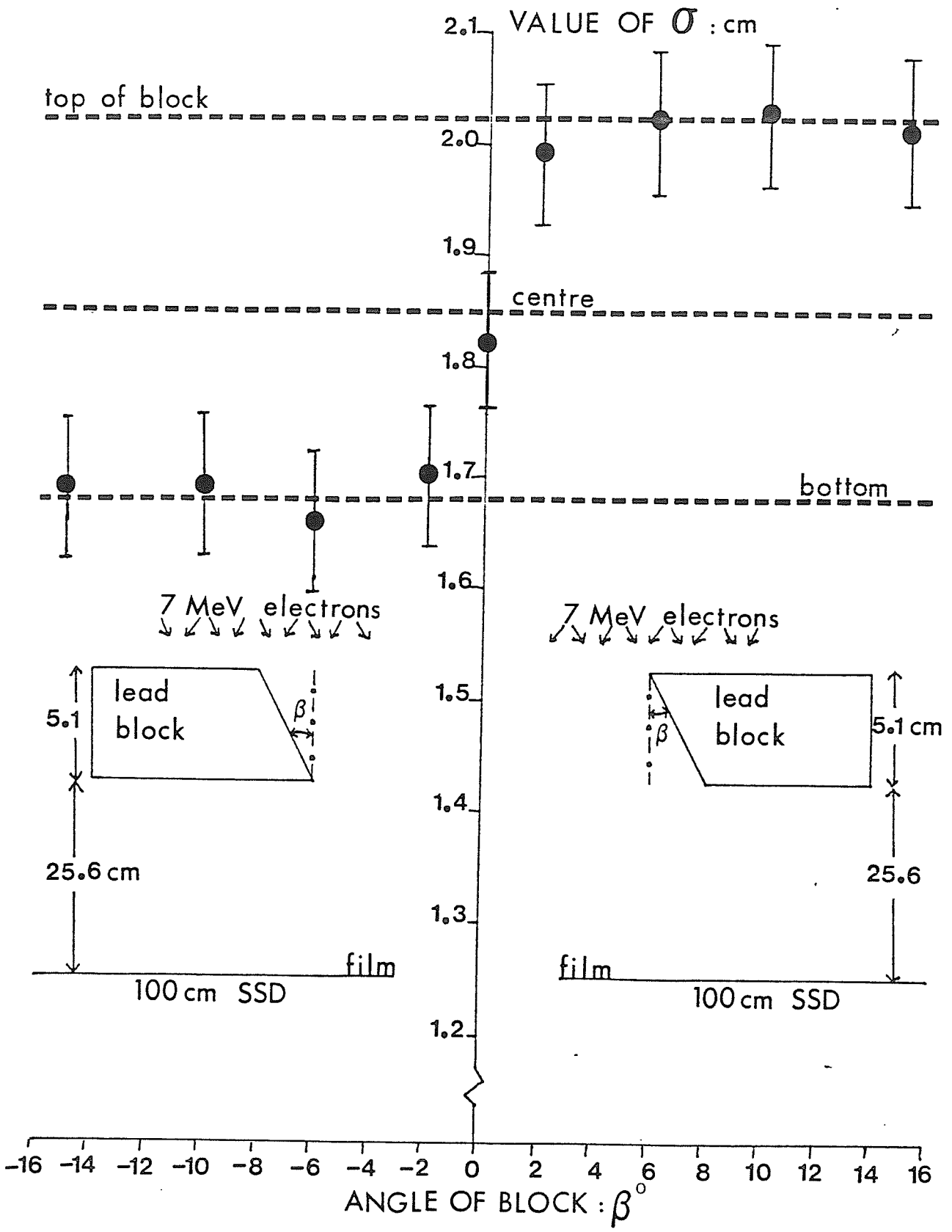


Figure 5.11: Variation of $\mathcal{O}(z)$ derived from penumbra measured below a 5.1 cm thick block on the central axis of a 20 x 20 cm² field with block angle for a 7 MeV beam.



collimator system, straight edged lead blocks were positioned with their lower surface 25.6 cm above a film placed at 100 cm SSD. The block edge was oriented along a line parallel to the field edge. This block was then shifted in a lateral direction to locations of increasing distance off the central axis until the field edge defined by the light field was reached. At each lateral location the penumbra width formed on a film placed below the block was measured. These measurements were repeated for 7, 10, 16 and 22 MeV beam energies in a square field of 20 x 20 cm² defined at 100 cm SSD and also for field sizes of 5 x 5 cm², 10 x 10 cm², and 15 x 15 cm² defined at 100 cm SSD for 7 and 22 MeV beam energies. The values of $\sigma(z)$ derived from Equation A5.6 using these penumbra width measurements are plotted versus lateral location in Figures 5.12 and 5.13. Theoretically predicted values of $\sigma(z)$ assume the thick block equivalent to an infinitely thin plate at its midpoint and are shown as full lines in Figures 5.12 and 5.13.

5.7.4.2 Beam Energy

The form of collimation most often used clinically is the trimmers. Each trimmer may be considered a single collimator which maintains a positive angle to the central axis of the therapy beam. The trimmers are there-

Figure 5.12: Variation of $\sigma(z)$ derived from penumbra measured below a thick block with distance of the block off the central axis for a $20 \times 20 \text{ cm}^2$ field (●) at 100 cm SSD and 7, 10, 16 and 22 MeV beam energies.

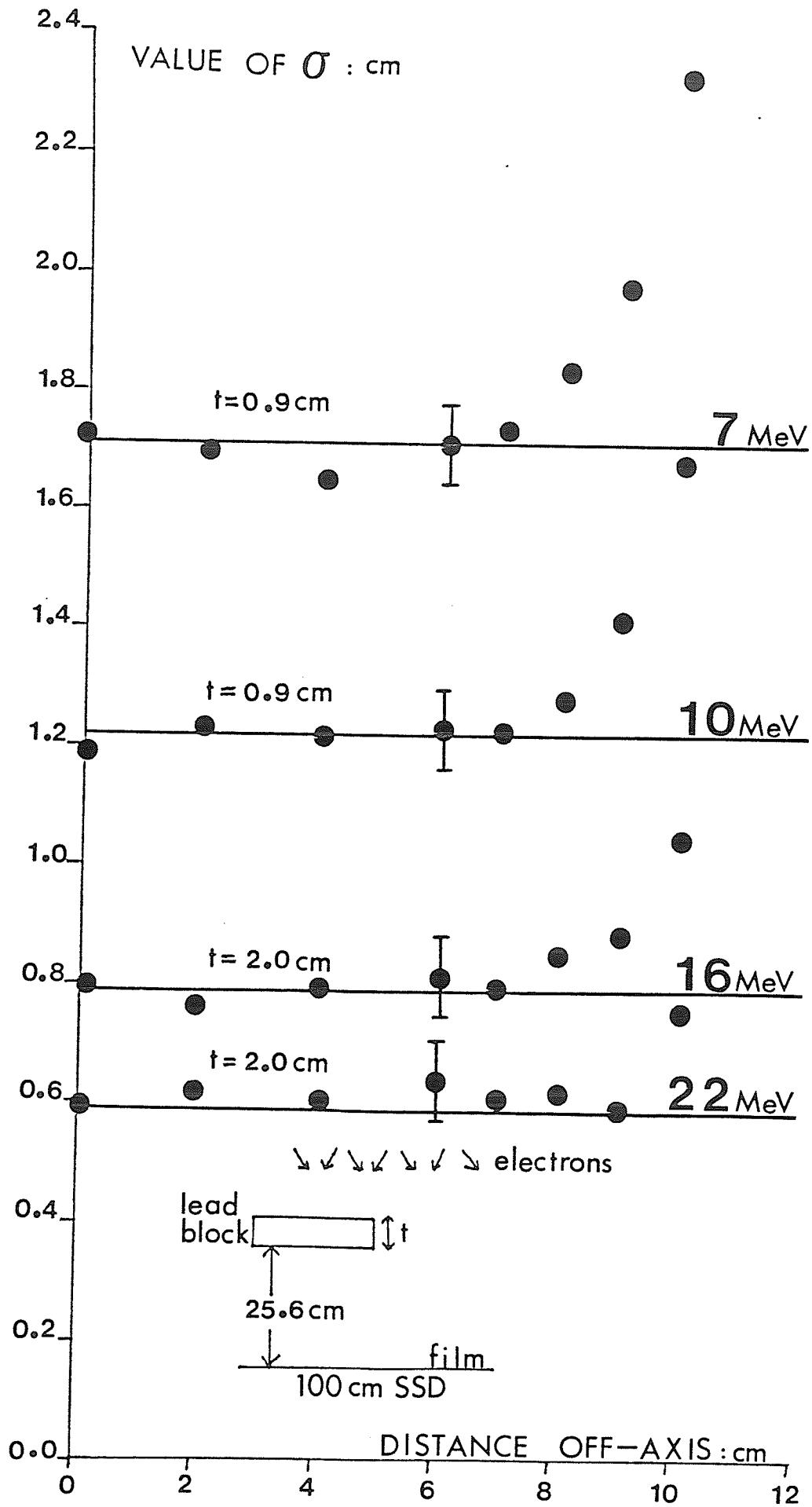
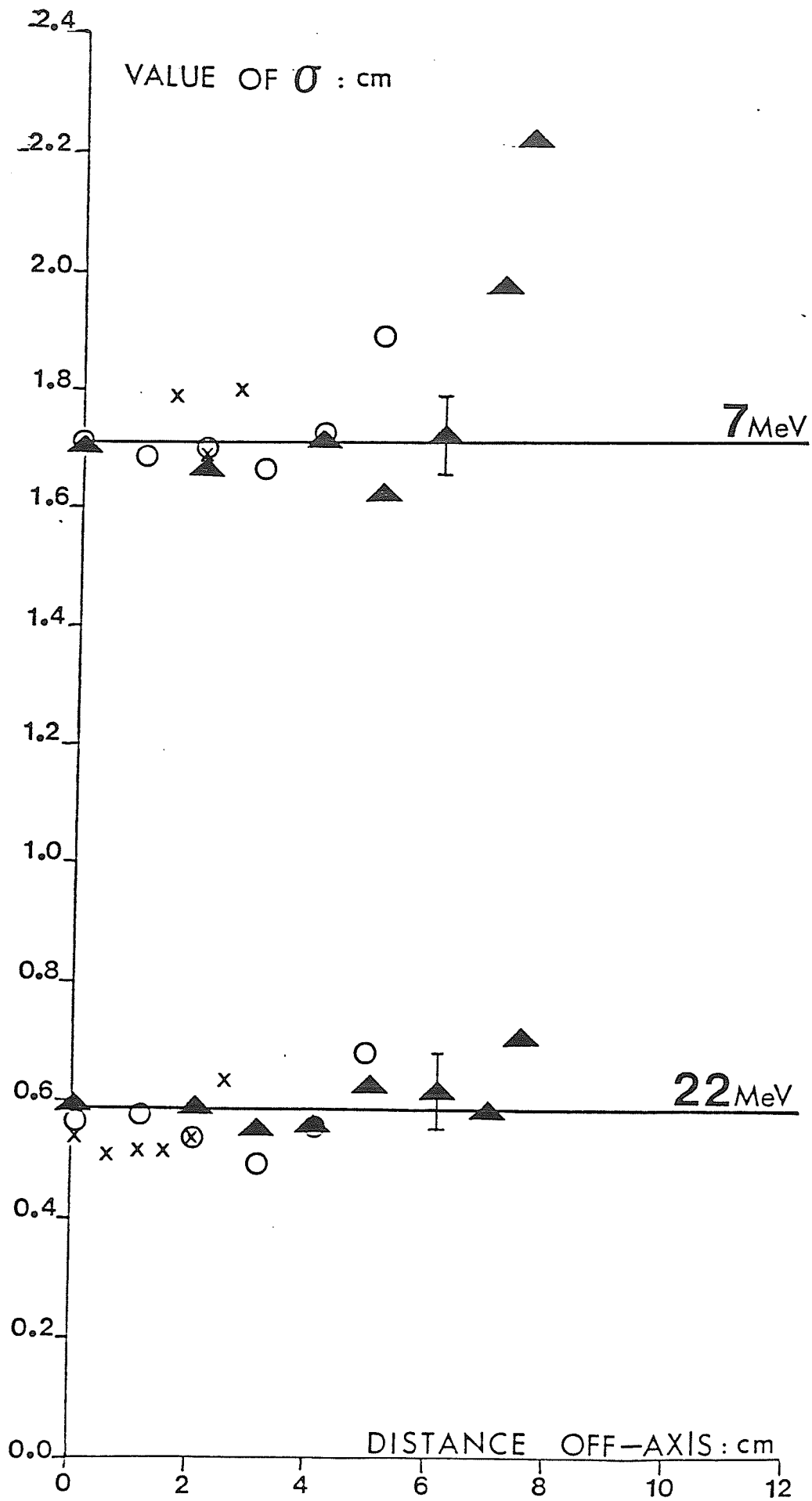


Figure 5.13: Variation of $\bar{O}(z)$ derived from penumbra measured below a thick block with distance of the block off the central axis for 15 x 15 cm² (▲), 10 x 10 cm² (○) and 5 x 5 cm² (×) at fields 100 cm SSD and 7 and 22 MeV beam energies.



fore modelled for the purposes of calculation by an infinitely thin absorbing plate located at a position corresponding to the top surface of the trimmer. The variation of penumbra width formed below the trimmers with beam energy was measured for 7, 16, 22 and 32 MeV beam energies in a 20 x 20 cm² field defined at 100 cm SSD. The corresponding values of $\sigma(z)$ computed using Equation A5.7 are plotted versus beam energy and compared to the theoretical values shown as a full curve in Figure 5.14.

5.7.4.3 Source-Surface Distance

Figure 5.15 shows the variation of $\sigma(z)$ with SSD for a 22 MeV beam and a square field size of 20 x 20 cm² defined at 100 cm SSD. The values of $\sigma(z)$ were derived from y-direction measurements of penumbra width formed below the trimmers and use of equation A5.7. The expected theoretical variation of $\sigma(z)$ based on the collimated isotropic source model is shown as the full curve in Figure 5.15.

5.7.4.4 Field Size

Measurements of the variation in penumbra width formed below the trimmers with field size were made at 100 cm SSD for a 22 MeV beam. The values of $\sigma(z)$ derived using Equation A5.7 are shown in Table 5.2 to be constant irrespective of

Figures 5.14: Variation of $\sigma(z)$ derived from penumbra measured below trimmer collimation at 100 cm SSD with beam energy. Full line shows the theoretically predicted values.

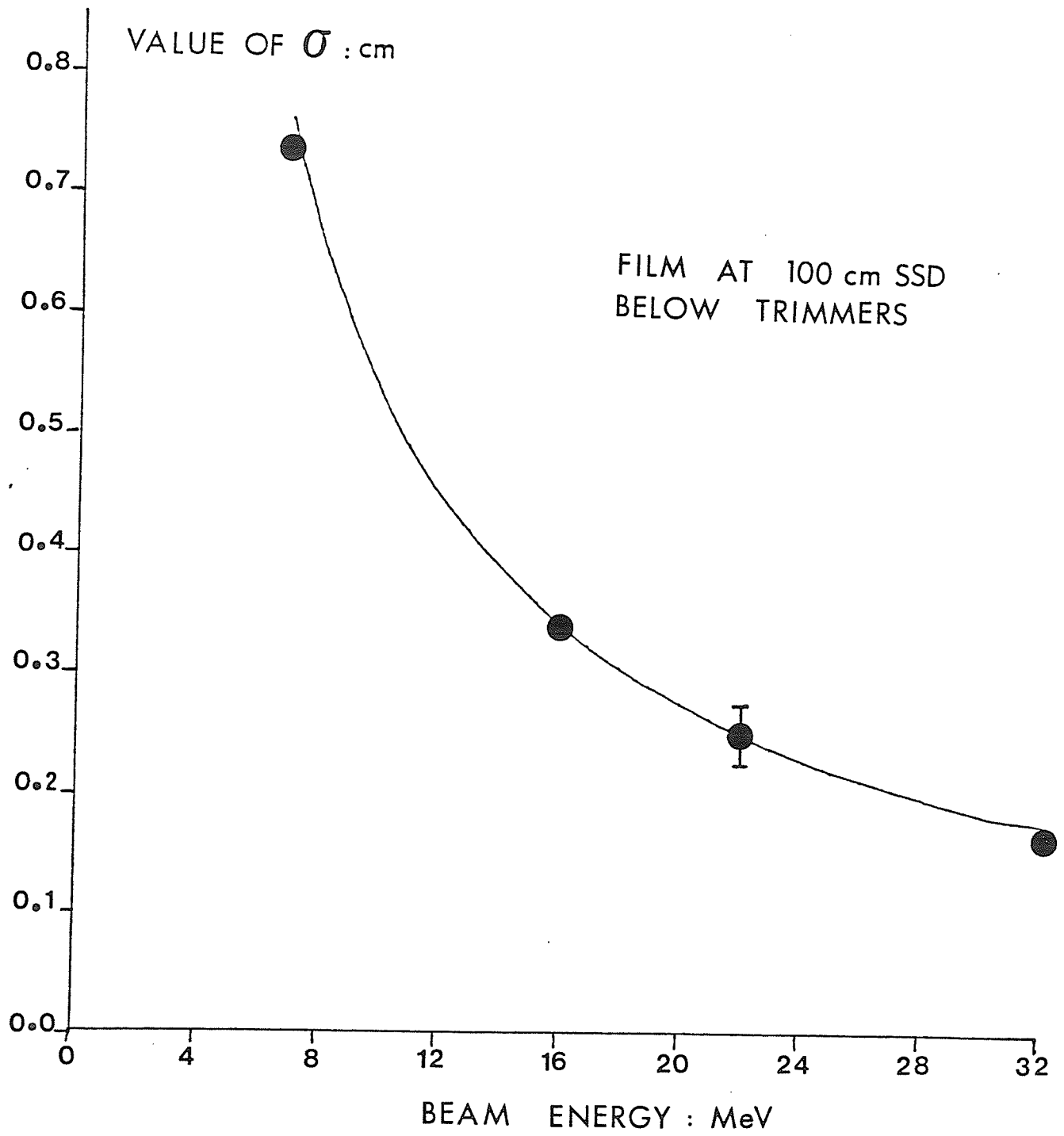


Figure 5.15: Variation of $\sigma(z)$ derived from penumbra measured below trimmer collimation with SSD for a 22 MeV beam energy. Full line shows the theoretically predicted values.

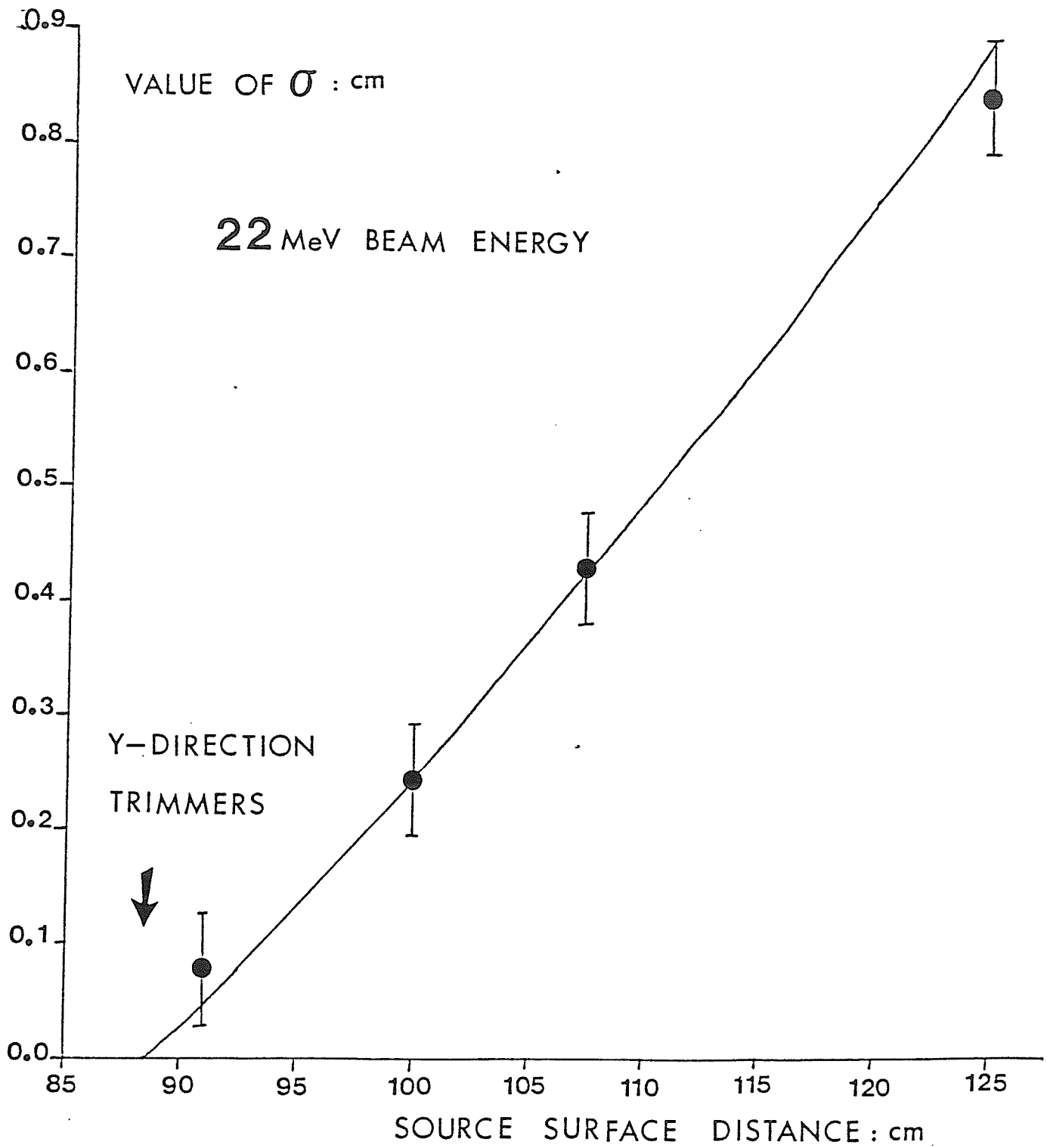


Table 5.2

Variation of $\sigma(z)$ derived from penumbra measured below trimmer collimation at 100 cm SSD with field size for a 22 MeV beam

FIELD SIZE (cm ²)	PREDICTED* $\sigma(z)$ (cm)	MEASURED $\sigma(z)$ (cm)
20 x 20	0.25	0.25 \pm 0.03
15 x 15	0.25	0.27 \pm 0.03
10 x 10	0.25	0.26 \pm 0.03
5 x 5	0.25	0.23 \pm 0.03
3 x 3	0.25	0.23 \pm 0.03

* $\sigma^2(z) = \bar{\sigma}_x^2 (88.5) + (11.5)^2 + \sigma_{mcs}^2 (11.5)$

field size setting, within the experimental error of this measurement. These results are in agreement with the data presented in Figures 5.12 and 5.13.

5.7.5 Predictive Power and Limitations of Model for a Double Collimator

5.7.5.1 Beam Energy

A method of collimating electron fields which is only occasionally adopted clinically is to use the photon collimators. These are conveniently labelled as a double collimator system, which implies two non-coplanar lead blocks are aligned such that both are responsible for penumbra formation. Measurements of the variation in penumbra width formed below the double collimator system were performed at 100 cm SSD for beam energies of 7, 16, 22 and 32 MeV. Table 5.3 shows the values of $\sigma(z)$ derived from y-direction beam profile penumbra width measurements for a 20 x 20 cm² field and the use of Equation A5.7. These measured values of $\sigma(z)$ are compared to the predicted values based on an isotropic source, and the lower collimator only of the double collimator system being responsible for penumbra formation. The lower collimator is

Table 5.3

Variation of $\sigma(z)$ derived from penumbra measured below double collimator system at 100 cm SSD with beam energy for a 20 x 20 cm² field defined at 100 cm SSD.

BEAM ENERGY (MeV)	PREDICTED* $\sigma(z)$ (cm)	MEASURED $\sigma(z)$ (cm)	PREDICTED + $\sigma(z)$ (cm)
7	3.81	3.66 \pm 0.05	3.66
16	1.73	1.66 \pm 0.05	1.66
22	1.27	1.22 \pm 0.05	1.22
32	0.86	0.80 \pm 0.03	0.83

$$* \sigma^2(z) = \bar{\theta}_x^2 (42) \cdot 58^2 + \sigma^2_{mcs}(58)$$

$$+ \sigma^2(z) = f\bar{\theta}_x^2 (42) \cdot 58^2 + \sigma^2_{mcs}(58)$$

Where f is a perturbation factor of 0.82 due to the presence of the photon collimator closest to the source.

considered equivalent to an infinitely thin absorbing plate located at a position corresponding to the top surface of the collimator. Inspection of the measured and predicted data sets reveals a significant discrepancy between them. This implies that the upper collimator in the double collimator system causes a perturbation of the electron field at the lower collimator. Assuming this perturbation effect alters the mean square angle of travel of the electrons at the lower collimator from the value predicted on the central axis of the beam, we introduce an empirical perturbation factor f into the formalism. The fourth column of Table 5.3 uses a multiplicative perturbation factor of 0.82 to reduce the predicted value of the mean square angle of travel of the electrons at the lower collimator. This factor of 0.82 was chosen to give good agreement with the measured data at 16 MeV. Surprisingly, this simple modification of the formalism is appropriate for all beam energies at this field size setting.

5.7.5.2 Source Surface Distance

Measurement of the variation in penumbra

width formed below the double collimator system with SSD was performed for a 22 MeV beam energy at a field size setting of 20 x 20 cm² defined for 100 cm SSD. Table 5.4 shows the measured values of $\sigma(z)$ derived from the y-direction beam profile penumbra width measurements and the use of Equation A5.7. The theoretical values of $\sigma(z)$ are computed on the basis of an isotropic source with only the lower collimator of the system assumed responsible for penumbra formation. Comparison of the measured and predicted data sets reveal that the measured values of $\sigma(z)$ are consistently overestimated by the predicted values. Implementing the use of the same 0.82 multiplicative perturbation factor f , for the mean square angle of travel of the electrons at the lower collimator in the double collimator system, produces a slight improvement in the agreement of predicted $\sigma(z)$ values with the measured data (Table 5.4).

5.7.5.3 Field Size

Measurements of the variation in penumbra width with field size below the double collimator system were performed for 7, 16, 22 and 32

Table 5.4

Variation of $\sigma(z)$ derived from penumbra measured below photon collimation with SSD for a 20 x 20 cm² field defined at 100 cm SSD

SSD (cm)	d (cm)	PREDICTED* $\sigma(z)$ (cm)	MEASURED $\sigma(z)$ (cm)	PREDICTED + $\sigma(z)$ (cm)
60	18	0.30	0.23 ± 0.03	0.28
70	28	0.51	0.44 ± 0.03	0.48
80	38	0.74	0.70 ± 0.03	0.71
90	47	0.97	0.94 ± 0.04	0.93
100	58	1.27	1.22 ± 0.04	1.22
107.4	65.4	1.48	1.44 ± 0.05	1.43

$$* \sigma^2(z) = \overline{\theta_x^2} (42) \cdot 58^2 + \sigma_{mcs}^2(58)$$

$$+ \sigma^2(z) = f\overline{\theta_x^2} (42) \cdot 58^2 + \sigma_{mcs}^2(58)$$

Where f is a perturbation factor of 0.82 due to the presence of the photon collimator closest to the source.

MeV beam energies. The penumbra width was measured at 100 cm SSD in the y-direction for square field sizes in the range 20 x 20 cm² to 3 x 3 cm². The measured values of $\bar{\sigma}(z)$ derived using Equation A5.7 are plotted in Figure 5.16 versus length of square field. There is a definite variation of the measured values of $\bar{\sigma}(z)$ with field size. This variation contrasts with the single collimator case where the measured values of $\bar{\sigma}(z)$ are constant with field size setting (Table 5.2). This variation with field size indicates that the empirical perturbation factor introduced into the formalism must be determined at each field size setting. The perturbation factor f determined for a 16 MeV beam at 100 cm SSD and square field sizes in the range 3 x 3 cm² to 20 x 20 cm² may be used to predict values of $\bar{\sigma}(z)$ at other beam energies and SSD. These perturbation factors are given in Table 5.5.

5.7.6 Predictive power and Limitations of Model for Beam Output and Profile FWHM

5.7.6.1 Output for Fixed Field Size

The effects of lateral scatter dise-

Figure 5.16: Variation of $\sigma'(z)$ derived from penumbra measured below photon collimation at 100 cm SSD with field size for 7, 16, 22 and 32 MeV beam energies. Dotted lines act as a guide to the eye.

VALUE OF σ : cm

7 MeV

DOUBLE (PHOTON) COLLIMATORS

16 MeV

22 MeV

32 MeV

LENGTH OF SQUARE FIELD : cm

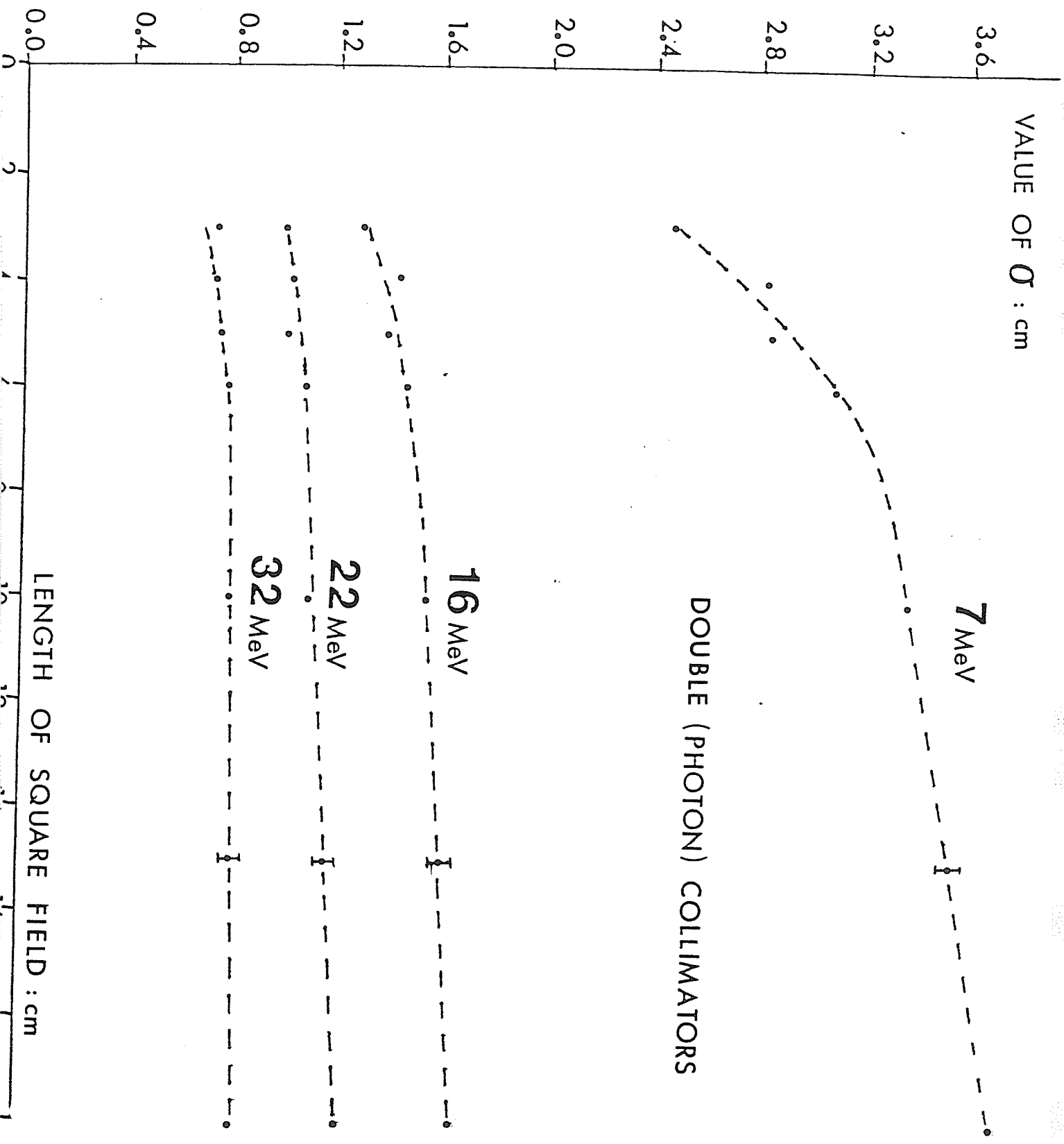


Table 5.5

Variation of empirical perturbation factors
f with field size setting of the double
collimator system

Field Size at 100 cm SSD (cm ²)	Perturbation Factor f
20 x 20	0.82
15 x 15	0.65
10 x 10	0.49
6 x 6	0.29
5 x 5	0.21
4 x 4	0.14
3 x 3	0.00

quilibrium on beam output were investigated by fixing the field size setting. Measurement of the variation in ionization along the central axis of a 6 cm x 6 cm square field with SSD for beam energies of 7, 16, 22 and 32 MeV are compared in Figure 5.17 to the inverse square law shown as a dashed curve and the predicted variation using Equation 5.6 shown as full lines. The ionization values measured with SSD are normalized to the value obtained at 100 cm SSD for all the results quoted in this subsection. The variation in ionization along the central axis of a 7 MeV beam with SSD for square field sizes of 5 cm x 5 cm, 10 cm x 10 cm and 15 cm x 15 cm are compared in Figure 5.18 also to the inverse square law and the predicted variation using Equation 5.6. Similarly, these measurements were repeated for a 10 MeV beam energy and the results are shown in Figure 5.19.

5.7.6.2 Output for Variable Field Size

The radiation output factor in air at 100 cm SSD was measured without trimmer collimation for field sizes in the range 4 cm x 4 cm to 36 cm x 36 cm at electron beam energies of 7, 10, 22 and

Figure 5.17: Variation of Ionization with source chamber distance for a 6 cm x 6 cm field at beam energies of 7, 16, 22 and 32 MeV.

IONISATION RATIO

6cm x 6cm FIELD

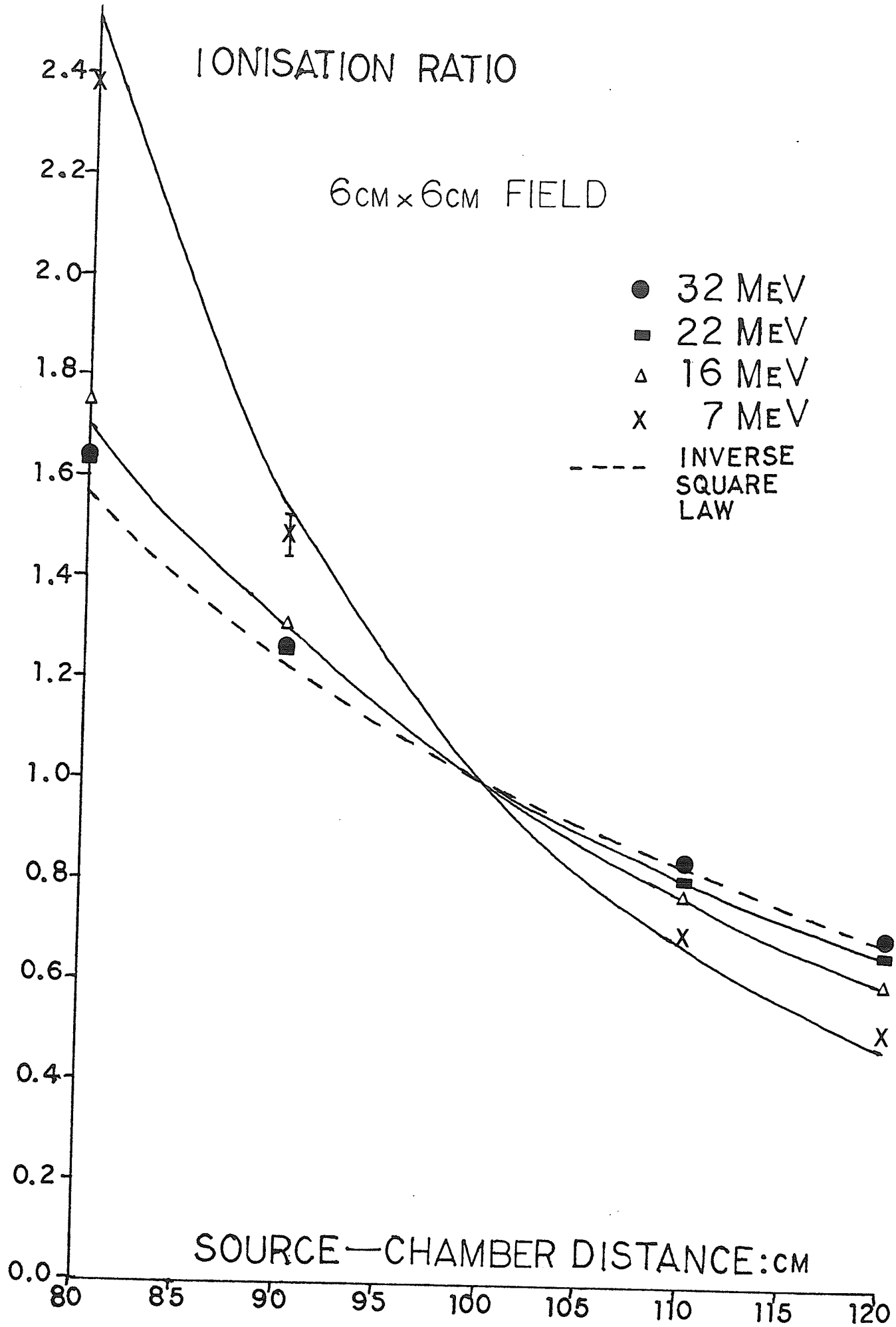


Figure 5.18: Variation of Ionization with SCD for a 7 MeV beam energy at square field sizes of 5 cm x 5 cm, 10 cm x 10 cm and 15 cm x 15 cm.

IONISATION RATIO

7 MEV

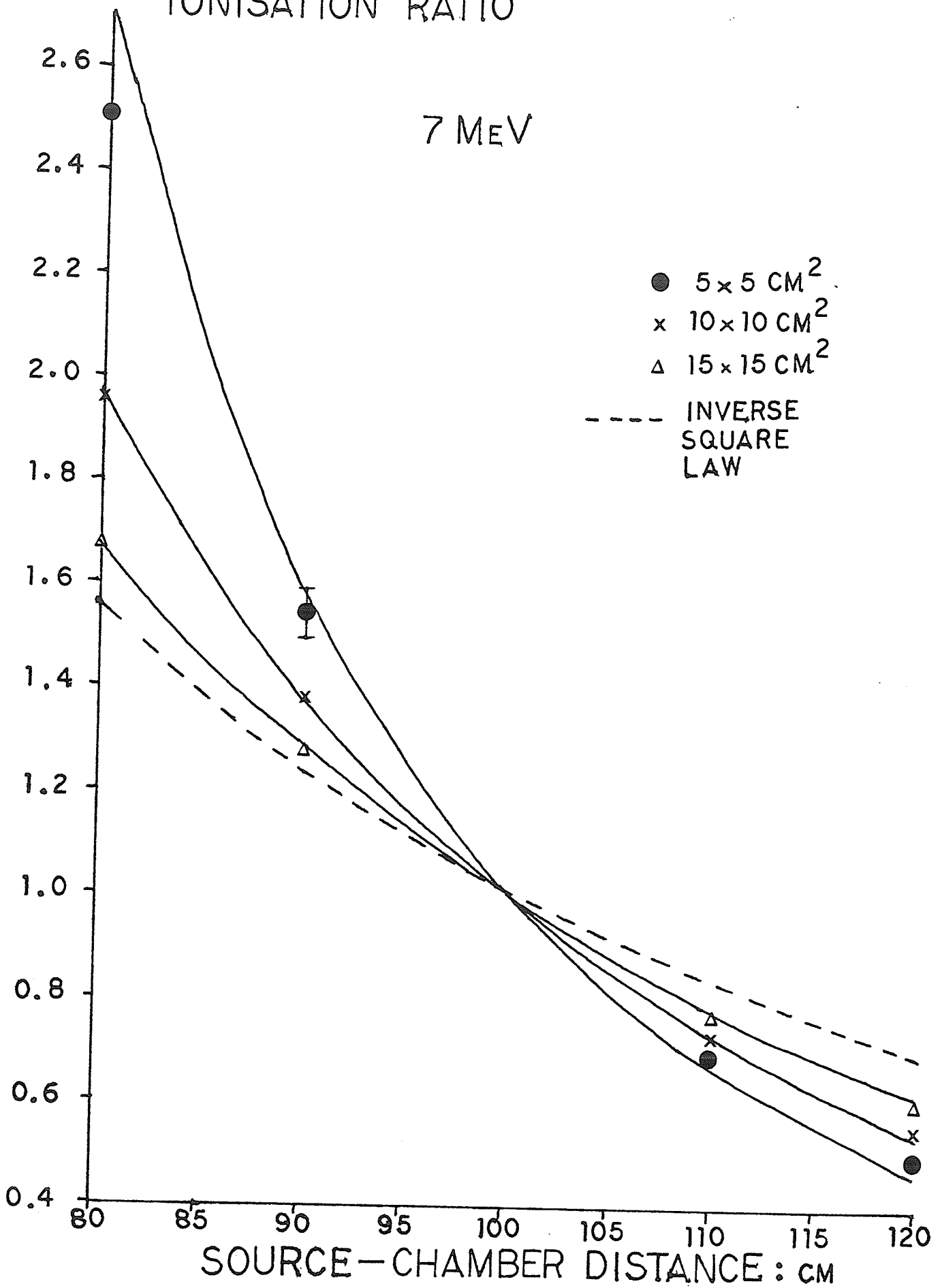
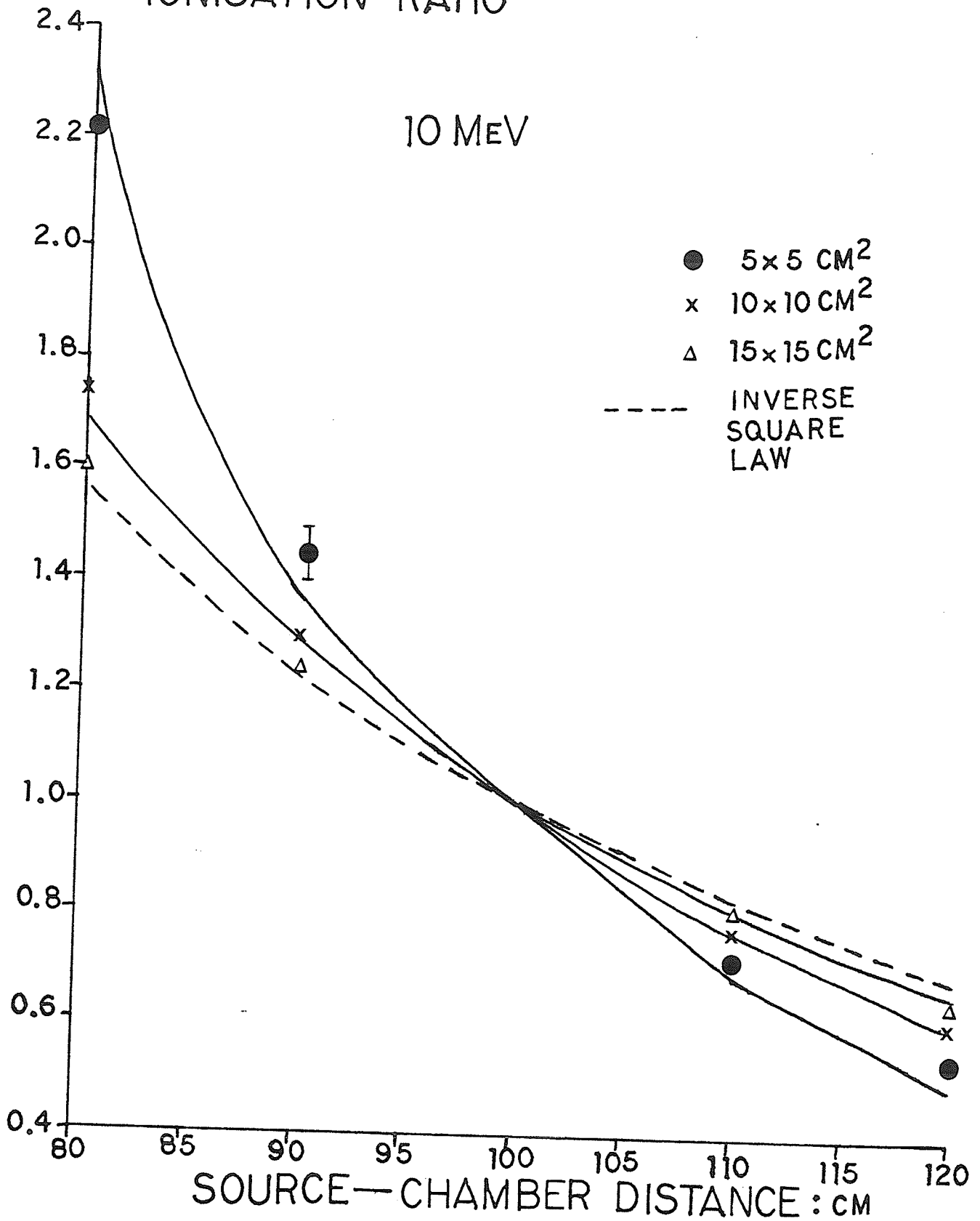


Figure 5.19: Variation of Ionization with SCD for a 10 MeV beam energy at square field sizes of 5 cm x 5 cm, 10 cm x 10 cm and 15 cm x 15 cm.

IONISATION RATIO

10 MEV



32 MeV. The results shown in Figure 5.20 demonstrate that the reduction in output with decreasing square field size is strongly dependent on beam energy. Figure 5.21 reproduces the variation in radiation output factor for the 7 and 32 MeV beam energies and compares them to the theoretically predicted variation computed using Equation 5.6. The theoretically predicted curves shown as dashed lines in Figure 5.21 account only for lateral scatter disequilibrium effects. The differences between the measured and predicted curves in this figure are probably due to the effects of backscattering from collimators to the monitor chamber.

5.7.6.3 Beam Profile FWHM

A further effect of lateral scatter disequilibrium is to increase the full width at half maximum (FWHM) of a normalized beam profile above that predicted on purely geometrical grounds. Table 5.6 presents measurements of beam profile FWHM at 100 cm SSD for square fields formed by the photon collimators. The field size is set according to the light field measurements and is varied over the range 3 cm x 3 cm to 20 cm

Figure 5.20: Variation in output at 100 cm source chamber distance with field size for beam energies of 7 MeV (●), 10 MeV (✂), 22 MeV (X) and 32 MeV (■). Field is defined by the photon collimators.

IONISATION RATIO

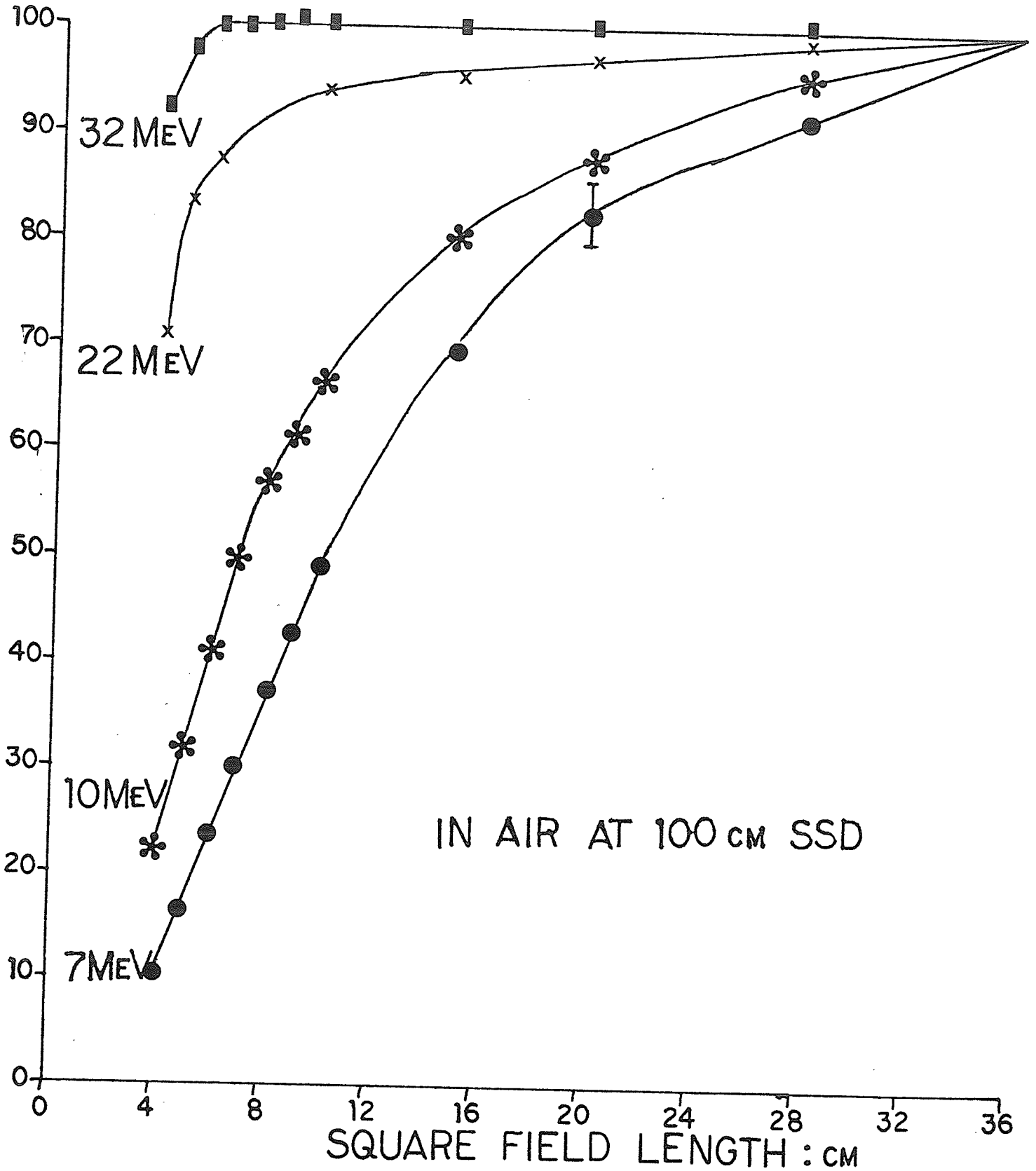


Figure 5.21: Variation in output at 100 cm SCD with field size for beam energies of 7 MeV (●) and 32 MeV (■). Theoretically predicted curves shown dashed.

IONISATION RATIO

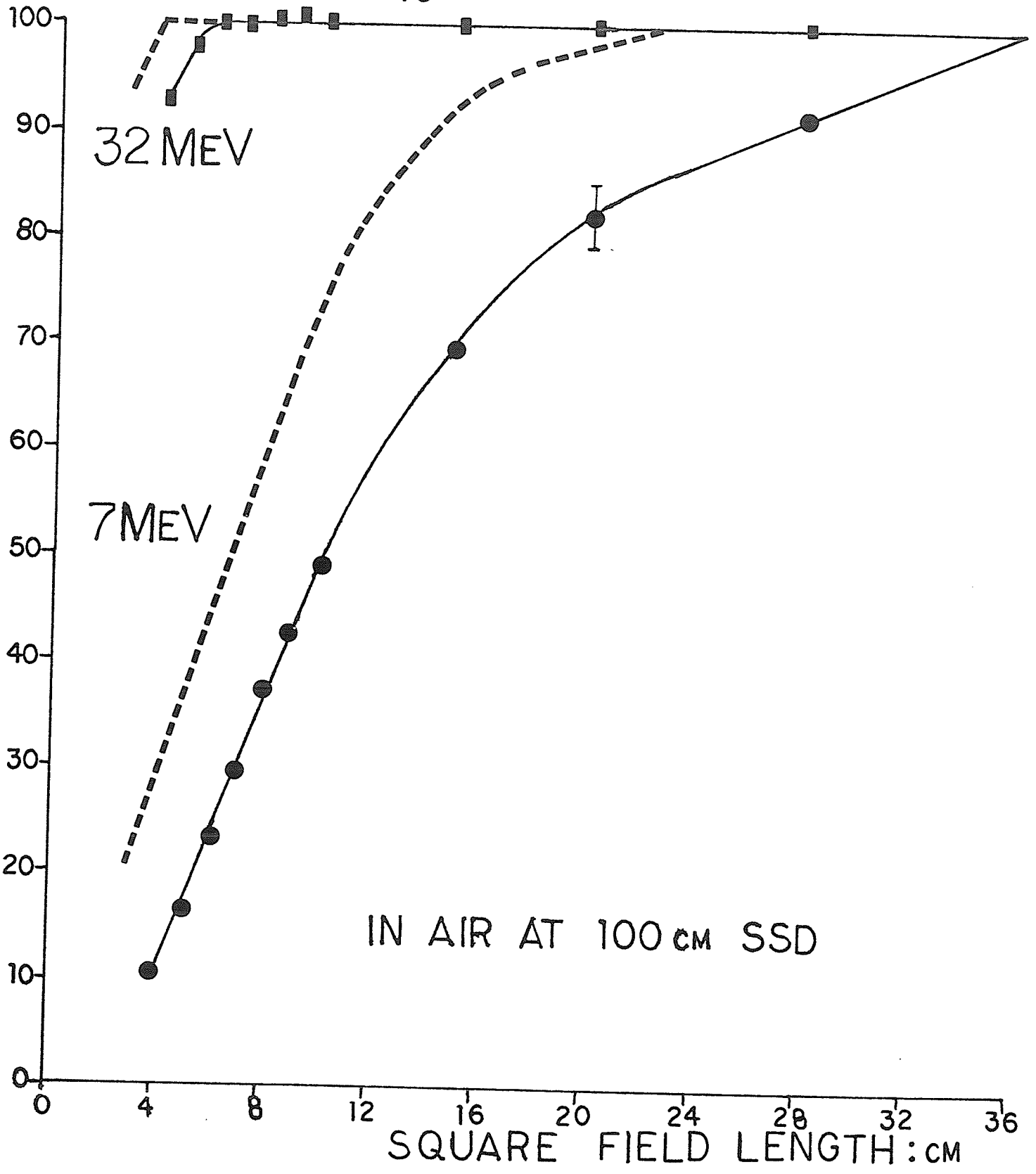


Table 5.6
 Comparison of measured values of FWHM with predicted
 values for y-direction beam profiles

Field Size (cm ²) at 100 cm SSD	Electron Energy:MeV							
	7		16		22		32	
	M	P	M	P	M	P	M	P
20 x 20	20.1	20.1	20.0		20.0		20.0	
15 x 15	15.3	15.3	15.0		15.0		15.0	
10 x 10	10.9	11.1	10.0		10.0		10.0	
6 x 6	8.4	8.5	6.2	6.1	6.0		6.0	
5 x 5	7.7	7.6	5.3	5.3	5.0	5.0	5.0	
4 x 4	7.1	7.0	4.5	4.5	4.1	4.1	4.0	
3 x 3	6.6	6.2	3.8	3.8	3.3	3.3	3.1	3.0

M = Measured (cm); P = Predicted (cm)

x 20 cm for beam energies of 7, 16, 22 and 32 MeV. Notice that at the smallest energy and field size the measured FWHM of the normalized beam profile is over twice as large as would be expected based on the geometrical set-up. Table 5.6 also compares the measured data to the FWHM of the beams predicted using Equation 5.8. The values of $\sigma(z)$ used in this equation are taken from the measured profiles. Therefore the predicted FWHM results only give a test of self-consistency since the values of $\sigma(z)$ are derived from the same basic equation.

5.8 Discussion

The Liouville Theorem which governs the phase-space transport of electrons in linear accelerators (Banford 1966) predicts an elliptical shape of the static accelerator beam upon emerging from the accelerator exit window. The beam profiles in air at each SSD investigated are closely fit by Gaussian shaped curves in both the x and y directions. A typical example is shown in Figure 5.7 for the beam profiles at 100 cm SSD at a 22 MeV energy. Figure 5.8 shows that the variation in spatial spread of the static accelerator beam with SSD may be approximated by a pencil beam of electrons at the exit window of the accelerator which has an initial Gaussian angular distribution.

However, the initial mean square angular spread $\overline{\theta_x^2}(0)$, measured by the gradient of the straight line plots in Figure 5.8, is different in the x and y directions. Representing the static beams as a point source has several important implications, the first of which is that the finite size of the beam (3.5 mm x 1.5 mm) at the accelerator exit window may be considered negligible.

Secondly, the scattering effect of the monitor chamber on the static beam may be approximated at large distances downstream by simply assuming the chamber to cause an additional initial angular divergence to the pencil beam source over the true initial angular divergence. Consequently, this implies that as the static beam is scanned over large angles, the effect of the monitor chamber can be ignored at large distances downstream since the initial divergence of the equivalent pencil beam is overwhelmed by the scanning action. Therefore the therapeutic scanned electron beams may be modelled by a collimated isotropic source located at the exit window of the accelerator. If this approximation is bad, the scattering effect of the monitor chamber would be expected to shift the location of the isotropic electron source as derived using Equation 5.3, from the accelerator exit window. Figure 5.9 shows that a linear regression fit to the data went through the origin and gave the source-film distance as $(97 \pm 8 \text{ cm})$. Because the true source-film distance is 100 cm, this result suggests that approximating the static accelerator

beam plus chamber as equivalent to a pencil beam with an initial Gaussian angular distribution is remarkably good. The finding that the isotropic source can be considered located at the accelerator exit window and the scattering effect of the monitor chamber can be ignored, provides a simple but powerful model of the accelerator which may be used to compute the theoretical values of $\sigma(z)$ for use in Equation 5.2 and hence predict the shape of beam profiles.

The formalism used for the plot in Figure 5.9 assumed that the 1.6 cm thick straight-edged lead block was equivalent to an infinitely thin absorbing plate located at a position corresponding to the centre of the thick block. Figure 5.10 shows the variation of $\sigma(z)$ derived from the penumbra width formed below straight-edged lead blocks with lead block thickness for 7, 16 and 22 MeV beams. These data are compared to the theoretical predictions (full lines in Figure 5.10) computed from Equation 5.3 on the basis of an isotropic source at the exit window and treatment of the block as equivalent to an infinitely thin absorbing plate located at a position corresponding to the centre of the block. The agreement between the predicted and measured data is excellent. This agreement verifies that thick blocks may be considered infinitely thin when predicting penumbra shape and suggests that the gain or loss of electrons from the field due to interactions with the block, have negligible effect on the for-

mation of penumbra in air at distances beyond the block greater than a few centimeters.

Although thick collimation or blocks may be considered equivalent to an infinitely thin absorbing plate, the position at which the plate is located in the field depends upon the angle of the block, as shown in Figure 5.11. For blocks which make positive angles with the central axis, the equivalent infinitely thin absorbing plate may be considered located at a position corresponding to the surface of the thick lead block closest to the source. However, for blocks which make negative angles with the central axis the equivalent infinitely thin absorbing plate must be considered located at a position corresponding to the surface of the thick lead block furthest from the source.

The good agreement between the values of $\sigma(z)$ predicted using Equation 5.3 and the measured values plotted in Figure 5.10 and 5.11, suggest that modelling the accelerator electron beam by an isotropic source and the collimation as infinitely thin absorbing plates is valid for central axis measurements in large fields. The predictive power of this model was initially tested for field edges defined by a single collimator. To establish the validity of the model at locations off the central axis and for variations of field size, $\sigma(z)$ derived from penumbra width formed below a single collimator was measured across square field sizes of 5 x 5, 10 x 10, 15 x 15 and 20 x 20 cm² for beam

energies of 7 and 22 MeV and across a 20 x 20 cm² field for beam energies of 10 and 16 MeV. Figures 5.12 and 5.13 show that for all the energies investigated, the value of $\sigma(z)$ derived from penumbra width for a given energy is constant within experimental error for the central region of the therapeutic beam, irrespective of field size. These values are consistent with the theoretically predicted values for an isotropic point source located at the exit window, which are shown as full lines in both Figures 5.12 and 5.13. However, as the single collimator moves laterally into the region close to the field edge defined by the double collimator system, the value of $\sigma(z)$ derived from penumbra width measurements rise above the predicted value. The lateral extent of this anomolous region of increased $\sigma(z)$ value appears constant with energy (Figure 5.12) and is seen from the 7 MeV data to decrease with field size (Figure 5.13).

The reason for the discrepancies between predicted and measured values of $\sigma(z)$ in this region is unclear. It may be due, in part, to the single collimator entering the penumbra region of the field formed by the double collimator system. The electron fluence beyond the double collimator system in the penumbra region decreases rapidly. This violates an assumption implicit in the derivation of Equation A5.6 that the fluence across the field at the level of the single collimator is constant.

The predictive power in air of assuming an isotropic point source at the exit window and assuming thick lead collimation equivalent to an infinitely thin absorbing plate located at the top surface of the collimator is excellent for predicting the shape of fields formed by the trimmer collimation. This is because the positively angled trimmers lie about 4 cm inside the field formed by the double collimator system and therefore the region of anomalous $\sigma(z)$ values described previously is fortunately avoided. Figure 5.14 shows the excellent agreement between theoretical variation of $\sigma(z)$ with beam energy derived using Equation 5.3 (full curve) and the measured values of $\sigma(z)$ derived from penumbra width for 7, 16, 22 and 32 MeV beam energies. This excellent agreement is maintained between the measured and predicted values of $\sigma(z)$ with a variation in source surface distance as demonstrated in Figure 5.15 for a 22 MeV beam energy. Also, the value of $\sigma(z)$ measured below the trimmers is constant irrespective of field size setting, as predicted according to theory. This is shown in Table 5.2 for a 22 MeV beam energy and the conclusion is supported for other beam energies by the data of Figures 5.12 and 5.13.

In most clinical situations trimmer collimation or a single "lead cut-out" collimator of irregular shape is used. The collimated isotropic source model is simple and able to make excellent predictions of beam profile shape in these clinical situations

without the requirement of any empirical input data. Although only rectangular field data has been compared to the theory, it is expected that the agreement between theoretical and measured data for irregular field shapes will remain excellent.

When a double collimation system is used to form a beam edge some modelling difficulties arise. The upper collimator of the double collimation system restricts the field size and forms a penumbra. In the penumbra region, the mean square angle of travel of the electrons continuously falls below the value expected on the central axis of the beam (see Chapter 4 section 5). Since the lower collimator of the double collimation system lies within the penumbra region, the measured values of $\sigma(z)$ below this particular collimator will be affected by the reduced mean square angle of travel of the electrons. This is demonstrated in Table 5.3 where there is a significant discrepancy between the measured and predicted data for all the beam energies investigated. The introduction into the formalism of an empirical perturbation factor f for the mean square angle of travel of the electrons has some surprising predictive power. For a given field size setting the same perturbation factor may be used for any beam energy or SSD as shown in Tables 5.3 and 5.4 respectively. Such an empirical approach is obviously limited. One limitation is that the empirical perturbation factor must be determined at each field size (Table 5.6) to reflect the measured variation of $\sigma(z)$ with

field size (Figure 5.16). Also, the scaling of the perturbation factor with energy does not work well for the 7 MeV beam below a square field size of 6 cm x 6 cm. Physically this perturbation factor represents the decrease in mean square angle of travel of electrons at points close to a field edge from the value predicted on the central axis of the field for an isotropic source.

The prediction of beam profile shape is an important component of treatment planning. Knowledge of the change in beam output with treatment geometry is equally important. Both are related to lateral scatter disequilibrium. Figure 5.17 shows that for a fixed square field size of 6 cm x 6 cm the change in beam output with SSD and beam energy is accounted for within 5%, by the inverse square law and lateral scatter disequilibrium effects predicted by Equation 5.6. The agreement between the measured and predicted data is equally good for other field sizes as demonstrated in Figure 5.18 for a 7 MeV beam and Figure 5.19 for a 10 MeV beam. The agreement between the measured and predicted data although good is not perfect, and indicates some possible systematic errors. These errors may be due to the instability in beam output for the Sagittaire Therac 40 being $\pm 3\%$ for a given reading and hence $\pm 6\%$ on a ionization ratio, or the implicit assumption in Equation 5.6 of having a coplanar collimation system.

Figure 5.20 shows that the reduction of beam output with a

reduction in field size is strongly dependent on beam energy. Figure 5.21 compares the measured output variation for the 7 MeV and 32 MeV beams with that predicted by Equation 5.6. The discrepancy between the measured and predicted data in Figure 5.21 indicates there is another effect, in addition to lateral scatter disequilibrium, which reduces beam output with a reduction in field size. Most probably this is the effect of radiation backscattering from the top of the collimator system into the monitor chamber. The gun current and hence the electron output is controlled by a feedback mechanism based on the signal from the monitor chamber. As the field size is reduced there is an increase in collimator surface available for the electrons to backscatter into the monitor chamber. This causes an increase in the signal and therefore a corresponding decrease in the actual electron output.

Often noted in the literature (eg. Fehrentz et al 1976, Schroder-Babo 1983) is the increase in FWHM of normalized electron beam profiles above that normally expected on geometrical grounds. This increase is most noticeable for low beam energies and small field sizes. Table 5.6 demonstrates that if the values of $\sigma(z)$ are known or measured, then Equation 5.8 may be used to accurately predict the FWHM of rectangular beam profiles for any energy and field size. A comparison of the measured and predicted results clearly show that the increase in

FWHM of beam profiles above that geometrically expected can be satisfactorily explained by lateral scatter disequilibrium effects.

The close agreement between the predicted and measured results for the beam output at a fixed field size and the FWHM data is achieved simply by correctly parameterizing the beam in air on the basis of Fermi-Eyges theory and then accounting for lateral scatter disequilibrium effects. This indicates that the concept of a "virtual" source (Briot and Dutreix 1976, Cecatti et al 1983) for magnetically scanned broad electron beams is redundant.

5.9 Conclusion

Fermi-Eyges theory has excellent predictive power in air and may be applied to magnetically scanned broad beams from the Sagittaire Therac 40 electron accelerator. The beams from this accelerator may be modelled in the air space above patients by a collimated isotropic point source with thick lead collimation assumed equivalent to an infinitely thin absorbing plate. The position at which the plate is located depends upon the angle the thick collimation or block makes with the central axis. Blocks whose edges make positive angles with the central axis require the location of the equivalent plate to correspond to the surface of the thick block closest to the source, straight-edged blocks require the location of the plate at a position corresponding to the centre of the thick block and blocks with negative angles to

the central axis require the location of the plate at a position corresponding to the surface of the thick block furthest from the source. This accelerator model is very powerful for predicting beam profile shape in treatment fields whose edges are defined by a single or trimmer collimator. It is able to predict accurately the shape of beam profiles for any clinically used SSD, beam energy and field size and does not require any input data.

For field edges defined by a double collimator system the model overestimates penumbra width. This discrepancy is probably due to the presence of the upper collimator in the system limiting the size of the field and hence perturbing the mean square angle of travel $\overline{\theta_x^2}(z)$ of the electrons incident at the lower collimator from the value on the central axis of the beam. This notion is supported by the introduction of an empirical multiplicative perturbation factor for $\overline{\theta_x^2}(z)$ which gives good agreement with measured data and which is independent of beam energy or SSD for a given field size setting.

The accelerator model presented may also be used to predict within 5% the changes in beam output for a fixed field size with SSD or beam energy due to lateral scatter disequilibrium effects. However, changes in beam output with field size are not accurately predicted due to Fermi-Eyges theory being unable to account for the backscattering of electrons from the top of the photon collimators into the monitor chamber. The increase in FWHM of

beam profiles above the FWHM expected on geometrical grounds at small field sizes and low beam energies is satisfactorily explained by lateral electron disequilibrium effects and is adequately predicted using the accelerator model. The accuracy of the output and FWHM predictions demonstrates that the use of a "virtual" source concept for magnetically scanned electron beams is redundant.

Appendix 5.1

Relationship between broad beam penumbra width and electron pencil beam spread.

The fluence distribution $F(z,x,y)$ in a broad square electron field which is blocked by a large thin absorbing plate placed some distance b off the central axis and parallel to the y -direction field edge is given by,

$$F(z,x,y) = \frac{1.}{z^2} \frac{1.}{4} \cdot \left[\text{ERF} \frac{(a(z)-x)}{\sqrt{2} \sigma'} - \text{ERF} \frac{(-b(z)-x)}{\sqrt{2} \sigma} \right] \quad (\text{A5.1})$$

$$\cdot \left[\text{ERF} \frac{(a(z)-y)}{\sqrt{2} \sigma'} - \text{ERF} \frac{(-a(z)-y)}{\sqrt{2} \sigma'} \right]$$

Where $a(z)$ is the half-field width at depth z defined by the square field collimation system, $b(z)$ is the field dimension in the negative x -direction at depth z formed by the thin absorbing plate, x and y are lateral coordinates, σ' is the root mean square spatial spread of a pencil beam at depth z when defined at the level of the square field collimation system and σ is the root mean square spatial spread of a pencil beam at depth z when defined at the level of the thin absorbing plate.

The central axis fluence profile in the x -direction at depth z may therefore be computed from Equation A5.1 to be:

$$F(z,x,0) = \frac{1.}{z^2} \frac{1.}{4} \left[\frac{\text{ERF}(a(z)-x)}{(\sqrt{2} \sigma')} - \frac{-\text{ERF}(-b(z)-x)}{(\sqrt{2} \sigma)} \right] \cdot 2 \frac{\text{ERF} a(z)}{(\sqrt{2} \sigma')} \quad (\text{A5.2})$$

The value of the x-position corresponding to the fluence maximum of this profile, X_{max} , may be computed by setting $d/dx \cdot [F(z,x,0)]$ equal to zero,

$$\frac{d}{dx} \cdot F(z,x,0) = \frac{1}{z^2} \cdot \frac{1}{4} \cdot 2 \operatorname{ERF} \frac{a(z)}{\sqrt{2} \sigma'} \quad (A5.3)$$

$$\cdot \frac{-2}{\sqrt{2\pi} \sigma'} \cdot \operatorname{EXP} \frac{-(a-x)^2}{\sqrt{2} \sigma'^2} + \frac{2}{\sqrt{2\pi} \sigma} \cdot \operatorname{EXP} \frac{-(-b-x)^2}{\sqrt{2} \sigma^2}$$

Which leads to a quadratic equation in X

$$- \frac{(a-x)^2}{\sigma'^2} + \frac{(b+x)^2}{\sigma^2} = 2 \log_e \cdot \frac{\sigma'}{\sigma} \quad (A5.4)$$

and the positive root of this equation is the value of X_{max} . The relationship between the penumbra width W below the thin absorbing plate and the value of pencil beam spread σ' may now be obtained by noting that the tangent to the central axis fluence profile at the 50% point $-b(z)$, is equal to the maximum fluence divided by W .

$$\frac{d}{dx} \cdot [F(z,x,0)]_{x=-b} = \frac{F(z, X_{max}, 0)}{W} \quad (A5.5)$$

Substituting the value of X_{max} and Equations A5.2 and A5.3 into Equation A5.5 results in the relationship.

$$W = \sqrt{2\pi} \cdot \left[\operatorname{ERF} \frac{(a - X_{max})}{\sqrt{2} \sigma'} - \operatorname{ERF} \frac{(-b - X_{max})}{\sqrt{2} \sigma} \right] \quad (A5.6)$$

$$\left[\frac{1}{2 \sigma} - \frac{1}{2 \sigma'} \cdot \operatorname{EXP} - \frac{(a+b)^2}{2 \sigma'^2} \right]$$

For an unblocked square field of penumbra width W' the relationship

becomes:

$$W' = \frac{\sqrt{2\pi'} \sigma' \cdot \text{ERF} \frac{a(z)}{2 \sigma'}}{1 - \left[\text{EXP} - \frac{2a^2}{\sigma'^2} \right]} \quad (\text{A5.7})$$

and in the limit that $a \gg \sigma'$ we obtain the approximation of Van Gastern (1984).

$$W' = \sqrt{2\pi'} \sigma' \quad (\text{A5.8})$$

The value of σ' may be computed iteratively from Equation A5.7 using square field penumbra. Substitution of this value of σ' into Equation A5.6 then permits the computation of σ from the penumbra width W below the thin absorbing plate blocking the square field.

Chapter 6

APPLICATION OF FERMI-EYGES SCATTERING THEORY TO
MAGNETICALLY SCANNED THERAPEUTIC ELECTRON BEAMS IN TISSUE

6.1 Introduction

Therapeutic electron beam treatment planning requires dose computation algorithms suitable for implementation on the small computers commonly encountered in radiotherapy centres. Currently, most pencil beam algorithms available (Hogstrom et al 1981, Brahme et al 1981, Bruinvis et al 1983, Storchi and Hurzenga 1985) are based on the small angle multiple scattering theory developed by Fermi (1941) and Eyges (1948). This theory is eminently suitable for describing the penetration of electrons in the air space above patients as shown in Chapter 5. However, it has major limitations in tissue media. These limitations are due to the theory being restricted to small angle multiple scattering and therefore ignoring the non-negligible secondary interaction processes of large angle scattering, delta-ray production bremmstrahlung production and electron absorption in tissue. Large angle scattering and delta-ray production limit the success of Fermi-Eyges theory at shallow depths in tissue whereas electron absorption becomes important near the electrons' range in tissue. To overcome these limitations, empirical data is incorporated into the Fermi-Eyges theoretical framework to modify the calculations so as to achieve closer agreement with measured dose distribution data. Previous workers have used values of electron pencil beam spread derived both empirically (Lillicrap et al 1975, Brahme et al 1980 and Abou-Mandour et al 1983)

and semi-empirically, as the input data to dose computation algorithms. Semi-empirical methods combine solutions for rectangular broad beam dose distributions computed from the convolution of the Fermi-Eyges pencil beam over the broad beam area with measured broad beam dose data, to compute values of $\sigma(z)$ at depth in homogeneous media. Kozlov and Shishov (1982) and Bruinvis et al (1983) utilize the ratio of central axis depth doses for small and large fields to compute semi-empirical values of $\sigma(z)$, while alternatively, the scattering of electrons beyond a collimator edge has been used by Perry and Holt (1980), Hogstrom et al (1981), Werner et al (1982), Van Gasteren (1984), and Hogstrom (1985) to obtain semi-empirical values of $\sigma(z)$ from broad beam penumbra or slit beams.

The present work provides an intercomparison between one empirical and two semi-empirical methods of deriving values of electron pencil beam spread $\sigma(z)$ in homogeneous media. The practical problems and theoretical limitations of each method are examined in detail. In addition, the penumbra method is used to derive semi-empirical values of $\sigma(z)$ in homogeneous muscle, lung and bone-equivalent media over the range of therapeutic electron beam energies commonly used in radiotherapy. These data are compared to theoretical calculations provided by the isotropic source model of magnetically scanned beams, previously developed by Sandison and Huda (1987) on the basis of Fermi-Eyges

multiple scattering theory, and with the empirical modifications suggested by Werner et al (1982) and Lax et al (1983) to account for the absorption of electrons near the end of their range.

6.2 Methods of deriving pencil beam spread in tissue

6.2.1 Theoretical

After travelling through the air space above patients the electrons from the accelerator enter the patients' tissue. Soft-tissue is about 1000 times the density of air and the electrons lose energy in this medium at a rate of about 2 MeV cm⁻¹. The energy loss of electrons in tissue may be taken into account within the framework of Fermi scattering theory by utilizing the solution due to Eyges (1948). It is assumed in his work that the loss of energy of the electrons comprising the pencil beam is a well defined function of depth only in the scattering medium. The variance of the Gaussian spatial spread of a pencil beam incident at the tissue surface is then given by (Brahme 1975, ICRU 1984a)

$$\sigma^2(z) = \sigma^2(0) + \overline{\theta_x^2}(0)z^2 + \overline{\theta_x \times}(0)z + \frac{1}{2} \int_0^z k[z-\xi]^2 d\xi \quad (6.1)$$

where the linear scattering power $k(z)$ is a function of the depth z in the medium due to the electron energy loss; $\sigma(0)$ is the spatial variance of the pencil beam at the surface of the medium, $\overline{\theta_x^2}(0)$ is the angular variance of

the pencil beam at the surface, $\overline{\theta_x x}(0)$ is the cross correlation coefficient between lateral position x and projected angle of travel θ_x at the surface and the integral term is the contribution of scattering in the medium. Following the procedure of Jette et al (1983), $k(z)$ may be expressed as

$$k(z) = \frac{16\pi e^4}{(PV)^2} \sum_i N_i Z_i (Z_i + 1) \ln 204 Z_i^{-1/3} \quad (6.2)$$

where N_i is the number of atoms per unit volume of element i with atomic number Z_i , e is the electronic charge and (PV) is given by the relativistic identity,

$$PV = \frac{E(E + 2m_0c^2)}{E + m_0c^2} \quad (6.3)$$

where E is the kinetic energy of the electrons at depth z in the medium and m_0c^2 is the rest mass energy of the electron.

Andreo and Brahme (1981,1984) have shown using Monte Carlo studies that the kinetic energy E of an electron in a pencil beam is a function both of depth in the scattering medium and its radial position. Therefore, the assumption of Eyges (1948) that energy loss is a function of depth only for a pencil beam is incorrect. However, patients are treated using broad beams whose dose distribution is derived by the summation of dose from many pencil beams.

This summation process compensates the increased energy loss at lateral positions in the pencil beam and therefore the assumption that energy loss is a function of depth only is a good one for homogeneous media. Therefore relationships describing broad beam energy variation with depth may be applied to pencil beams. Hogstrom et al (1981) and Jette et al (1983) utilize an empirical formula due to Harder (1965)

$$\bar{E}(z) = E(o) \left[1 - z/R_p \right] \quad (6.4)$$

where $\bar{E}(z)$ is the mean energy at depth z equated with the most probable energy at depth, $E(o)$ is the incident beam energy at the tissue surface and R_p is the practical range in the homogeneous medium considered. The practical range may be measured for homogeneous media or derived from the empirical formula obtained by Markus (1964)

$$\rho \langle Z/A \rangle R_p = 0.285 E(o) - 0.137 \quad (6.5)$$

where $\langle Z/A \rangle = \sum_i f_i Z_i / A_i$, f_i is the fraction by weight of element i of atomic number Z_i and atomic weight A_i and ρ is the density of the medium.

The theoretical values of $\sigma(z)$ computed using Fermi-Eyges theory do not account for range straggling.

Modifications to the theoretical results have previously been suggested by Werner et al (1982) and Lax et al (1983) to account for this effect. Werner et al (1982) subtract the dose contribution due to bremsstrahlung and show that their remaining electron pencil beam spread data may be well fit by assuming all electrons scattering to angles greater than $\pi/4$ to be absorbed locally. The modification suggested by Werner et al (1982) is

$$\sigma(z) = \sigma(z)_{\text{Fermi-Eyges}} \cdot \text{ERF} \left[\frac{\theta_{\text{max}}}{\sqrt{2 \overline{\theta_x^2}(z)}} \right] \quad (6.6)$$

where θ_{xmax} equals $\pi/4$ and $\overline{\theta_x^2}(z)$ is the mean square angle of travel of the electrons at depth z computed using Fermi-Eyges theory. The modification suggested by Lax et al (1983) was derived by fitting an empirical function to Monte Carlo data for a monodirectional pencil beam incident upon water at energies of 5, 10 and 20 MeV. The empirical, multiplicative formula provided includes the bremsstrahlung dose fraction and is given by

$$\sigma(z) = \sigma(z)_{\text{Fermi-Eyges}} \cdot Q(z) \quad (6.7)$$

$$\text{where } Q = \text{EXP} \left[-R^{1.2} (1.5 - R) \right] \quad (6.8)$$

$$R = 0.95 (Z/R_p) \quad (6.9)$$

and R_p is the practical range of the incident electrons.

6.2.2 Semi-Empirical from Central Axis Dose Ratios

Theoretically derived values of $\bar{\sigma}(z)$ based on Fermi-Eyges theory only include small-angle multiple scattering collisions. The use of such theoretical values for describing penumbra shape or the variation of central axis depth dose in inhomogeneous tissue-equivalent media is limited because other interaction effects are important. To overcome this limitation, some dose computation algorithms based on Fermi-Eyges theory use values of $\bar{\sigma}(z)$ as input data which are derived semi-empirically from the ratio of central axis depth doses for small and large fields (Kozlov and Shishov 1982, Bruinvis et al 1983). This method is based on the dose distribution of a rectangular broad electron field $D(x,y,z)$ computed by convolution of the pencil beam dose distribution over the broad beam area.

$$D(z,x,y) = \frac{D_0(z)}{4} \cdot \left[\frac{SSD}{SSD+z} \right]^2 \cdot \left[\frac{\text{ERF}\left(\frac{x+a}{\sqrt{2}\sigma}\right) - \text{ERF}\left(\frac{x-a}{\sqrt{2}\sigma}\right)}{\sqrt{2}\sigma} \right] \cdot \left[\frac{\text{ERF}\left(\frac{y+a}{\sqrt{2}\sigma}\right) - \text{ERF}\left(\frac{y-a}{\sqrt{2}\sigma}\right)}{\sqrt{2}\sigma} \right] \quad (6.10)$$

where $D(z,x,y)$ is the dose distribution for a diverging square field of length a at depth z in the tissue, x and y are lateral coordinates, SSD is the source surface distance, σ is the root mean square pencil beam spread at

depth z , $D_{\infty}(z)$ is the central axis depth dose distribution for a large field and ERF is the error function. The central axis dose distribution for the square field normalized to the surface value $D(0,0,0)$ is given by

$$\frac{D(z,0,0)}{D(0,0,0)} = \frac{D_{\infty}(z)}{D_{\infty}(0)} \left[\frac{SSD}{SSD+z} \right]^2 \left[\frac{\text{ERF} \frac{a(z)/\sqrt{2} \sigma(z)}{\sqrt{2} \sigma(z)}}{\text{ERF} \frac{a(0)/\sqrt{2} \sigma(0)}{\sqrt{2} \sigma(0)}} \right]^2 \quad (6.11)$$

The ratio N^2 of this quantity for two square fields of length $S(z)$ and $L(z)$ is

$$N^2 = \left[\frac{D_S(z,0,0)}{D_S(0,0,0)} / \frac{D_L(z,0,0)}{D_L(0,0,0)} \right] = \frac{\left[\frac{\text{ERF}(S(z)/\sqrt{2} \sigma(z))}{\text{ERF}(S(0)/\sqrt{2} \sigma(0))} \right]^2}{\left[\frac{\text{ERF}(L(z)/\sqrt{2} \sigma(z))}{\text{ERF}(L(0)/\sqrt{2} \sigma(0))} \right]^2} \quad (6.12)$$

Assuming that the smaller S of these two square fields satisfies the condition that $S(0)/\sqrt{2} \sigma(0) \gg 2$, then Equation 6.12 may be simplified and solved iteratively for $\sigma(z)$

$$N \cdot \frac{\text{ERF} \frac{L(z)}{\sqrt{2} \sigma(z)}}{\sqrt{2} \sigma(z)} = \frac{\text{ERF} \frac{S(z)}{\sqrt{2} \sigma(z)}}{\sqrt{2} \sigma(z)} \quad (6.13)$$

6.2.3 Semi-Empirical from Penumbra

An alternative method of deriving semi-empirical

values of $\sigma(z)$ is to relate this parameter to broad beam penumbra width. The central plane (z,x) of the dose distribution given by Equation 6.6 is

$$D(z,x,0) = D_{\infty}(z) \left[\frac{SSD}{SSD+z} \right]^2 \cdot \left[\frac{\text{ERF}\left(\frac{x+a}{\sqrt{2}\sigma}\right) - \text{ERF}\left(\frac{x-a}{\sqrt{2}\sigma}\right)}{2} \right] \cdot 2 \cdot \text{ERF}\left(\frac{a}{\sqrt{2}\sigma}\right) \quad (6.14)$$

Appendix 5.1 of Chapter 5 has derived the relationship between the penumbra width $W(z)$ of this beam profile to the value of $\sigma(z)$ as

$$W(z) = \sqrt{2\pi}\sigma(z) \cdot \frac{\text{ERF}(a/\sqrt{2}\sigma)}{[1 - \text{EXP}(-2a^2/\sigma^2)]} \quad (6.15)$$

This equation may also be solved iteratively for $\sigma(z)$.

6.2.4 Empirical

Empirical pencil beams may be obtained by collimation (Lillicrap et al 1975 Abou-Mandour et al 1983, McParland and Cunningham 1986). The profile of a pencil beam so produced may be assumed Gaussian and the dose distribution

represented as

$$D(z,x,y) = P(z).EXP[-(x^2+y^2)/2\sigma^2] \quad (6.16)$$

where $P(z)$ is the central axis dose distribution for a pencil beam and the exponential is unity for x and y both equal to zero. The Gaussian function in Equation 6.16 may be replaced by another Gaussian function which is normalized such that its area integral over a transverse plane is unity

$$D(z,x,y) = \frac{D_{\infty}(z)}{2\pi\sigma^2} . EXP[-(x^2+y^2)/2\sigma^2] \quad (6.17)$$

Now, instead of $P(z)$ we have $D_{\infty}(z)$ which is the central axis dose distribution for an infinitely broad field. The empirical values of $\sigma(z)$ were obtained from a measure of full width at half maximum (FWHM) of the pencil beam profiles using the relation

$$\sigma(z) = FWHM/\sqrt{8 \ln 2} \quad (6.18)$$

6.3 Materials and Methods

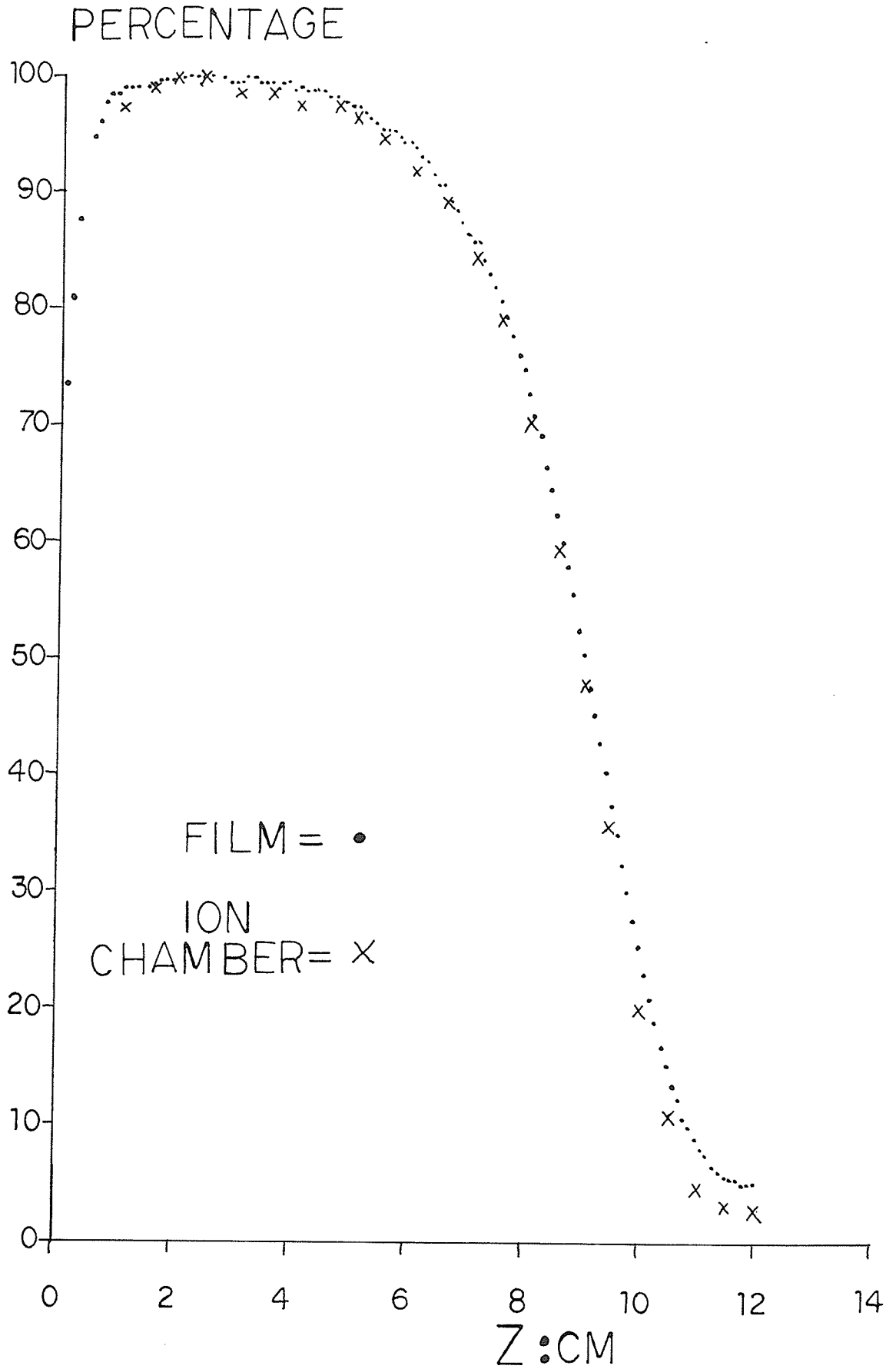
The Sagittaire Therac 40 linear accelerator (Aucouturier 1970) was used to produce electron beams in the energy range 7 to 32 MeV. Central axis depth doses in water and water-equivalent temex (Stacey et al 1961) were measured using Kodak

Industrex M film or a cylindrical Capintec Farmer Type PR-06C ionization chamber of 0.65 ml sensitive volume, inner axial length 2.2 cm and an inner diameter of 0.7 cm. The film and ionization chamber measurements of percentage depth dose agree within 2% over most of the electron range. An example is shown in Figure 6.1 for a 20 cm x 20 cm beam of 22 MeV energy incident upon a temex phantom placed at 100 cm SSD. Conversion from ionization reading to absorbed dose was performed using the electron dosimetry protocol outlined in the AAPM Task Group 21 report (AAPM 1983).

In-phantom beam profile measurements were obtained both perpendicularly and parallel to the central axis of the therapy electron beam using Kodak industrex M film. The film was retained within the manufacturers opaque paper cassette when placed in the perpendicular orientation. However, for profile measurements with the film oriented parallel to the central axis the beam, the paper cassette was removed in a photographic darkroom and the bare film placed in a specially designed holder made from tissue-equivalent material. Three film holders were constructed of the same material as the tissue-equivalent phantoms used for dosimetry. These were white high impact polystyrene muscle substitute, a resin based lung tissue substitute known as LN1 (White 1978) and a resin based bone tissue substitute known as SB3 (White 1978). The physical properties of

Figure 6.1: Comparison of film and ionization chamber measurements for the central axis percentage depth dose of a 20 cm x 20 cm field using a 22 MeV beam energy and 100 cm SSD

TEMEX: 22 MEV



these and other dosimetric materials are given in Table 6.1. The holders were painted matt black to prevent light transmission and sealed using black insulating tape. Film placed in the holder fit such that one of its edges was perfectly aligned with the top surface of the phantom. The holders were placed in the appropriate phantoms, and these phantoms were then squeezed in a vice to exclude air gaps and irradiated. The parallel orientation was most often utilized to conserve film. Films were developed using hand processing and read manually by a Sargent-Welch densitometer (Densichron mode PDD) with a 1 mm diameter light aperture.

The empirical pencil beam produced for this work was formed by a 1 mm hole drilled centrally in a large area lead block of 3.1 cm thickness and irradiated by a 4×4 cm² electron field formed by the photon collimator. The lead block was then positioned on the central axis of this field 20 cm above the phantom surface. Profiles of this pencil beam were measured in temex for a 22 MeV beam energy using the Kodak Industrex M film. The measurements were repeated for both parallel and perpendicular orientations of the film.

Errors at selected data points were determined from the standard deviation of not less than five repeat measurements or have been estimated and are indicated by error bars on data points.

Table 6.1

Physical Properties of Dosimetric Materials

Material	Density $\langle Z/A \rangle^+$ g cm ⁻³		Electron Density e cm ⁻³ x10 ²³	Scattering Power* Constant k ₀ cm ⁻¹
Water	1.00	0.55509	3.3428	47.2689
Polystyrene	1.06	0.53768	3.4322	40.8859
Temex	1.01	0.54716	3.3070	39.9887
LN	0.30	0.52792	0.9537	12.4764
SB3	1.84	0.51484	5.7047	113.8676
Air	1.205x10 ⁻³	0.49975	3.6264x10 ⁻³	56.257x10 ⁻³

$$+ \langle Z/A \rangle = \sum_i F_i (Z_i/A_i)$$

where F_i = fraction by weight of
element Z_i of atomic weight A_i

* Linear scattering power $k(z) = k_0 \cdot \left[\frac{m_0 c^2 (E + m_0 c^2)}{E(E + 2m_0 c^2)} \right]^2$

6.4 Results

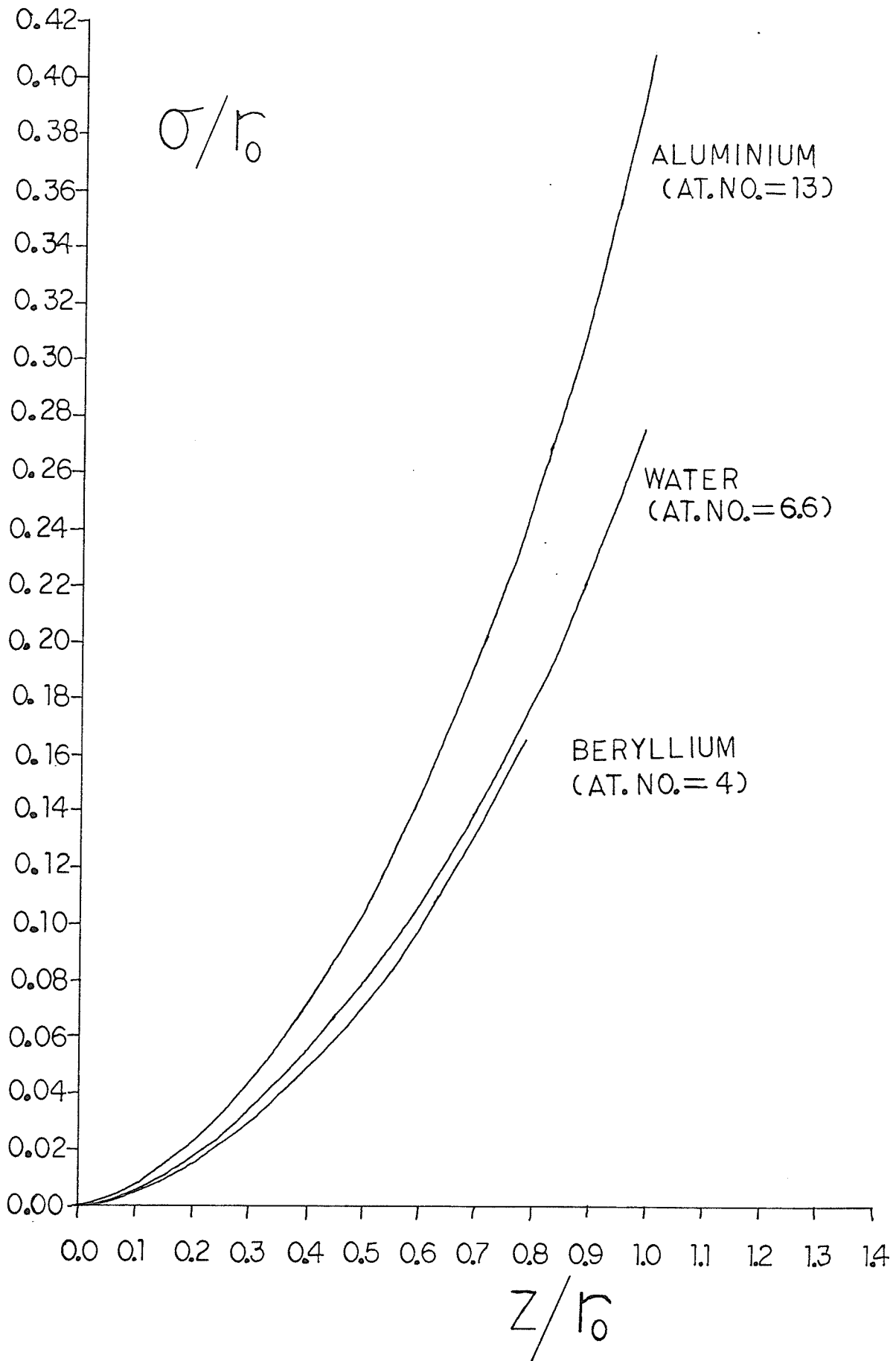
6.4.1 Theoretical Method

The general expression for the spatial variance $\sigma^2(z)$ of a Gaussian pencil at depth z in a medium is given by Equation 6.1. The first three terms of this expression depend upon parameters evaluated at the surface. These parameters define the contribution to the spread of the pencil beam provided by air scattering from the electron source to the surface of the medium. It is important to evaluate these parameters since their contribution to pencil beam spread can be dominant, especially at shallow depths.

Figure 6.2 shows the theoretical variation $\sigma(z)$ with depth for a point monodirectional pencil beam incident upon the surface of homogeneous media of different atomic number. Energy loss has been incorporated through Harder's equation using the solution to the integral term of Equation 6.1 computed by Jette et al (1983). The axes have been expressed in dimensionless units by scaling distance in terms of the continuous slowing down approximation range Γ_0 . This ensures that any differences between curves are due to the lateral scattering power of the medium. It can be seen in Figure 6.2 that the theoretical value of $\sigma(z)$ at a given depth z increases with

Figure 6.2: Theoretical variation of $\sigma(z)$ with depth z in homogeneous scattering media of different atomic number for a point monodirectional pencil beam.

22 MEV



an increase in the atomic number of the medium. Figure 6.3 demonstrates the decrease in the theoretical value of $\sigma(z)$ as the energy of a point monodirectional pencil beam incident upon water increases. This behaviour is consistent with the dependence of theoretical $\sigma(z)$ values on the linear scattering power $k(z)$, which increases with the atomic number of the medium and decreases as the electron energy increases.

6.4.2 Semi-empirical Central Axis Dose Ratio Method

The smallest square field size obtainable with the Sagittaire Therac 40 was found to be 2.2 cm x 2.2 cm at 100 cm SSD. The central axis depth ionization curve in temex for this size of field is compared in Figure 6.4 to the depth ionization curve of a 20 cm x 20 cm field for a 22 MeV beam energy. The curves measured in temex using an ionization chamber, have not been normalized in order to show absolute differences in ionization and their very different shapes. It is this difference in shape which allows the computation of semi-empirical $\sigma(z)$ values. Figure 6.5 shows the values of $\sigma(z)$ derived from Equation 6.9 using the central axis depth ionization data presented in Figure 6.4. The value of $\sigma(z)$ increases with depth in temex to a maximum which occurs in this instance at about 0.9 times the continuous slowing down

Figure 6.3: Theoretical variation of $\sigma(z)$ with depth z in water and incident beam energy for a point monodirectional pencil beam.

WATER

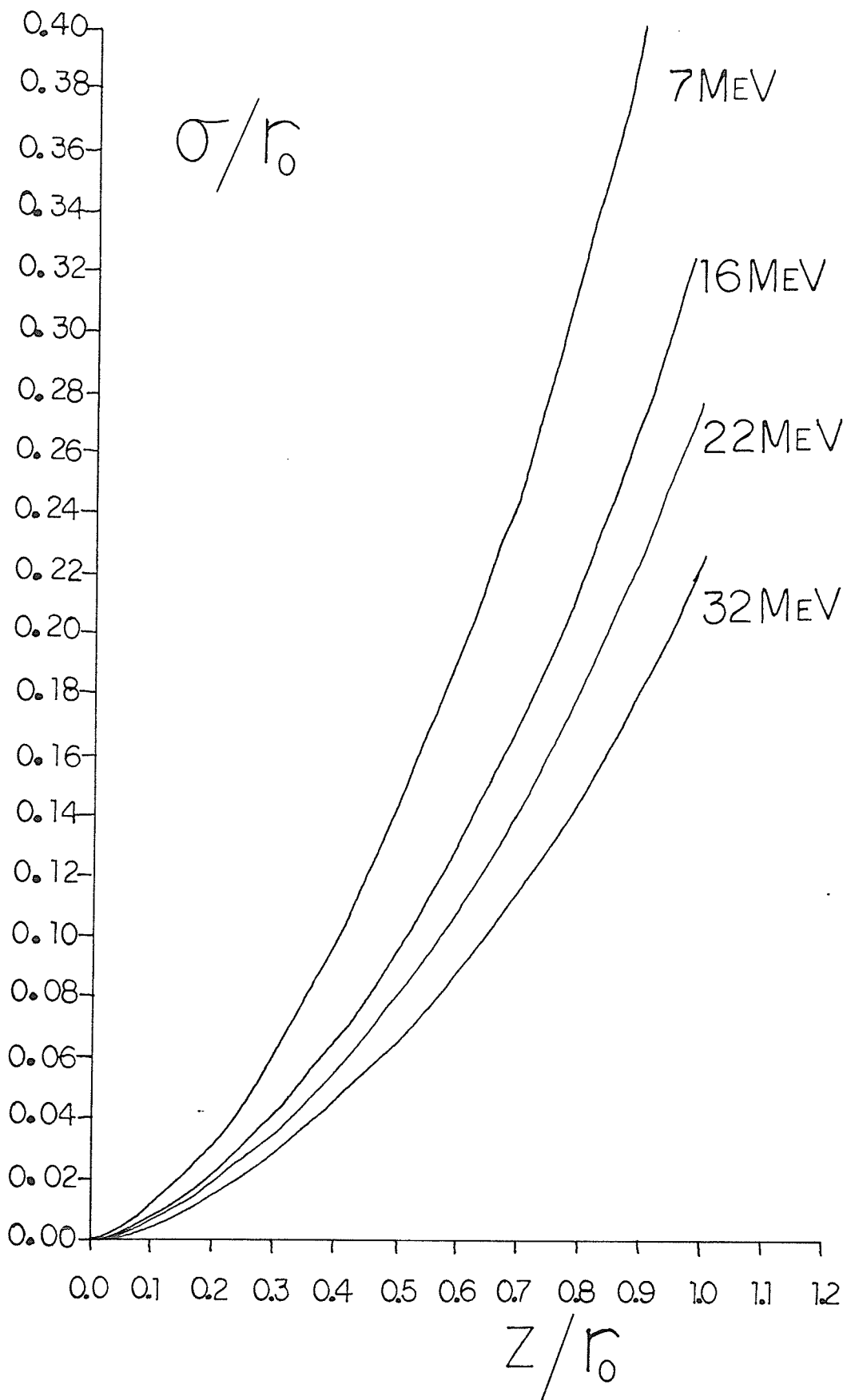


Figure 6.4: Depth ionization curves in tenex for a 22 MeV beam energy for both a 20 cm x 20 cm and a 2.2 cm x 2.2 cm field.

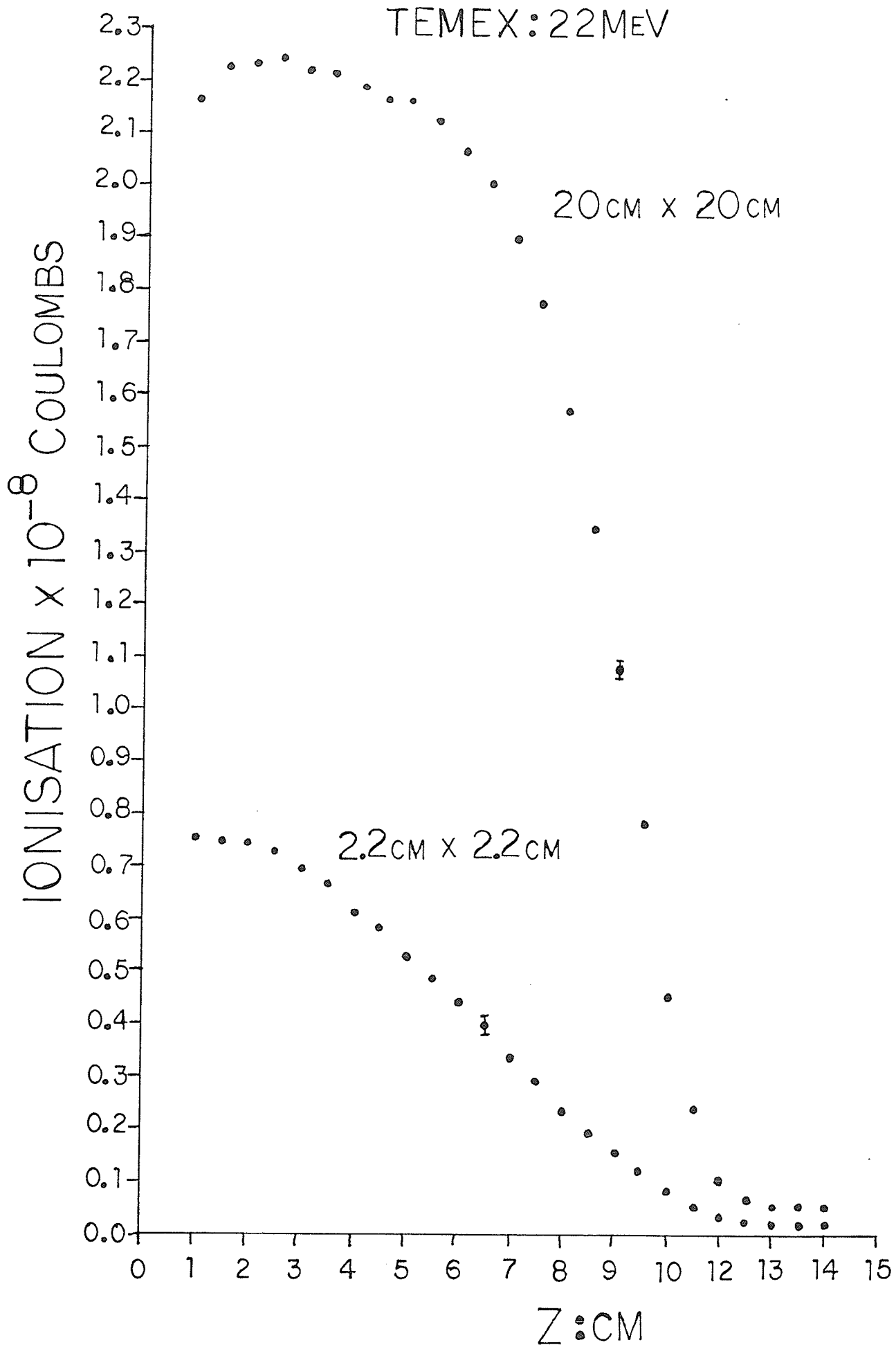
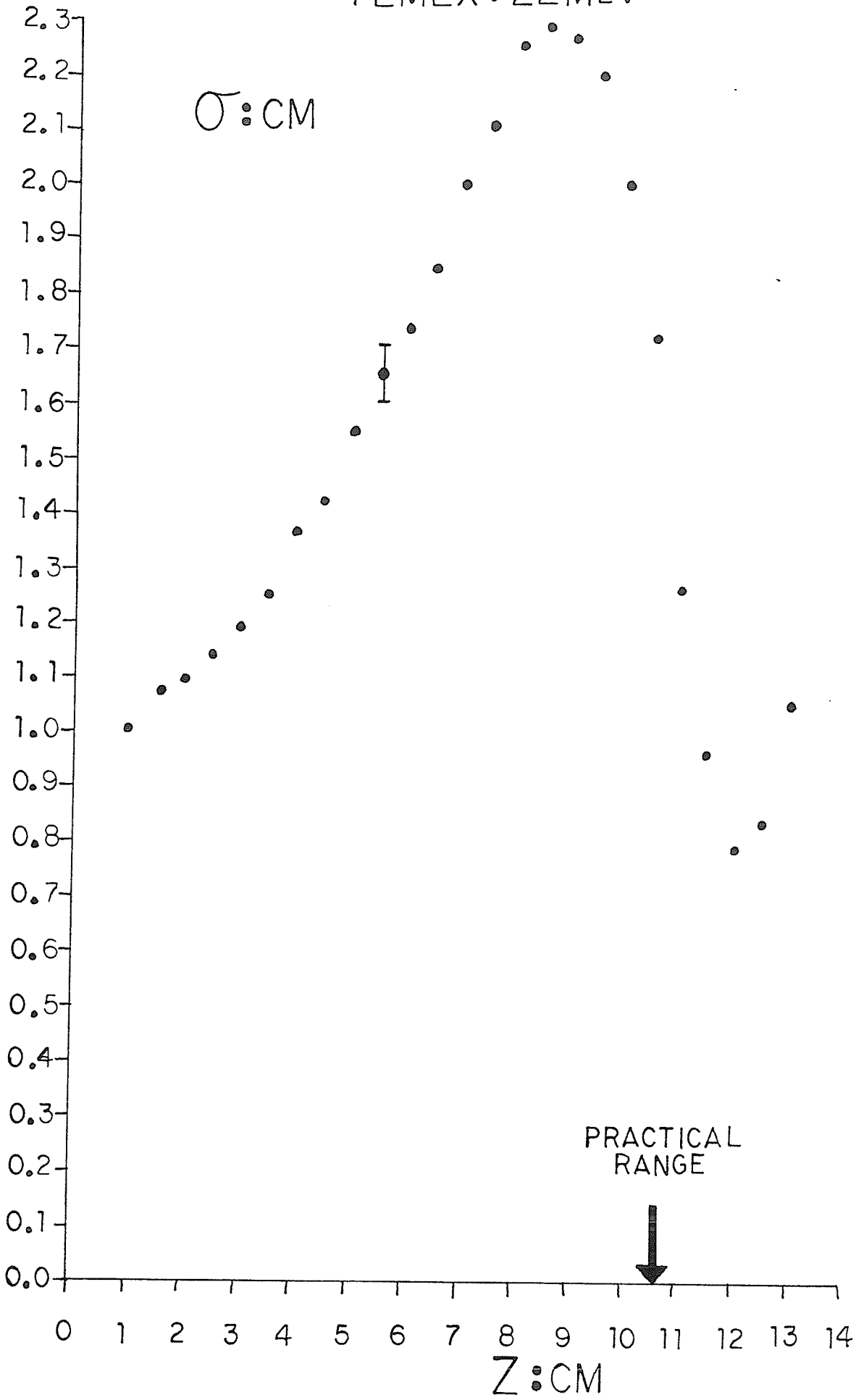


Figure 6.5: Semi-empirical $\sigma(z)$ values generated from central axis data presented in Figure 6.4.

TEMEX: 22MEV



approximation (CSDA) range r_0 . At greater depths the values of $\sigma(z)$ decrease sharply and then rise again slightly. The sharp decrease in $\sigma(z)$ is due to range straggling of the electrons and the slight rise in the deepest region is due to the bremsstrahlung background.

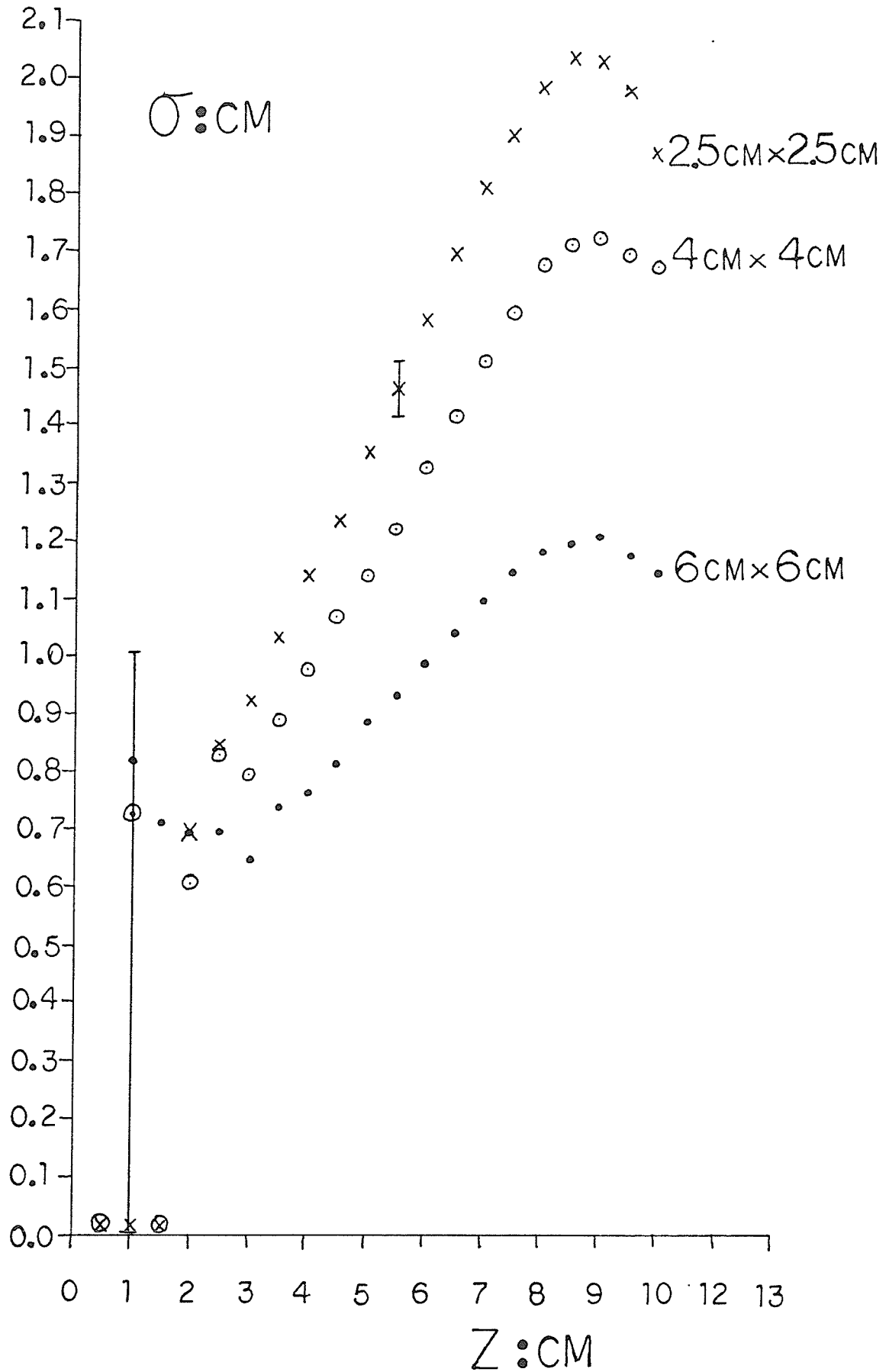
The value of the small field size chosen to generate these semi-empirical values of $\sigma(z)$ is somewhat arbitrary. Theoretically however one expects the value of $\sigma(z)$ to be unique and independent of the small field size used. Figure 6.6 presents the values of $\sigma(z)$ generated in temex for a 22 MeV beam at 100 cm SSD and central axis depth dose data for a large square field of 20 cm x 20 cm and small square fields of 2.5 cm x 2.5 cm, 4.0 cm x 4.0 cm and 6.0 cm x 6.0 cm. The values of $\sigma(z)$ generated are definitely dependent on the value of the small field size chosen. Also, at shallow depths the values of $\sigma(z)$ show a wide variability.

6.4.3 Semi-empirical Penumbra Method

The values of $\sigma(z)$ derived from broad beam penumbra depend upon the collimation geometry defining the field. This is due to the differences in the in-air scattering components to $\sigma(z)$, defined in Equation 6.1. Figure 6.7 shows semi-empirical values of $\sigma(z)$ derived from the penumbra in polystyrene of a trimmed 10 cm x 10 cm field

Figure 6.6: Variation of semi-empirical $\sigma(z)$ values in temex with small field central axis depth dose for a 22 MeV beam energy.

TEMEX: 22 MEV



for beam energies of 7 and 22 MeV and an SSD of 100 cm. Only $\sigma(z)$ values up to the practical range of the electrons are computed. The full curves in Figure 6.7 indicate the theoretical variation of $\sigma(z)$ predicted by Fermi-Eyges theory and the collimated isotropic source model of the accelerator presented in Chapter 5. Under identical geometrical conditions, semi-empirical values of $\sigma(z)$ were derived from the penumbra of the broad beam in lung-equivalent and bone-equivalent materials for electron beam energies of 7, 16 and 22 MeV.

Figure 6.8 presents the data for the homogeneous lung-equivalent phantom at 7 and 22 MeV beam energy. The electron range, r_0 of a 22 MeV electron in lung is about 35 cm. This is larger than the dimensions of the lung phantom employed and accounts for the incomplete data set shown in Figure 6.8 for the 22 MeV beam energy. The full curves indicate the predictions of Fermi-Eyges theory. Data for the homogeneous bone-equivalent phantom is shown in Figure 6.9 for the 7 and 22 MeV beam energies. Again, the full curves represent the predictions of Fermi-Eyges theory. The polystyrene, lung and bone data presented in Figures 6.7, 6.8 and 6.9 demonstrate that the measured values of $\sigma(z)$ agree closely with the theoretical predictions up to a depth of about 0.7 times the CSDA range

Figure 6.7: Variation of semi-empirical $\sigma(z)$ values in polystyrene derived from the penumbra of a 10 cm x 10 cm field for 7 and 22 MeV incident beam energies.

POLYSTYRENE

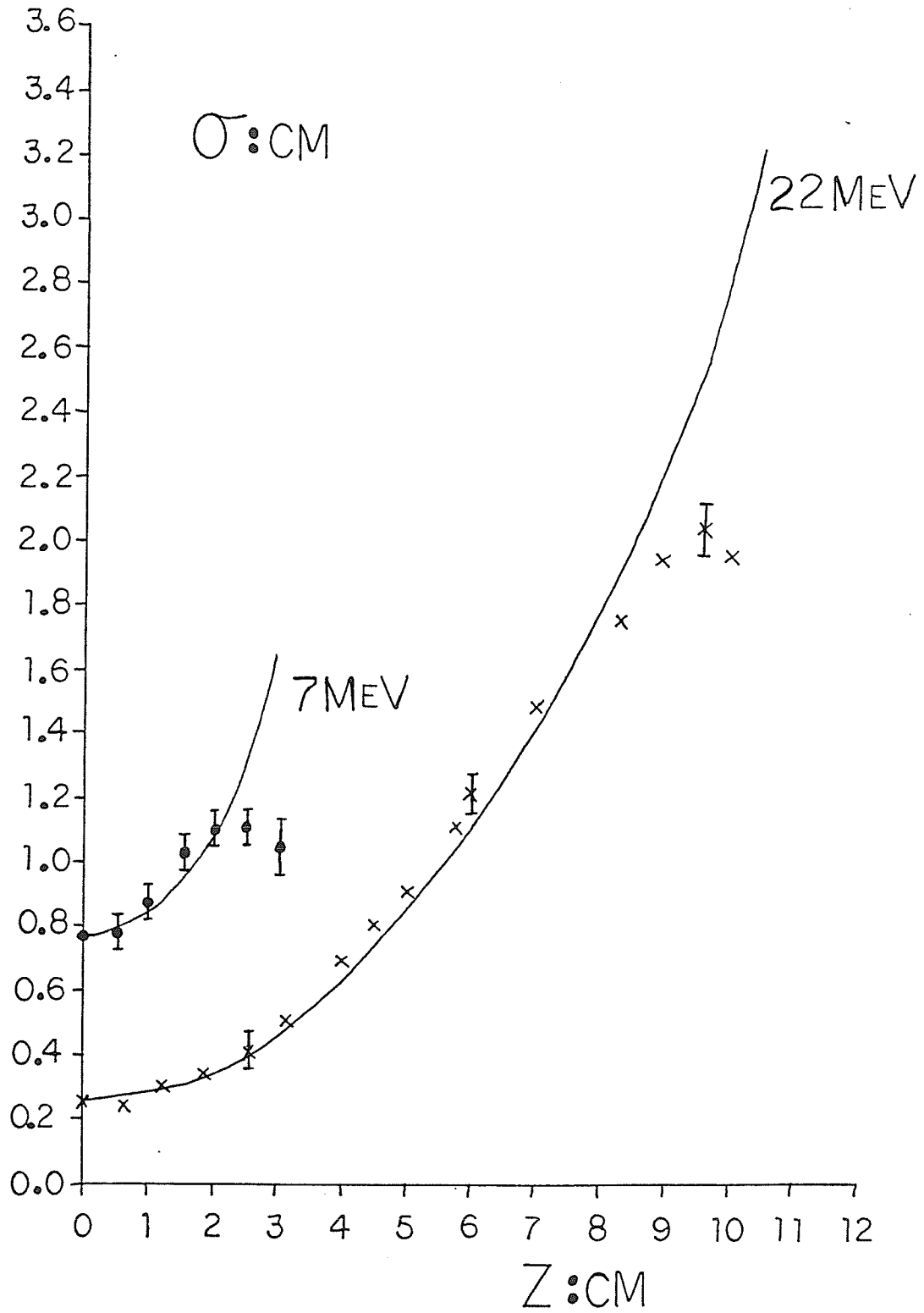


Figure 6.8: Variation of semi-empirical $\sigma^-(z)$ values in lung-equivalent material derived from the penumbra of a 10 cm x 10 cm field for 7 and 22 MeV beam energies.

LUNG

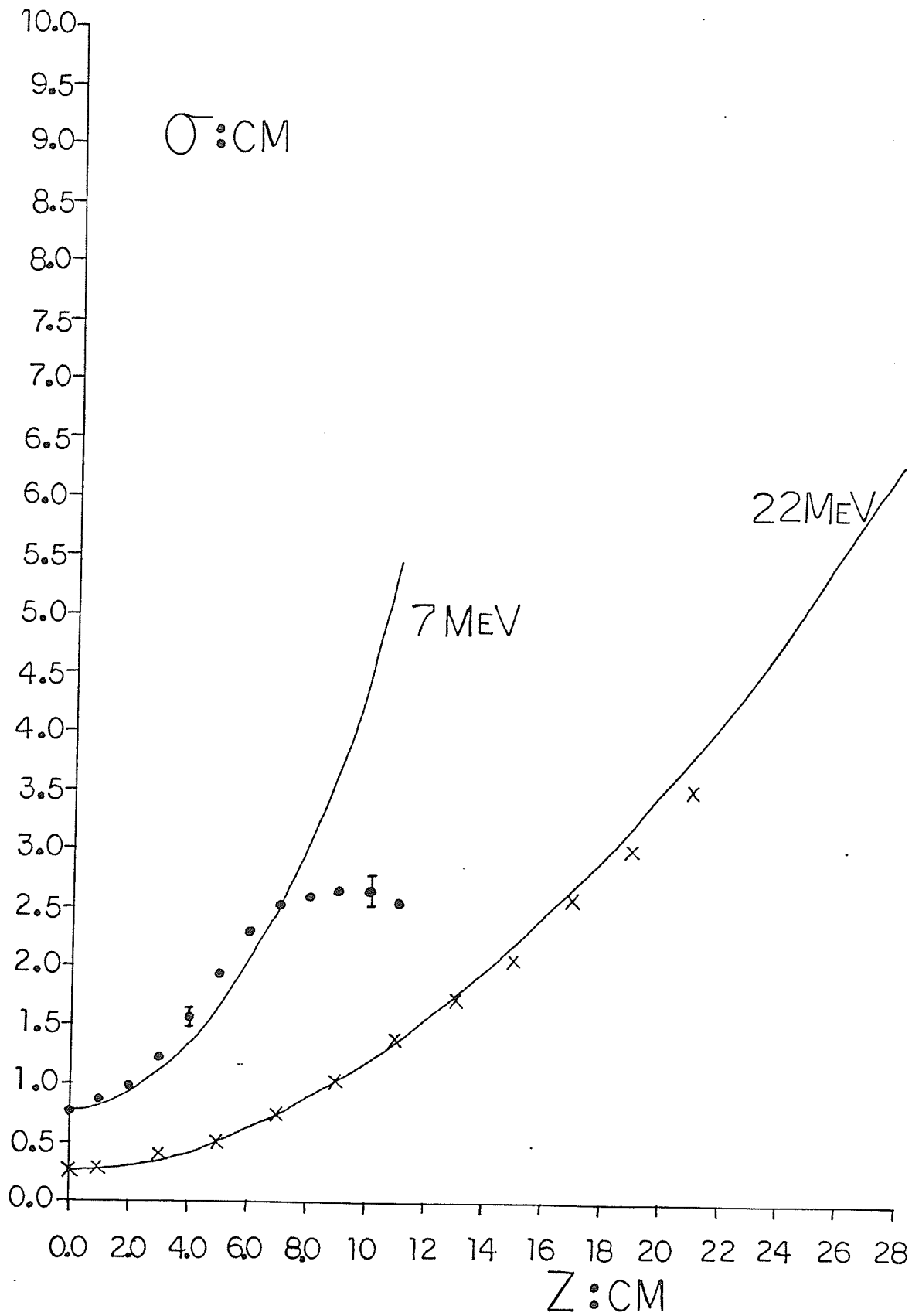
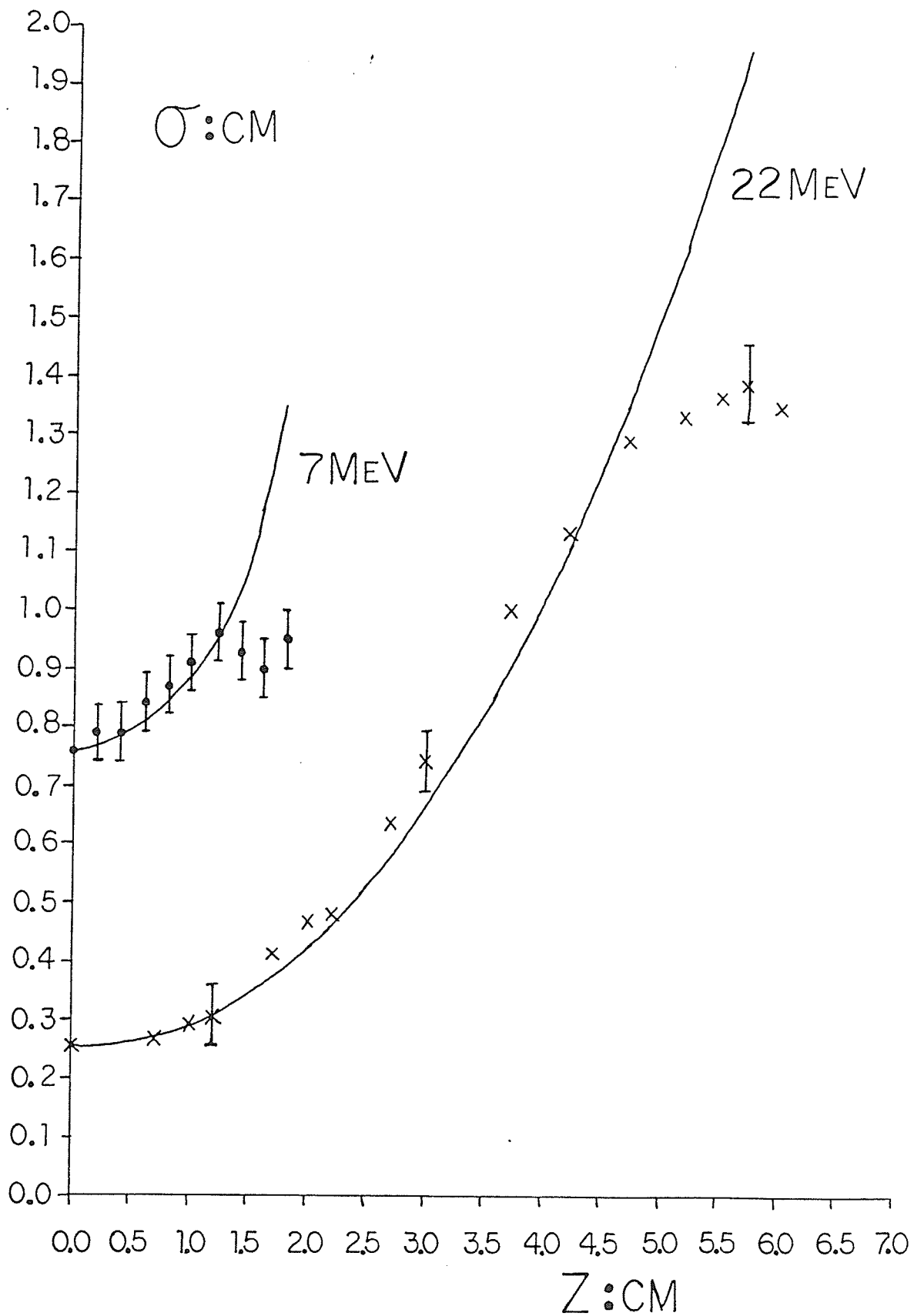


Figure 6.9: Variation of semi-empirical $\sigma(z)$ values in bone-equivalent material derived from the penumbra of a 10 cm x 10 cm field for 7 and 22 MeV beam energies.

BONE



for the incident electrons. Beyond this depth a substantial discrepancy between the theory and measured data is apparent. This departure of the theory from measured data has been noted previously by Perry and Holt (1980) and is due, at least in part, to range straggling. Empirical modifications of the theory suggested by Werner et al (1982) and Lax et al (1983), to account for this effect are shown in Figure 6.10 to give better agreement with the measured data for a 22 MeV beam incident upon polystyrene. Further comparisons of these empirical modifications to the theory for a point monodirectional pencil beam are presented for measured data derived from the penumbra of a 16 MeV broad beam incident upon the lung phantom in Figure 6.11 and also the bone phantom in Figure 6.12. In Figures 6.10, 6.11 and 6.12 the components of spread due to air scattering have been subtracted so that the comparisons presented are for a point monodirectional pencil beam incident upon the phantom surface.

6.4.4 Empirical Method

The 1 mm diameter pinhole used to produce an empirical pencil beam is so small that the emerging electrons may be considered initially monodirectional along the z-axis. Figure 6.13 shows a profile of the 22 MeV pencil beam at a depth of 1 cm in temex and another at a depth of

Figure 6.10: Comparison of measured semi-empirical $\sigma(z)$ values in polystyrene for a 22 MeV beam energy with predictions of Fermi-Eyges theory and empirical modifications to this theory.

POLYSTYRENE: 22MeV

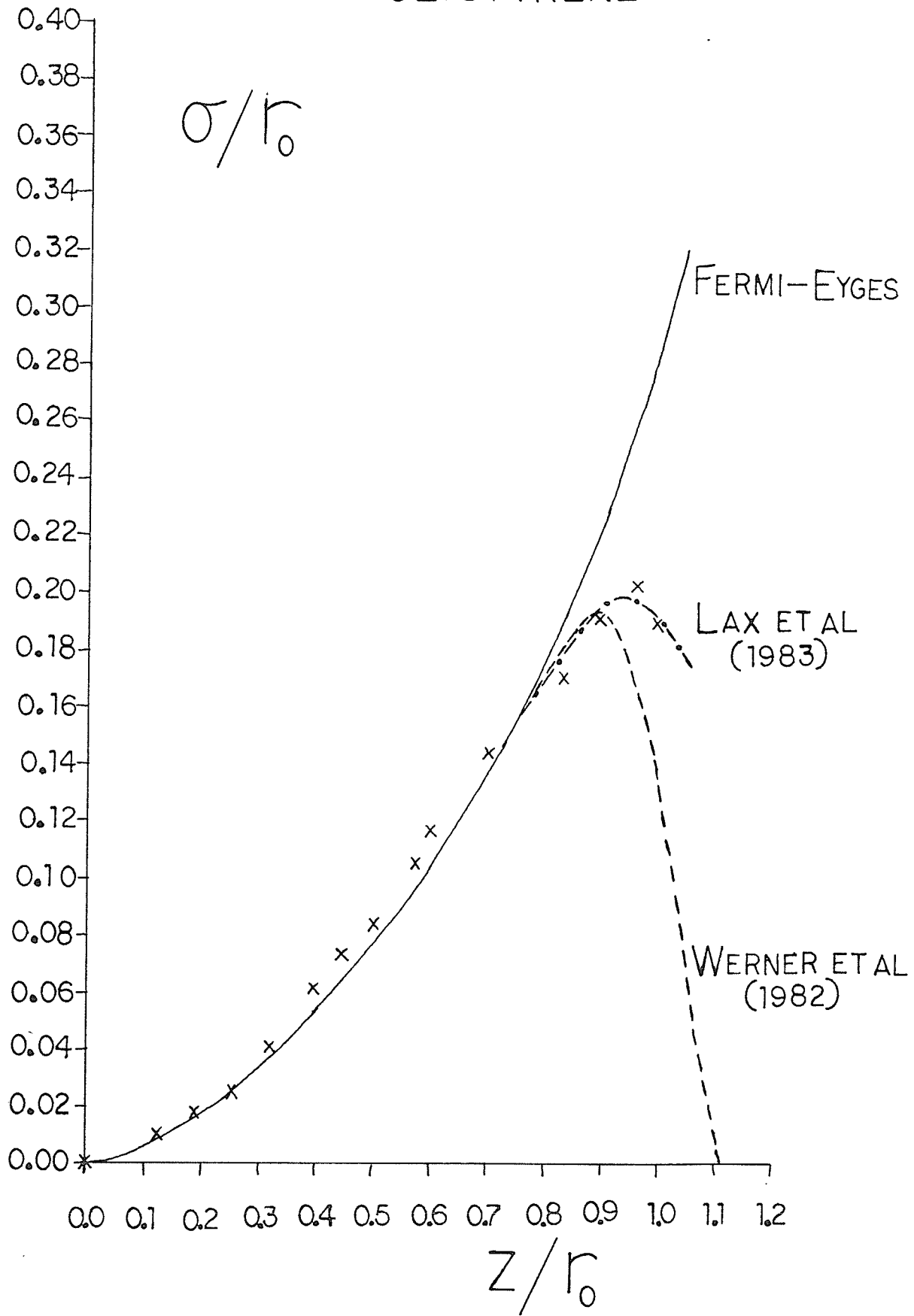


Figure 6.11: Comparison of measured semi-empirical $\sigma(z)$ values in lung-equivalent material for a 16 MeV beam energy with empirical modifications to Fermi-Eyges theory.

LUNG : 16 MeV

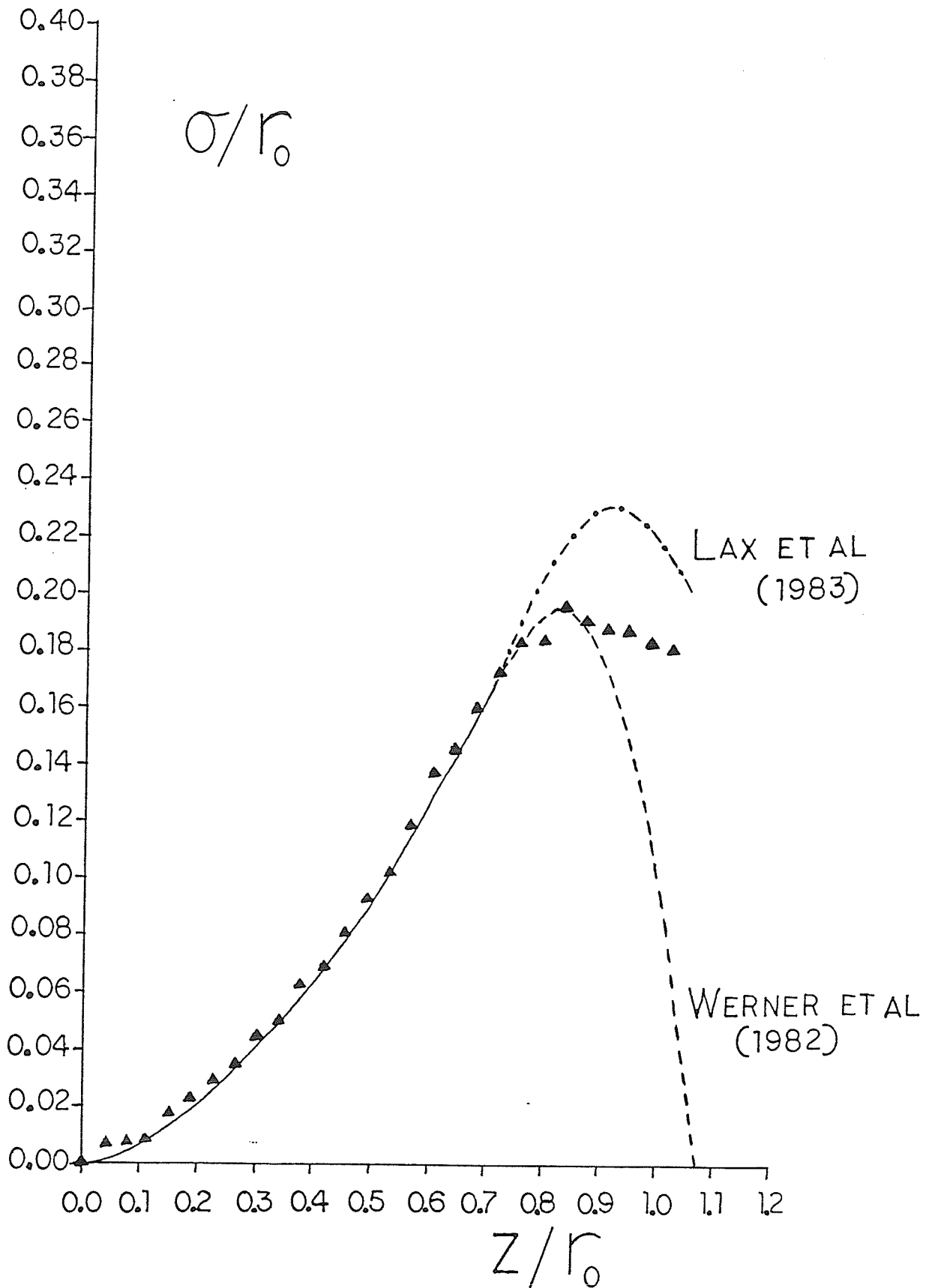


Figure 6.12: Comparison of measured semi-empirical $\sigma(z)$ values in bone-equivalent material for a 16 MeV beam energy with empirical modifications to Fermi-Eyges theory.

BONE : 16 MeV

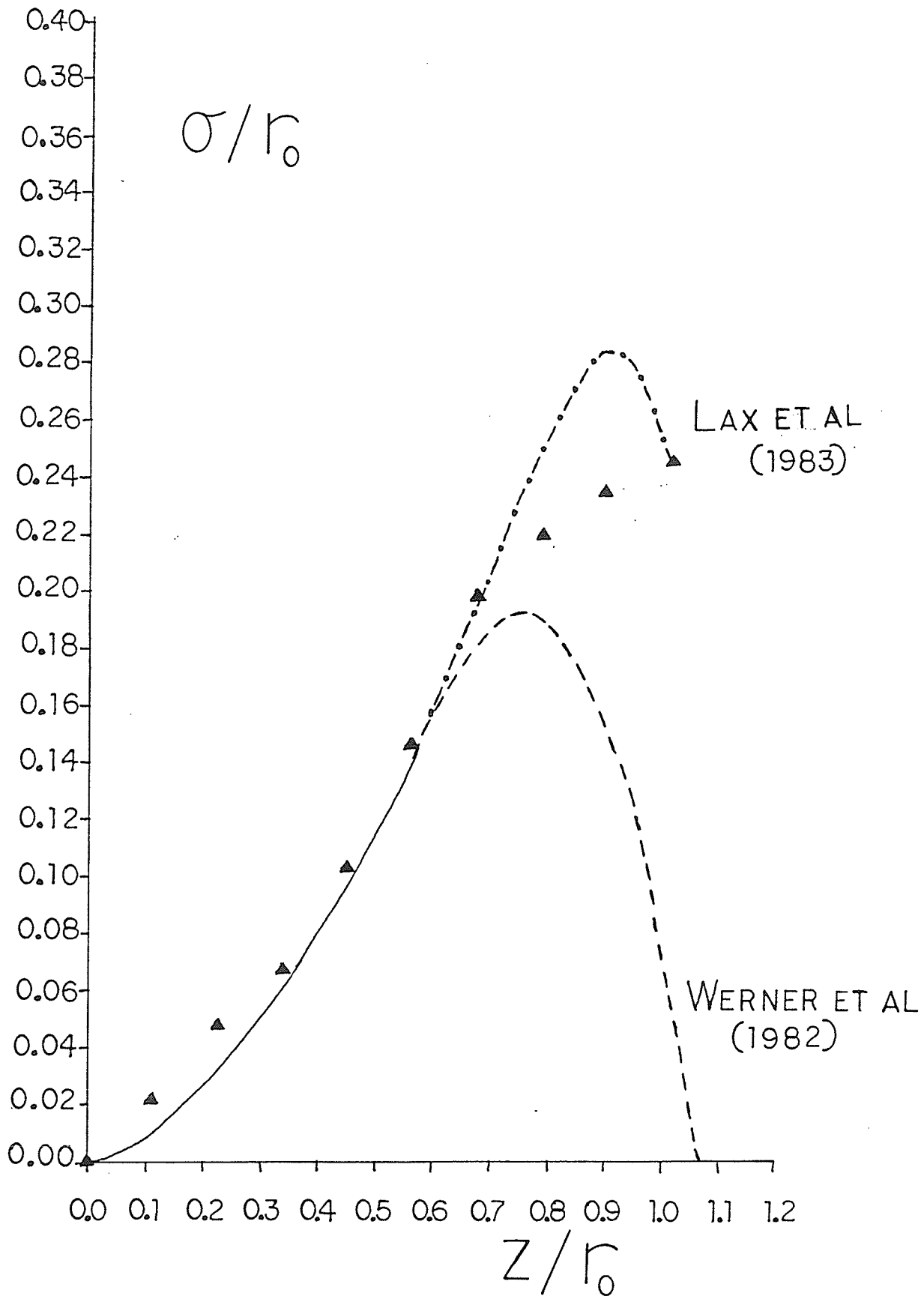
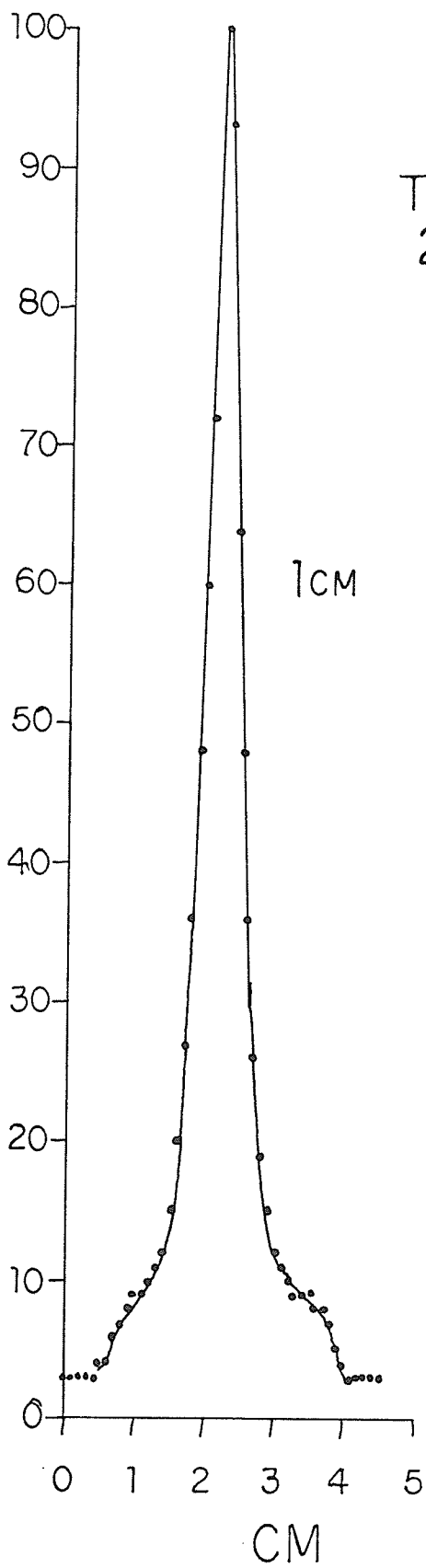
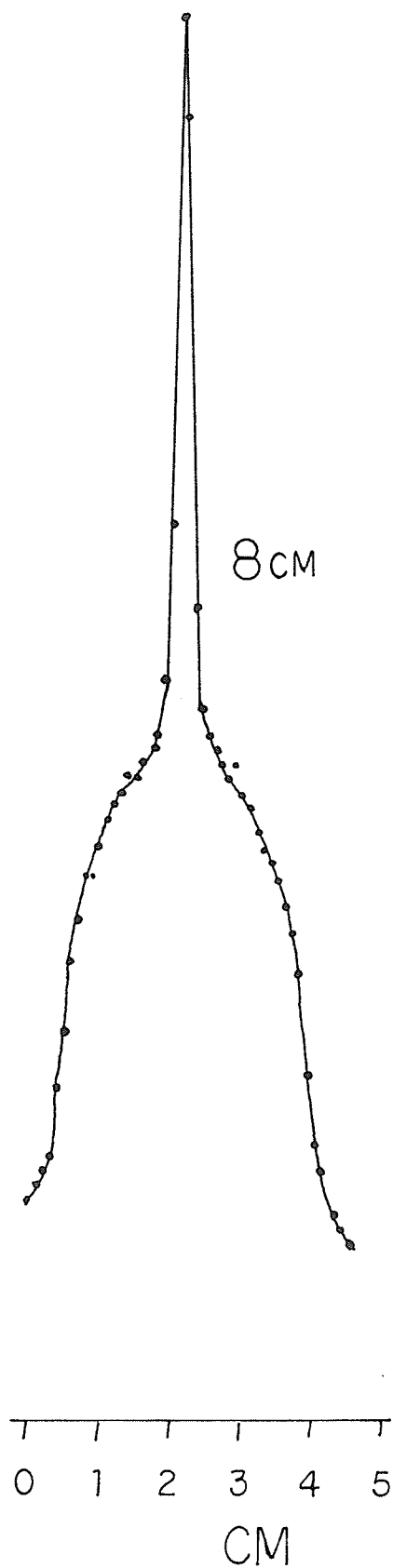


Figure 6.13: Profiles of an empirical pencil beam of 22 MeV energy
at 1 cm and 8 cm depth in temex.

PERCENT OF MAXIMUM



TEMEX
22MEV



8 cm in temex. The pencil beam profile at the 1 cm depth resembles a sharp Gaussian curve with a low photon background. The 8 cm depth profile appears distorted from the Gaussian shape due to the bremsstrahlung dose being relatively important. Figure 6.14 shows the central axis percentage depth dose measured along the pencil beam using a film placed in the parallel orientation. In this figure data points have been interpolated and the distribution represented as a smooth curve. The electron dose falls rapidly leaving a relatively large bremsstrahlung tail beyond the incident electron range. Figure 6.15 shows the values of $\sigma(z)$ derived from the FWHM of the pencil beam profiles and Equation 6.18 up to a depth of 6 cm in temex. Two sets of data points have been provided, one for films in the parallel orientation and the other for films in the perpendicular orientation. The full curve shown in Figure 6.15 is the theoretical variation of $\sigma(z)$ predicted using Fermi-Eyges theory.

6.5 Discussion

The spatial and angular distribution of an electron pencil beam scattering in tissue may be obtained from Fermi-Eyges theory. Limitations to the predictive power of this theory in tissue exist because it ignores electron interactions which are secondary to small-angle multiple scattering. One consequence of

Figure 6.14: Central axis percentage depth dose measured along the pencil beam using film.

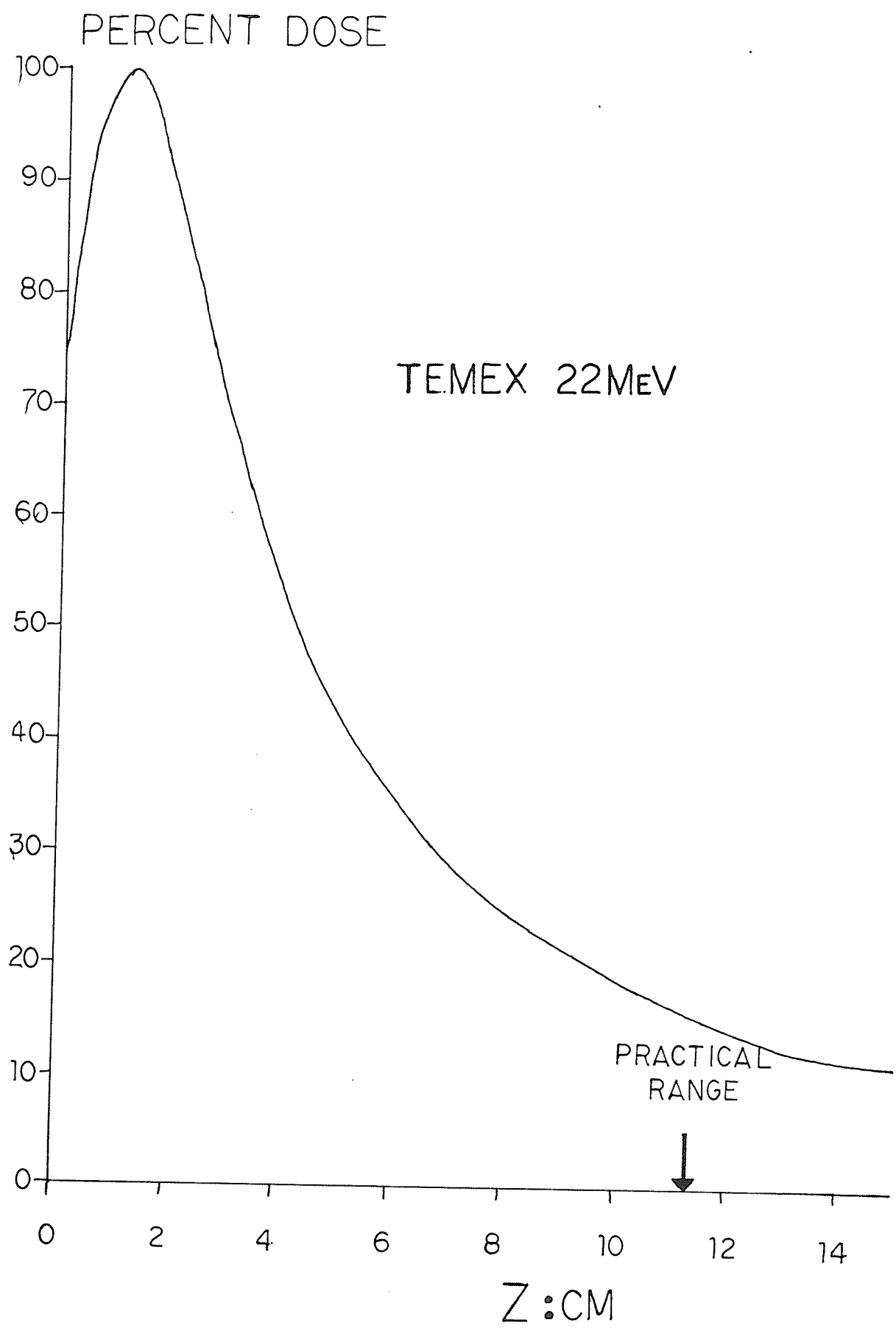
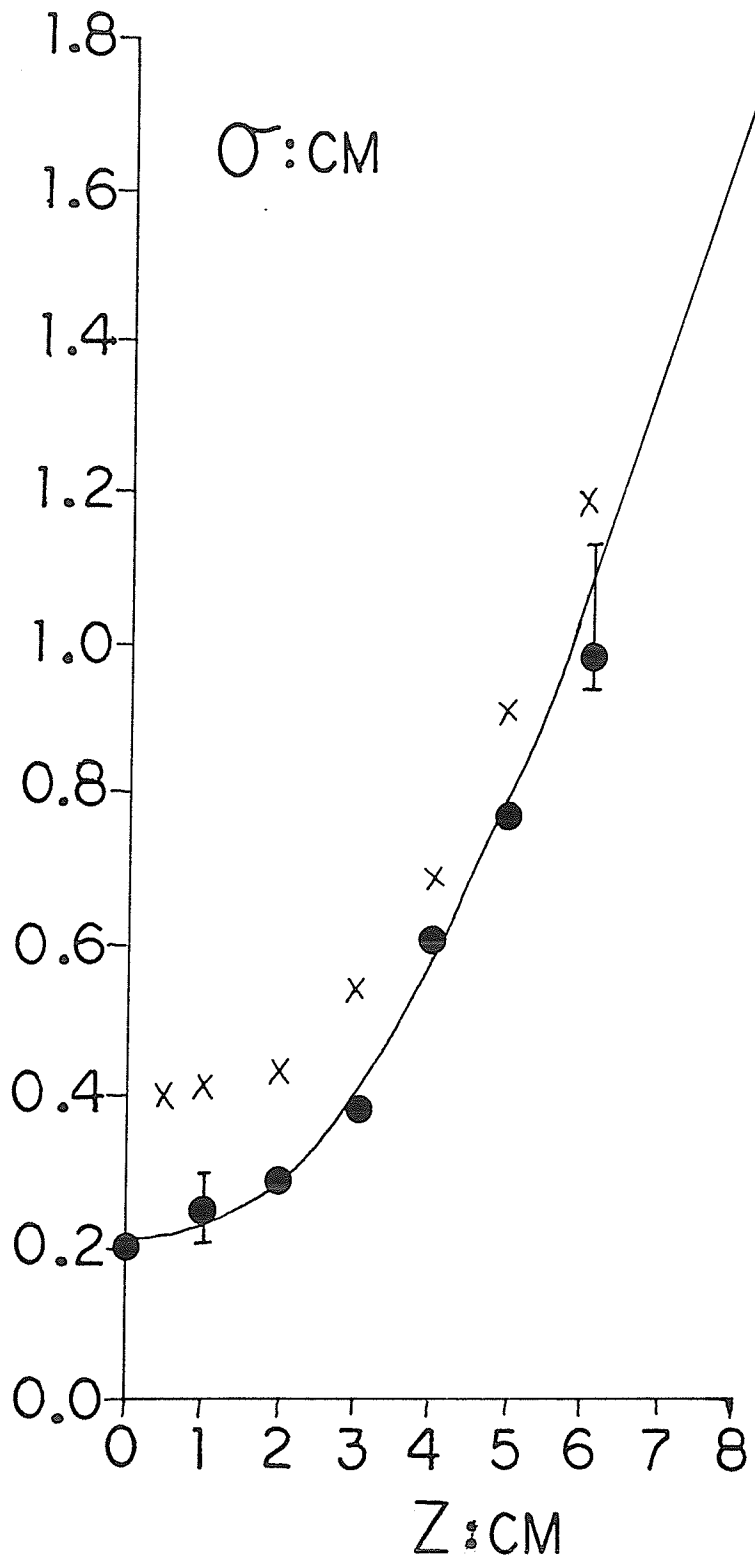


Figure 6.15: Variation of empirical $\sigma(z)$ values with depth z
in temex for a 22 MeV pencil beam.
(X parallel orientation, ● perpendicular orientation)

TEMEX 22MEV



these limitations is that the finite range of an electron must be imposed using an external constraint. This constraint is provided by Harders equation in the approach used here, and therefore theoretical calculations have been terminated in Figures 6.2 and 6.3 at the practical range of the electrons. The constraint does not, however, account for range straggling effects and the theoretical value of pencil beam spread $\sigma(z)$ continues to increase with depth z in the medium until the practical range is reached. The theoretical value of $\sigma(z)$ is a function of the mass angular scattering power of the medium and hence increases with increasing atomic number (Figure 6.2) and decreases with increasing beam energy (Figure 6.3). The theoretical expression for spread of a point monodirectional pencil beam may be generalized to include finite initial spatial and angular distributions for the electron source. This expression is given in Equation 6.1. It is used to compute the components of pencil beam spread in tissue due to scattering in air from the source to the surface of a phantom. Air scattering is an important contribution to the measured spread of the pencil beam in tissue media, as denoted by the non-zero values of σ at the phantom surface in Figures 6.7, 6.8 and 6.9.

Three measurements of the spread of an electron pencil beam have been performed. The semi-empirical method which employs the ratio of central axis doses for small and large square fields

depends upon the difference in shape between the central axis depth dose curves for small and large fields as shown in Figure 6.4. Equation 6.12 requires that the depth dose curves be normalized to their surface value of dose to exclude absolute differences in the incident planar fluence. This normalization also allows depth ionization curves to be legitimately employed in the generation of $\sigma(z)$ values. The dose ratio parameter N is sensitive to the extrapolated value of surface dose used for normalization and direct surface dose measurement should be performed, whenever possible, to minimize this potential systematic error. A typical set of $\sigma(z)$ values generated using Equation 6.13 for a 22 MeV beam incident upon temex are shown in Figure 6.5. The values of $\sigma(z)$ are essentially defined by the dose ratio parameter N . Initially the values of $\sigma(z)$ increase to a maximum which in this instance occurs at a depth of about 0.9 times the CSDA range. This maximum corresponds to the minimum value of the parameter N . The rapid decrease in $\sigma(z)$ values close to the electron range reflects a rise in the value of N toward unity and the values of $\sigma(z)$ after the range are due to bremsstrahlung background.

Figure 6.6 shows that the semi-empirical values of $\sigma(z)$ generated using Equation 6.13 are strongly dependent on the shape of the small field size chosen. The small field length S , according to the derivation of Equation 6.13, must satisfy the

condition $S(o) > 2\sqrt{2}\sigma(o)$ and this imposes a lower limit to the size of the small field chosen. The value of $\sigma(o)$ is an unknown which must be computed assuming the pencil beams are redefined at the level of the collimation system (Chapter 5, Figure 5.2). An upper limit for the length of the small square field size chosen is not set and theoretically at least all appropriate small fields should produce the same values of $\sigma(z)$. This is not the case, as demonstrated in Figure 6.6. The finding is important because it implies that the approach of using only two central axis depth dose curves to obtain values of $\sigma(z)$ is very limited. It should be noted that the derivation of Equation 6.13 implicitly assumes that the incident planar fluence at the phantom surface for both the small and large fields is constant within the field area and zero outside. This condition is not satisfied for field sizes set by the photon collimation system at 100 cm SSD. For small field sizes, the incident beam profile may be sharply peaked. The shape of this profile will change with the field size setting and may to some extent account for the variation of $\sigma(z)$ with the small field size chosen for the calculations. Figure 6.6 also highlights another problem with the central axis dose ratio method. Generating $\sigma(z)$ values is dependent on the differences in depth dose distributions for small and large fields. However, as the beam energy is reduced, lateral scatter equilibrium for the

central axis depth dose occurs at smaller field sizes. Thus for a given small field size, the beam energy for which $\sigma(z)$ values can be generated is limited. This problem is exacerbated by the lower limit imposed on field size $S(o) > 2 \sqrt{2} \sigma(o)$.

Additional sources of error with the central axis dose ratio method for obtaining $\sigma(z)$ values, exist at depths in the phantom corresponding to the dose build-up region. In this region the value of the parameter N is close to, equal or exceeds unity. When N takes a value greater than or equal to unity, the only solutions to Equation 6.9 are $\sigma(z)$ equals zero or $\pm \infty$. For N close to unity, very small changes in N cause large changes in the value of $\sigma(z)$. Therefore, even with accurate dose measurements in the build-up region of the central axis depth dose curves, the values of $\sigma(z)$ generated will have a wide variability.

Ultimately, the use of $\sigma(z)$ parameters in the pencil beam approach to radiotherapy is to predict dose distributions in the patient for any treatment set-up. The limitations to the central axis dose ratio method for generating $\sigma(z)$ values, discussed above, are such that they cannot be used to confidently predict dose distributions with changes in treatment conditions and are therefore practically of little use. For instance, the $\sigma(z)$ values generated using this approach will not accurately predict beam profile penumbra shape since there are large discrepancies between these results and the results of the penumbra

method of generating $\sigma(z)$ values. This problem led Bruinvis et al (1983) to introduce a different set of values for pencil beam spread at field edges to those used for the field centre. This modification is obviously inconsistent with the physics of the pencil beam approach and therefore the method proposed by Bruinvis et al (1983) for dose computation in homogeneous media is very limited in its application.

The semi-empirical penumbra method is shown in Figures 6.7, 6.8 and 6.9 to generate values of $\sigma(z)$ in close agreement with Fermi-Eyges theory up to about 0.7 times the CSDA range, for homogeneous polystyrene, lung-equivalent and bone-equivalent materials respectively. Random errors associated with measurements of penumbra width are relatively large for low beam energies and high density material. For instance, measurements on a 7 MeV beam show a variation in $\sigma(z)$ from the surface value to its maximum value of only 2 millimeters in the bone phantom, and about 4 millimeters in the polystyrene phantom. Since the standard error on $\sigma(z)$ due to measurement of penumbra width is typically a half millimeter and depth position error is another half millimeter, the total error on a given $\sigma(z)$ value relative to the variation of $\sigma(z)$ is large in these materials for low beam energies.

Electron range straggling causes a divergence between the measured and theoretical data shown in Figures 6.7, 6.8 and 6.9

at depths greater than about 0.7 times the CSDA range. At present there is no theoretical modification to Fermi-Eyges theory which accounts for range straggling. However, Werner et al (1982) considered all electrons scattered to angles greater than $\pi/4$ to be lost from the beam and after subtracting the bremsstrahlung background achieved good agreement with their measured data (Equation 6.6). Lax et al (1983) used Monte Carlo data for pencil beams of electrons on water to obtain an empirical multiplicative modification factor which is used to reduce the value of $\sigma(z)$ at large depths (Equation 6.7). Figure 6.10 compares the suggested modifications of Werner et al (1982) and Lax et al (1983) to Fermi-Eyges theory and the measured data for a 22 MeV beam in polystyrene. The air-scattering components to the measured data have been subtracted in order to make the comparison valid for an initially point monodirectional beam. The Werner et al (1982) modification is suggested for a bremsstrahlung subtraction of the data. This has not been performed for our measured data and therefore agreement may only be reasonably expected up to a depth of 0.9 times the CSDA range. Both modifications therefore give good agreement with the measured data for this particular beam energy and medium.

A change of media density to lung is seen from Figure 6.11 to cause the Lax et al (1983) modification to overestimate the measured data, whereas the Werner et al (1982) approach is still

able to predict the measured variation. However, for a change in both density and atomic number both empirical modifications appear to be unable to adequately predict the measured variation. This indicates that the approaches of Werner et al (1982) and Lax et al (1983) are limited and that a more sophisticated approach to range straggling effects is required.

Use of the semi-empirical penumbra method to derive values of pencil beam spread in homogeneous media does not suffer serious limitations, such as those encountered for the central axis dose ratio method. The penumbra method therefore offers potential for developing a model based on Fermi-Eyges theory which will have good predictive power in both homogeneous and inhomogeneous media for changes in treatment conditions such as beam energy, SSD, field size and angle of incidence of the beam to the patient surface.

The third experimental method of measuring pencil beam spread in tissue was to examine beam profiles of an empirical pencil beam of 22 MeV beam energy incident upon temex. Production of an empirical pencil beam is relatively simple, since only a small hole bored through a thick lead block is all that is required. However, accurately measuring the pencil beam spread from such an arrangement is beset with experimental difficulties. One practical difficulty is that high given doses for the 4 cm x 4 cm square field irradiating the pinhole are required

to achieve optical densities in the linear region of the film used to measure beam profiles. Figure 6.13 shows that the electron pencil beam profile resembles a sharp Gaussian function at shallow depths. However at depths over about half the range of the incident electrons, collimator produced bremsstrahlung contributes a significant part of the dose at large radii. Also at large depths, the bremsstrahlung produced in the phantom forms a sharp central peak to the dose profile of the pencil beam. The relative importance of the bremsstrahlung background at large depths for electron pencil beams may be understood by examining Figure 6.14. The central axis dose for the pencil beam falls rapidly due to the uncompensated lateral scatter of the electrons, whereas the bremsstrahlung is restricted to a narrow forward cone and begins to dominate at large depths. Accurate subtraction of the bremsstrahlung background is problematical. An approximate method suggested by McParland and Cunningham (1986) is to plug the pinhole and remeasure the profile, then subtract this from the original. This approach overcompensates the central phantom produced bremsstrahlung and therefore has not been attempted here. Instead, measurements of pencil beam spread $\sigma(z)$ are only quoted for depths up to about 0.5 times the range in temex. This corresponds to the region in which the total bremsstrahlung background is considered relatively low. The measured values of pencil beam spread derived from the FWHM

of the profiles using Equation 6.18 and shown in Figure 6.15, compared favorably to the theoretical predictions of Fermi-Eyges theory when the film is placed in the perpendicular orientation. However, unexpectedly, repeat measurements with the film placed parallel to the beam do not agree with the perpendicular orientation results. This discrepancy is probably due to a parallel film orientation acting as a large perturbation to the electron field of such a small pencil beam and thereby producing a large systematic error. These data are only preliminary and further work is required to assess the adequacy of this empirical approach for the determination of electron pencil beam spread in tissue. However, the results do indicate potential experimental difficulties which require resolution and future researchers should be aware of these problems.

6.6 Conclusions

Three experimental methods of deriving electron pencil beam spread in tissue have been investigated with comparison to the theoretical predictions of Fermi-Eyges theory. The semi-empirical central axis dose ratio method has been shown to give unreliable results at depths in tissue corresponding to the build-up region of the central axis depth dose. For a given small field size the energy at which $\bar{\sigma}(z)$ values can be generated is limited due to lateral scatter equilibrium on the central axis of the small field. Furthermore, the values of $\bar{\sigma}$

(z) generated using this method are strongly dependent upon the small field size chosen. This variation with small field size is unexpected and is probably due to the changing incident planar fluence distribution at the phantom surface with field size setting. These results suggest that the use of central axis depth dose ratios to generate values of $\sigma(z)$ is very limited. The values of $\sigma(z)$ generated by this method cannot be used to predict beam profile shape or make predictions for the central region of the field for changes in treatment conditions.

The use of the semi-empirical penumbra method to generate values of the pencil beam spread parameter $\sigma(z)$ does not suffer from major shortcomings. Results are derived which give good agreement with Fermi-Eyges theory up to 0.7 times the incident electron range for bone, lung and muscle-equivalent media. Range straggling modifications to Fermi-Eyges theory suggested by Werner et al (1982) and Lax et al (1983), for depths approaching the incident electrons range have been shown to have limited predictive power. Neither modification is universally satisfactory for the range of tissue densities and atomic numbers encountered in patients. These results suggest that an empirical modification to Fermi-Eyges theory should be a function of both density and atomic number of the medium. However, empirical approaches to range straggling will still be limited in inhomogeneous media and alternative theoretical modifications to Fermi-Eyges theory to account for range straggling require development.

Empirically producing an electron pencil beam using lead collimation is simple but accurate measurement of the spread parameter $\sigma(z)$ from such a beam is experimentally problematical. Only provisional results have thus far been obtained, however, subtraction of the large bremsstrahlung background from electron dose at depths over the second half of the incident electrons range poses a major difficulty for this technique. In addition, because empirical pencil beams are so small, film should be used as the detector to maximize resolution. The film should be placed in the perpendicular rather than parallel orientation to avoid large perturbations of the electron field.

Fermi-Eyges theory is limited in tissue due to its neglect of interaction processes secondary to small-angle multiple scattering. The semi-empirical penumbra method of deriving values of the pencil beam spread parameter σ offers a simple and reliable experimental technique which potentially can be used to develop algorithms which improve upon the predictive power of Fermi-Eyges theory in tissue for changes in treatment conditions such as beam energy, SSD, field size and beam obliquity.

Chapter 7
CONCLUSIONS

7.1 Conclusions

The Fermi theory of electron transport (Rossi and Greisen 1941, Brahme 1975) is simple and accounts for the main electron scattering interaction mechanism of small-angle multiple scattering. The spatial and angular distribution of electrons as they penetrate tissue may be calculated with this theory and energy loss by the electrons may be included into the formalism using the solution derived by Eyges (1948). The predictions of this theory for dose from therapeutic electron beams scattering in air is excellent. However, Fermi-Eyges theory is limited since it ignores the interaction mechanisms which are secondary to small-angle multiple scattering. These secondary interactions include electron absorption, delta-ray production, bremsstrahlung production, range straggling, large-angle single scattering events and backscattering.

Although negligible in air, the secondary interaction mechanisms make important contributions to the spatial distribution of dose in tissue. Modification of Fermi-Eyges theory is therefore required to include secondary interaction effects. These modifications must be provided by a theoretical development of the basic theory since the ultimate aim is to accurately compute dose in a medium with 3-dimensional inhomogeneities (i.e. a patient), and for such calculations empirical data is of limited value. Recent progress toward this goal has been provided by: the expan-

sion of multiple scattering theory to second order (Jette 1985, Bielajew and Jette 1986) which describes the increasing skewness of the electron path with depth in a scattering medium, the removal of the semi-infinite slab approximation for calculations in inhomogeneous media (Storchi and Huizenga 1985, Jette 1986b) and an attempt to include range straggling into the Fermi-Eyges formalism (Bruinvis 1987).

This study has demonstrated that modelling the therapeutic electron beams from the Sagittaire Therac 40 accelerator as a collimated isotropic source of electrons has excellent predictive power in the air space above patients. The source is considered coincident with the exit window of the accelerator and a thick lead collimator is assumed equivalent to an infinitely thin absorbing plate whose location corresponds to the top, centre and bottom of the thick block when the angle the face of the block makes with the central axis of the beam is positive, zero or negative respectively.

In air, the predictions of beam profile shape for any beam energy, SSD and field size do not require any empirical input data when the field edge is formed by a single collimator. However, when the field edges are formed by a double collimator an empirical, field-size dependent perturbation factor must be introduced for good agreement between measured and predicted data. This is because the upper collimator of the double colli-

mator system restricts the field and hence perturbs the mean square angle of travel of the electrons incident on the lower collimator from the isotropic value predicted in the single collimator case. It is notable that the introduction of an empirical perturbation factor to account for this effect, scales with both energy and SSD.

In addition to predictions of beam profile shape, the collimated isotropic source model is able, for a fixed field size, to predict within 5% changes in beam output with SSD or beam energy. The increase in the FWHM of beam profiles above the FWHM expected on geometrical grounds at small field sizes and low beam energies may also be predicted. These effects are satisfactorily described by lateral scatter disequilibrium and the accuracy of the predictions demonstrates that the use of a "virtual" source concept for magnetically scanned electron beams is redundant.

Several experimental methods of obtaining values of pencil beam spread, $\sigma(z)$, in tissue were investigated in this study and compared to the predictions of Fermi-Eyges theory. These methods utilized a pinhole collimator, central axis depth dose data and the penumbra formed by the edge of a lead collimator respectively. It was found for all methods that the empirical subtraction of bremsstrahlung dose from electron dose was problematical, especially for the pinhole method and may lead to large systematic errors in the measured values of pencil beam spread. Each of

the experimental methods of determining the pencil beam spread parameter $\bar{\sigma}(z)$ have inherent limitations leading to possible systematic errors, and future researchers should be aware of these shortcomings. Of the three experimental approaches investigated the penumbra method of determining pencil beam spread is recommended as the easiest and most reliable method which gives accurate results over most of the electron range in tissue.

As the therapeutic electron beams enter tissue, interaction mechanisms which are secondary to small-angle multiple scattering become important and a breakdown in the predictions of Fermi-Eyges theory is expected. The determination of $\bar{\sigma}(z)$ values in homogeneous muscle, lung and bone-equivalent media using the penumbra method demonstrate that the collimated isotropic source model makes accurate predictions of the dose distribution in all homogeneous biological materials at depths up to about 0.7 times the electron range. At greater depths the model overestimates the experimental data to a large degree due to the neglect of electron range straggling by Fermi-Eyges theory. A comparison of the experimental data with the empirical modifications of Fermi-Eyges theory suggested by Werner et al (1982) and Lax et al (1983) to include range straggling effects reveal that neither modification is universally good for the range of therapeutic electron energies and homogeneous tissue-equivalent media

investigated. Future work will investigate the range straggling effect further.

The overall objective of this work has been to investigate and develop pencil beam methods of electron dose computation to achieve a ± 5% dose accuracy in cancer patients with a minimal amount of experimental input data. To achieve this goal a great deal more theoretical development work is required. However, the collimated isotropic source model presented and verified in this thesis has provided an essential component to electron dose computation algorithms and indicates the areas in which work should be concentrated for future progress.

REFERENCES

1. AAPM (1983): A protocol for the determination of absorbed dose from high-energy photon and electron beams. Med. Phys. 10(8):741-771.
2. Abou-Mandour, M and Harder, D. (1978): Berechnung der dosisverteilung schneller elektronen und hinter gewetse in homogenitaten beliebiger breite. Strahlentherapie 154:546-553.
3. Abou-Mandour M., Nusslin F. and Harder D. (1983): Characteristic functions of point monodirectional electron beams. Acta Radiol. Suppl. 364:43-48.
4. Almond, P., Wright, A. and Boone, M. (1967): High-energy electron dose perturbations in regions of tissue heterogeneity. Part II - Physical models of tissue heterogeneities. Radiology 88:1146-1153.
5. Andreo, P. and Brahme, A., (1981): Mean energy in electron beams. Med. Phys. 8:682-687.
6. Andreo, P. and Brahme, A. (1984): Restricted energy-loss stragglng and multiple scattering of electrons in mixed Monte Carlo procedures. Rad. Res. 100:16-29.
7. Andreo, P. (1985): Lecture 4, the interaction of electrons with matter II scattering. In the computation of dose distributions in electron beam radiotherapy p.56: A.E. Nahum (Ed.) Umea University. ISBN 91-7174-177-1.

8. Andreo, P. (1985b): Lecture 8, Broad beam approaches to dose computation and their limitations. In the computation of dose distributions in electron beam therapy p.128: A. E. Nahum (Ed.) Umea University ISBN91-7174-177-1.
9. Aucouturier, J., Huber, H. and Jaoven, J. (1970): Systeme de transport du Faisceau d'electrons dans le sagittaire. Revue Technique Thompson-CSF 2(4), 655-680.
10. Awadi, I. (1957): Penetration of electron beams into water below the critical energy. Phys. Rev. 107:1476-1482.
11. Ayyangar, K., Ting, J. and Suntharalingam, N. (1978): Surface contour and inhomogeneity corrections in electron beam treatment planning, Med. Phys. 5:345 (Abstract).
12. Ayyangar, K., Leonard, C., and Sunthralingham, N. (1980): Computerization of electron beams for treatment planning. Med. Phys. 7:440 (Abstract).
13. Bagne, F. (1976): Electron beam treatment-planning system. Med. Phys. 3:31-38.
14. Bakker, D., Kersten, C., Crommelin, M., Van Panthaleon Van Eck, R., and Van Overbeek, P. (1983): Evaluation of an electron beam calculation model. Medicamundi 28:4522 984 54001/772.
15. Banford, A. (1966): The Transport of Charged Particle Beams. E. and F. N. Spon. Limited Press, London.

16. Berger, M. and Seltzer, S. (1969): Calculation of energy and charge deposition and of the electron flux in a water medium bombarded with 20 MeV electrons. Ann. N.Y. Acad. of Sci. 161:8-23.
17. Berger, M. and Seltzer, S. (1978): The influence of scattering foils on absorbed dose distributions from electron beams. NBS-IR 78-1552 (National Bureau of Standards, Washington, D.C.).
18. Berger, M. and Seltzer, S. (1982): Tables of energy distribution in water phantoms irradiated by point monodirectional electron beams with energies from 1 to 60 MeV and applications to broad beams. NB51R:82-2451.
19. Bethe, H. (1933): Quantenmechanik der einund physik 24/2, Quantentheorie, Geiger, H. and Schael, K., Eds. (Springer-Verlag, Berlin).
20. Bethe, H., Rose, M. and Smith, L. (1938): The multiple scattering of electrons. Proc. Am. Phil. Soc. 78:573-585.
21. Bielajew, A. and Jette, D.(1986): Monte Carlo evaluation of second-order multiple scattering theory. Med. Phys. 13(4): 588 (Abstract).
22. Blunck, O. and Westphal, K. (1951): Zum Energieverlust energiereicher Elektronen in dunnen Schichten Z. Phys. 130:641.
23. Boone, M., Jardine, J., Wright, A., and Tapley, N. (1967): High energy dose perturbations in regions of tissue heterogeneity Part I - In vivo dosimetry. Radiology 88:1136-1145.

24. Boone, M., Almond, P., and Wright, A. (1969). High-energy electron dose perturbations in regions of tissue heterogeneity. *Ann. N.Y. Acad. of Sci.* 161:214-231.
25. Brahme, A. (1971): Multiple Scattering of relativistic electrons in air. TRITA-EPP-71-22 (1971).
26. Brahme, A. (1975): Simple relations for the penetration of high energy electron beams in matter. National Institute of Radiation Protection, Stockholm, Report SSI: 1975-011.
27. Brahme, A. and Svenson, H. (1976). Specification of electron beam quality from the central axis depth absorbed dose distribution. *Med. Phys.* 3:95-
28. Brahme, A., Kraepelien, T., and Svensson, H. (1980): Electron and photon beams from a 50 MeV racetrack microtron. *Acta Radiol. Oncol.* 19:305-319.
29. Brahme, A. (1981): Physics of electron beam penetration, fluence and absorbed dose. Proceedings of the symposium on electron dosimetry and arc therapy. B. Paliwal Ed. AAPM 0-88318-404-4.
30. Brahme, A., Lax, I. and Andreo, P. (1981): Electron beam dose planning using discrete gaussian beams - mathematical background. *Acta Radiol. Oncol.* 20:147-158.
31. Brahme, A. (1983): Geometric parameters of clinical electron beams .pll in Computed electron beam dose planning. *Acta Radiol. Suppl.* 364.

32. Brahme, A. and Lax, I. (1983): Absorbed dose distribution of electron beams in uniform and inhomogeneous media. *Acta Radiol. Suppl.* 364:61-79.
33. Brahme, A. and Nilsson, B. (1984): Limitations of pencil beam algorithms in electron beam dose planning. *Proc. of the Eight Int. Conf. on the Use of Computers in Radiation Therapy:* 157-160.
34. Brahme, A. (1985): Current algorithms for computed electron beam dose planning. *Radiotherapy and Oncology* 3: 347-362.
35. Briot, E. and Dutreix, A. (1976): Dosimetrie des faisceaux d'electrons de haute energie d'un accelerateur lineaire. *J. Radiol. Electrol.* 57(5):447-454.
36. Bruinvis, I., Van Amstal, A., Elevelt, A. and Van der Laarse, R. (1983): Calculation of electron beam dose distribution for arbitrarily shaped fields. *Phys. Med. Biol.* 28:667-683.
37. Bruinvis, I. (1987): Electron beams in radiation therapy collimation, dosimetry and treatment planning. Ph.D. Thesis University of Amsterdam.
38. Budge, R. (1981): Oblique incidence corrected electron isodose curves from the modified Kawachi formula. *Australas. Phys. Eng. Sci. Med.* 4:10-14.
39. Case, K.M. and Zweifel, P. (1967): *Linear transport theory* Addison-Wesley Press.

40. Cecatti, E., Goncalves, J., Cecatti, S. and da Penha Silva, M. (1983): Effect of the accelerator design on the position of the effective electron source. *Med. Phys.* 10:683-686.
41. Cercignani, C. (1975): Theory and application of the Boltzmann equation, Scottish Academic Press.
42. Cygler, J., Battista, J., Scrimger, J., Mah, E., and Antolak, J. (1987): Electron dose distributions in experimental phantoms. A comparison with 2D pencil beam calculations. Accepted for publication by *Phys. Med. Biol.*
43. Czaikowsky, P. (1972): Experimentelle untersuchung and mathematische approximation der teFerdosis venteilung schneller elektronen. 2. Mitteilung. *Strahlentherapie* 143:416-423.
44. Dahler, A., Baker, A. and Laughlin, J. (1969). Comprehensive electron-beam treatment planning. *Ann. N.Y. Acad. of Sci.* 161:198-213.
45. Edwards, F. and Coffey, C. (1979): A cumulative normal distribution model for simulation of electron beam profiles. *Int. J. Radiation Oncology Biol. Phys.*, 5: 127-133.
46. Eisen, H., Rosenstein, M. and Silverman, J. (1972): Electron depth-dose distribution measurement in two-layer slab absorbers. *Radiat. Res.* 52:429-447.
47. Eisenhauer, C. (1979). Model for diffusion of a narrow beam of charged particles. *Radiat. Res.* 81:336-354.

48. Ekstrand, K, and Dixon, R. (1982): The problem of obliquely incident beams in electron-beam treatment planning. Med. Phys. 9:276-278.
49. Eyles, L. (1948): Multiple scattering with energy loss. Phys. Rev. 74:1534-1535.
50. Fehrentz, D., Liebig, B. and Schroder-Babo, P. (1976): Berucksichtigung grosser inhomogenitatsbereiche bei der berechnung von elektronen-dosis verteilungen, Strahlentherapie 151:423.
51. Fehrentz, D. (1977): Methods to calculate electron dose distributions in computers in radiation therapy. p596-599. Proc. of the sixth International Conf. on the use of computers in radiation therapy, Göttingen Federal Republic of Germany. U. Rosenow (Ed).
52. Fehrentz, D., Kinimig, B., Ihnen, E., and Schroder-Babo, P. (1979): Ein analytisches verfahren zur berechnung von electron-endosisverteilungen I. Strahlentherapie 155:316-323.
53. Fermi, E. (1941): Cited by Rossi, B. and Greisen, K., Cosmic ray theory. Rev. Med. Phys. 13:265-268.
54. Goitein, N.(1978): A technique for calculating the influence of thin inhomogeneities on charged particle beams. Med. Phys., 5(4): 258-264.
55. Goitein,N. and Sisterson,J. (1978): The influence of thick inhomogeneities on chareged particle beams. Radiation Research 74: 217-230.

56. Goitein, M., Chen, G., Ting, J., Schneider, R., and Sisterson, J.
Measurements and calculations of the influence of thin inhomogeneities on charged particle beams. Med. Phys. 5(4): 265-273.
57. Harder, D. (1965): Energiespektren schneller elektronen in verschiedenen tiefen p.260. In Zuppringer, A.L.G. Poretti (eds) Symposium of high energy electrons - Montreux, 1964. Springer-Verlag, Berlin.
58. Harder, D. and Abou-Mandour, M. (1976): Berechnung der dosisverteilung schneller elektronen in und hinter gewebein - homogenitaeten beliebsiger breite. Strahlentherapie 152:509-516.
59. Hogstrom, K., Mills, M., and Almond, P. (1981): Electron beam dose calculations. Phys. Med. Biol. 26:445-459.
60. Hogstrom, K. (1982): Electron beam modelling and dose calculating algorithms in treatment planning computers. Med. Phys. 9:645-653.
61. Hogstrom, K. and Almond, P. (1982): The effect of multiple scattering on dose measured in non-water phantoms. Med. Phys. 9:607 (Abstract).
62. Hogstrom, K., Mills, M., Meyer, J., Palta, J, Mellenberg, D., Meoz, R., and Fields, R. (1984). Dosimetric evaluation of a pencil-beam algorithm for electrons employing a two-dimensional heterogeneity correction. Int. J. Radiat. Oncol. Biol. Phys. 10:561-569.

63. Hogstrom, K. (1985): AAPM refresher course; evaluation of electron pencil beam dose calculation. Med. Phys. 12:554. (Abstract).
64. Holt, J., Mohan, R., Caley, R., Buffa, A., Reid, A., Simpson, L. and Laughlin, J. (1978): Memorial electron beam AET treatment planning system. p70 in practical aspects of electron beam treatment planning. Medical Physics Monograph No. 2. AAPM, Orton, D. and Bagne F. (eds). American Institute of Physics Publication, N.Y.
65. Huizenga, H. and Storchi, P. (1986a): Scattering of clinical electron beams in air. Med. Phys. (Abstract).
66. Huizenga, H. (1986b): Fermi-Eyges theory, internal report, Rotterdam Radiotherapy Institute, June 1986.
67. Huizenga, H. and Storchi, P. (1987): The in-air scattering of clinical electron beams as produced by accelerators with scanning beams and diaphragm collimators. Submitted to Phys. Med. Biol.
68. ICRU (1970): International Commission of Radiation Units and Measurements, Linear energy transfer. ICRU Report 16 (Bethesda, Maryland).
69. ICRU (1972): International Commission on Radiation Units and Measurements, Radiation dosimetry, Electron beams with energies between 1 and 50 MeV: ICRU Report 21 (Bethesda, Maryland).

70. ICRU (1976) International Commission on Radiation Units and Measurements, Determination of absorbed dose in a patient irradiated by beams of X or gamma rays in radiotherapy procedures. ICRU Report 24 (Bethesda, Maryland).
71. ICRU (1980): International Commission on Radiation Units and Measurements. Radiation quantities and units. ICRU Report 33 (Bethesda, Maryland).
72. ICRU (1984a): International Commission on Radiation Units and Measurements, Radiation dosimetry, Electron beams with energies between 1 and 50 MeV: ICRU Report 35 (Bethesda, Maryland).
73. ICRU (1984b): International Commission of Radiation Units and Measurements, Stopping Powers for electrons and positrons. ICRU Report 37 (Bethesda, Maryland).
74. Jackson, J.D. (1975): Classical Electro-Dynamics 2nd Edition (Wiley, New York).
75. Jette, D., Lanzl, H., Rosenfeld, M. and Pagnamenta, A. (1981): Analytic representation of electron central-axis depth dose data. Med. Phys. 8:877-881.
76. Jette, D. and Pagnamenta, A. (1982): Electron multiple scattering distribution from a point source. Phys. Med. Biol. 27(2): 308-310.
77. Jette, D., Pagnamenta, A., Lanzl, L. and Rosenfeld, M. (1983): The application of multiple scattering theory to therapeutic electron dosimetry. Med. Phys. 10:141-146.

78. Jette, D. (1984): The problem of electron dose calculation: II. Inhomogeneities and beam shaping. AAMD Journal 9(4): 12-17.
79. Jette, D. (1985): Second-order multiple-scattering theory for charged-particle teletherapy beams. Med. Phys. 12:178-182.
80. Jette, D., Pagnamenta, A., Kao, M., Lanzl, L., and Rosenfeld, M. (1985): Secondary effects in electron beams. Med. Phys. 12:515 (Abstract).
81. Jette, D. (1986a): General solution to the Fermi equation. Unpublished work.
82. Jette, D. (1986b): Application to a thick half-slab of the general solution to the Fermi equation. Unpublished work.
83. Johns, H. and Cunningham, J. (1984). The physics of radiology, 4th Edition (Springfield Illinois).
84. Kawachi, K. (1975): Calculation of electron dose distribution for radiotherapy treatment planning. Phys. Med. Biol. 20: 571-577.
85. Kessarlis, N. (1964): Calculated absorbed dose for electrons. Radiat. Res. 23:630-640.
86. Kessarlis, N. (1966): Penetration of high energy electron beams in water. Phys. Rev. 145:164-174.
87. Kessarlis, N. (1970): Spectra of high energy electron beams in water. Radiat. Res. 43, 281-287.

88. Khan, F. and Lee, J. (1979): Computer algorithm for electron beam treatment planning. *Med. Phys.* 6:142-144.
89. Koch, H. and Motz, J. (1959): Bremsstrahlung cross section formulas and related data. *Rev. Mod. Phys.* 31:921-984.
90. Kozlov, A. and Shishov, V. (1982): Calculation of high-energy dose distributions in tissue equivalent media. 1. Determination of the dose function of point unidirectional sources. *Strahlentherapie* 158:298-304.
91. Landau, L. (1944): On the energy loss of fast particles by ionisation. *J. Phys. USSR* 8:201-205.
92. Laughlin, J., Ovodia, J., Beattie, J., Henderson, W., Harvey, R. and Haas, L. (1953): Some physical aspects of electron beam therapy. *Radiology* 60:165-185.
93. Laughlin, J. (1965): High energy electron treatment planning for inhomogeneities. *Brit. J. Radiol.* 38:143-147.
94. Laughlin, J., Lundy, A., Phillips, R., Chu, F. and Sattar, A. (1965): Electron beam treatment planning in inhomogeneous tissue. *Radiology* 85:524-531.
95. Lax, I. and Brahme, A. (1980): Collimation of high energy electron beams. *Acta Radiol. Oncol.* 19:199-207.
96. Lax, I., Brahme, A. and Andreo, P. (1983): Electron beam dose planning using gaussian beams: improved radial dose profiles. *Acta Radiol. Suppl.* 364:49-59.

97. Lax, I. and Brahme, A. (1985): Electron beam dose planning using Gaussian beams. Energy and spatial scaling with inhomogeneities. Acta Radiol. Oncol. 24:75-85.
98. Lax, I. (1985) A generalised gaussian model for the electron beam dose planning. pp.191-209 in The computation of dose distributions in electron beam radiotherapy. Dept. of Radiation Physics, University of Umea, S-901 85 Umea, Sweden 1985 (ed. Nahum, A.).
99. Lax, I. (1986): Inhomogeneity corrections in electron-beam dose planning. Limitations with the semi-infinite slab approximation. Phys. Med. Biol. 31: 879-892.
100. Lewis, H. (1950): Multiple scattering in an infinite medium. Phys. Rev. 78:526-542.
101. Liaw, J. (1977): Calculation of high energy radiotherapeutic electron field. In: Proc. of 4th Conf on Scientific and Industrial Applications of Small Accelerators, Denton, 27-29 August 1976. IEEE, New York: 526-528.
102. Lillicrap, S., Wilson, P., and Boag, J. (1975): Dose distributions in high energy electron beams: Production of broad beam distributions from narrow beam data. Phys. Med. Biol. 20:30-38.
103. Loyd, M. and Rosen, I. (1985): Calculation of output from irregularly shaped electron beams. Med. Phys. 12(4): 505 (Abstract).

104. Luo, Z-M. (1982): A method for calculating electron energy deposition in thick media. *Radiat. Res.* 92:1-18.
105. Marion, J. and Zimmerman, B. (1967): Multiple scattering of charged particles. *Nucl. Inst. Meth.* 51:93-105.
106. Markus, B. (1964): Beitrage zur Entwicklung der Dosimetrie Schneller Elektronen. *Strahlentherapie* 124: 33-53.
107. McKenzie, A. (1979): Air-gap correction in electron treatment planning. *Phys. Med. Biol.* 24:628-635.
108. McKinley, W. and Feshback, H. (1948): *Phys. Rev.* 74:1759-1772.
109. Millan, P., Millan, S., Hernandez, A. and Andreo, P. (1979): Parameterization of linear accelerator electron beam for computerized dosimetry calculations. *Phys. Med. Biol.* 24: 825-826.
110. McParland, B. and Cunningham, J. (1986): A phenomenological approach to a pencil beam algorithm for electrons. *Med. Phys.* 13(4): 581 (Abstract).
111. Moller, C. (1932): Zur theorie des durchgangs schneller elektronen durch materie. *Ann. Phys.* 14:531-544.
112. Mott, N. (1929): The scattering of fast electrons by atomic nuclei. *Proc. Royal Society London A*124:425-437.
113. Mott, N. (1932): The polarization of electrons by double scattering. *Proc. Royal Society London A*135:429-442.

114. Nath, R., Gignac, C., Agostinelli, A., Rothberg, S. and Schultz, R. (1980): A semi-empirical model for the generation of dose distributions produced by a scanning electron beam. *Int. J. Radiat. Oncol. Biol. Phys.* 6:67-73.
115. Nigam, B., Sundaresan, M., and Wu, T., (1959): Theory of multiple scattering. Second Born approximation and corrections to Moliere's work. *Phys. Rev.* 115:491-511.
116. Nilsson, B. and Brahme, A. (1986): Electron contamination from photon beam collimators. *Radiotherapy and Oncology* 5:235-244.
117. Nusslin, F. (1979): Computerized treatment planning in therapy with fast electrons: a review of procedures for calculating dose distributions. *Medicamundi* 24:112-118.
118. Nusslin, F. (1980): A simple model for calculating dose distributions in high-energy electron therapy. *J. Eur. Radiother.* 1:193-197.
119. Osman, G. (1976): Dose distribution of therapeutic electron beams and automation of treatment planning. *Journal of Medicine* 7:143-167.
120. Osman, G. (1977): Decrement curves in therapeutic electron beams and their use in medical computers. *Applied Radiology* 6:53-60.
121. Pacyniak, J. and Pagnamenta, A. (1974): Central axis percentage depth-dose for high energy electrons. *Radiation Research* 60:342-346.

122. Perry, D. and Holt, J. (1980): A model for calculating the effects of small inhomogeneities on electron beam dose distributions. *Med. Phys.* 7(3):207-215.
123. Peterson, M. (1983): Angular distributions in multiple scattering. *Phys. Rev. A* 28(1):135-140.
124. Pohlit, W. (1960): Dosisverteilung in inhomogenen medien bei Röntgenstrahlung mit schnellen Elektronen. *Fortschr. Röntgenstr.* 93:631-639.
125. Pohlit, W. (1965): *Dosimetrie zur Betatrontherapie* (Georg Thieme Verlag, Stuttgart).
126. Pohlit, W. (1969): Calculated and measured dose distributions in inhomogeneous materials and in patients. *Ann. N.Y. Acad. of Sci.* 161:189-197.
127. Pohlit, W. and Manegold, K. (1976): Electron-beam dose distribution in inhomogeneous media p. 244 in *High energy photons and electrons*, Suntharalingam and Zininger (eds), John Wiley and Sons (1975).
128. Puel, G. (1981): *Etude des faisceaux d'électrons - Application au calcul d'isodoses par ordinateur dans les milieux irradiés par des électrons de haute énergie*. Thesis, University of Toulouse, France.
129. Radziewsky, G. (1981): On similarity properties of scattered electron fields in homogeneous media. *Int. J. Appl. Radiat. Isot.* 32:331-343.

130. Riley, R., Mohan, R., Laughlin, J., Goodman, M., Karpowsky, A. and Gabriel, A. (1981). Use of Monte Carlo generated pencil beam data in electron dosimetry. Works in progress AAPM Meeting, Boston.
131. Roos, H., Drepper, P., and Harder, D. (1973): The transition from multiple scattering to complete diffusion of high-energy electrons p779. In Fourth symposium on microdosimetry - Euratom Eur 5122 d-e-f. (eds: Booz, J., Ebert, H., Eickely, R., Waker, A.) 1974.
132. Rossi, B. and Greisen, K. (1941): Cosmic-ray Theory. Rev. Med. Phys. 13:240-270.
133. Rossi, H. and Roesch, W. (1962): Field equations in dosimetry. Rad. Research 16:783-795.
134. Rosenfeld, M., Lanzl, L., Newton, C. and Skaggs, L. (1969). Computation of the distribution of absorbed dose and absorbed dose rate from a scanning electron beam. Strahlentherapie 138: 651-662.
135. Sandison, G. (1983): A report on the method to obtain the parameter values of the steban formula provided by the TP11 Theraplan software for the calculation of electron dose distributions. Internal report Med. Phys. Dept. Manitoba Cancer Treatment and Research Foundation, Canada.
136. Sandison, G. and Huda, W. (1987): Application of an Fermi scattering theory to the sagittaire therac 40 electron accelerator. Accepted for publication by Med. Phys. (1987).

137. Schroder-Babo, P. and Harder, D. (1981): Die charakteristischen funktionen der dosisverteilung energiereicher elektronen. p.637 in Medizinische Physik, Bunde, E. Ed (A. Huthig Verlag, Heidelberg).
138. Schroder-Babo, P. (1983): Determination of the virtual electron source of a betatron. In Computed electron beam dose planning. Acta Radiologica supplement 364:7-10.
139. Scott, W. (1963): The theory of small-angle multiple scattering of fast charged particles. Rev. Mod. Phys. 35:231-313.
140. Shabanson, L. and Hendee, W. (1979): An analytic expression for central axis electron depth dose distributions. Int. J. Rad. Oncology Biol. and Phys. 5(2): 263-267.
141. Shortt, K., Ross, C., Bielajew, A., and Rogers, D. (1986): Electron beam dose distributions near standard inhomogeneities. Phys. Med. Biol. 31:235-249.
142. Spencer, L. (1955): Theory of electron penetration. Phys. Rev. 98:1597-1615.
143. Stacey, A., Bevan, A. and Dickens, C. (1961): A new phantom material employing depolymerized natural rubber. Br. J. Radiol. 34:(404): 510-515.
144. Steben, J., Ayyangar, K. and Suntharalingham, N. (1979): Betatron electron beam characterization for dosimetry calculations. Phys. Med. Biol. 24:299-309.

145. Sterling, T., Perry, H., Katz, L. (1964): Automation of radiation treatment planning - IV. Derivation of a mathematical expression for the percent depth dose surface of ^{60}Co beams and visualization of multiple field dose distributions. Br. J. Radiol. 37:544-550.
146. Sternick, E. (1978): Algorithms for computerised treatment planning. In: Practical aspects of electron beam treatment planning (eds) Ortin, C.E. and Bagne, F. Medical Physics monograph 2:52-69.
147. Storchi, P. and Huizenga, H. (1985): On a numerical approach of the pencil beam model. Phys. Med. Biol. 30:467-473.
148. Storchi, P. and Huizenga, H. (1986): Progress on the moment method for clinical electron beam planning. Med. Phys. (Abstract).
149. Strydom, W. (1984): An analytical expression for central axis depth-dose of electrons. Phys. Med. Biol. 29:267-269.
Erratum Phys. Med. Biol. (1984) 29:605.
150. Sweeney, L., Gur, D. and Bukovitz, A. (1981): Scatter component and its effect on virtual source and electron beam quality. Int. J. Radiat. Oncol. Biol. Phys. 7:967-971.
151. Tronc, D. and Levailant, M. (1978): Absorbed dose distributions for beams from the Sagittaire. Systematic measurements and their representation for introduction into a computer. Strahlentherapie 154:643-649.

152. Ueda, T. (1979): Equations for the dose distributions of high energy electrons, *Strahlentherapie* 155:709-713.
153. Van Gasteren, J. (1984): Pencil beam parameters of clinical electron beams in proceeding of the eighth international conference on the use of computers in radiation therapy CH2048-7/84/0000/0004 IEEE:161-166.
154. Weiss, H., Epp, E. and Heslin, J. (1972): The energy spectrum electrons in water irradiated with 10 to 20 MeV electron beams. *Radiat. Res.* 51,211-228.
155. Werner, B., Khan, F. and Deibel, F. (1982): A model for calculating electron beam scattering in treatment planning. *Med. Phys.* 9:180-187.
156. Werner, B. (1984): The perturbation of electron beam dose distributions at medium interfaces. *Med. Phy.* 11:378 (Abstract).
157. Werner, B. (1985): The perturbation of electron beam dose distributions at medium interfaces. *Med. Phys.* 12:754-763.
158. White, D. (1978): Tissue substitutes in experimental radiation physics. *Med. Phys.* 5(6):467-479.
159. Zerby, C. and Keller, F. (1967): Electron transport theory, calculations and experiments. *Nucl. Sci. Eng.* 27:190-218.